APPLICATION OF SPIN SQUEEZING IN FREE SPACE ATOMIC SENSORS

A DISSERTATION
SUBMITTED TO THE DEPARTMENT OF APPLIED PHYSICS
AND THE COMMITTEE ON GRADUATE STUDIES
OF STANFORD UNIVERSITY
IN PARTIAL FULFILLMENT OF THE REQUIREMENTS
FOR THE DEGREE OF
DOCTOR OF PHILOSOPHY

Yunfan Wu
November 2021

I certify that I have read this dissertation and that, in my opinion, it is fully adequate in scope and quality as a dissertation for the degree of Doctor of Philosophy.

Mark Kasevich, Primary Adviser

I certify that I have read this dissertation and that, in my opinion, it is fully adequate in scope and quality as a dissertation for the degree of Doctor of Philosophy.

Leo Hollberg

I certify that I have read this dissertation and that, in my opinion, it is fully adequate in scope and quality as a dissertation for the degree of Doctor of Philosophy.

Amir Safavi-Naeini

Approved for the Stanford University Committee on Graduate Studies.

Stacey F. Bent, Vice Provost for Graduate Education

Abstract

Atomic sensors measure a variety of physical quantities with ensembles of atoms. With careful engineering, the resolution of the atomic sensors can reach the quantum-projection limit. To beat this limit and further improve the resolution, spin squeezing, a specific entangled state, can be utilized.

In this thesis, I focus on the application of spin squeezing to free space atomic sensors; specifically, atomic fountain clocks and atom interferometers. In our experiment, spin squeezing is generated by a quantum non-demolition measurement on J_z using an optical cavity, which gives maximum metrological squeezing so far. In this method, atoms are trapped by an optical lattice. Therefore, for free space applications, which require atoms to move freely in space, the atoms need to be released after squeezing generation. Two methods are introduced to retrieve squeezing after free space release.

The first method is based on the optical cavity, the same as the one used to generate squeezing. Using this method, almost all the metrological squeezing is retrieved at short release time ($\sim$ 13dB). $\sim$ 10dB squeezing maintains for up to hundreds of microseconds. Squeezing degrades to almost 0dB within 3ms. The study of this degradation leads to the understanding of the effects of coupling homogeneity loss.

The second method uses a CMOS camera. This camera measures the J_z value by fluorescence imaging while atoms are moving freely in space. 5.8dB metrological squeezing is retrieved by this method while maintaining constant with release time for up to 4ms. Then a free space Ramsey spectroscopy below quantum-projection limit is successfully demonstrated using the camera method, which is an important step to build an atomic fountain clock. The clock enhancement is 5.8dB for interrogation time less than 1.3ms. This is limited by the camera resolution. At 3.6ms interrogation time, the clock enhancement is 3.8dB, corresponding to 2.4 times reduction in averaging time. The enhancement reduces at longer interrogation time because of microwave phase and amplitude noise, as well as magnetic field fluctuations.

Finally, I will detail the laser system I construct to do atom interferometry based on Raman transitions. The interferometer performance is tested by interferometer contrast and final J_z noise at the output port. Different types of noise sources to the final J_z are also studied.

Acknowledgments

First, I would like to thank my advisor Mark Kasevich for giving me the opportunity to study and work in your group for the past 6 years. Your optimism, enthusiasm, and attitudes towards research have deeply inspired me. You are very optimistic and have the ability to see opportunities from seemingly difficult situations. I remember at one time while we were struggling with some experimental problems that stopped us from moving forward, you immediately came up with a new research topic that helped me to think about additional research opportunities. Not only that, I would never forget your warnings of falling into the trap of publishing works that do not add something new to the field. You really commit to advancing the state of the art of the field in a significant way. In addition, your knowledge and insights on physics have guided me through many confusing and uncertain moments. I really appreciate your time spent on giving experimental advice and providing suggestions on my publications.

Next, I would like to thank my defense committee: Mark Kasevich, Leo Hollberg, Tony Heinz, Amir Safavi-Naeini, and Tsachy Weissman for your time and availability. I am also grateful to my reading committee: Mark, Leo, and Amir.

I was fortunate to work with a wonderful team during my time here at Stanford. Thank you Onur Hosten for mentoring me with great patience and wisdom during my first two years in the group. I always found great joy and learned a lot by discussing problems with you and seeing how you tackled them. Thank you Rajiv Krishnakumar. You taught me a lot about how to run the experiment. I still remember days when we stayed up late taking data in the lab and days when we used a manual drill to replace the MOT laser. I also owe you the introduction to the music from Gorillaz. Thank you Nils Englesen for your kindness and knowledge. You helped me a lot to transition smoothly into the group and answered so many of my weird questions. I found great inspiration when I saw your best wishes written on the Atomic Physics books you gave me. I really appreciated our discussions through Whatsapp and your remote mentoring. Thank you Julian Martinez. Your theoretical knowledge and practical optics skills were irreplaceable for the team. There were times when you came to the lab and solved all the confusion about the optics that Ben and I had. You also have a good taste of humor that added little breaks to some of our long and intense discussions. Thank you Benjamin Malia for being my fellow graduate student. We worked most of the time together in the lab. Your perseverance and openness to try new things inspired me a lot. It was really a pleasure to collaborate with you. In addition, thank you for your help on my thesis writing.

I am indebted to my predecessors on the spin squeezing experiment who built the apparatus and made tremendous improvements: Geert Vrijsen, Jongmin Lee, Igor Teper, Onur Hosten, Nils Engelsen, and Rajiv Krishnakumar.

I would like to thank the rest of the Kasevich group members, both past and present: Brannon Kloper, Yonantan Israel, Stewart Koppell, Adam Bowman, Thomas Juffmann, Fan Xiao, David Berryrieser, Peter Asenbaum, Chris Overstreet, Tim Kovachy, Remy Notermans, Minjeong Kim, Joseph Curti, Shaun Burd, and Gugliemo Panelli. I really enjoyed the discussions about interesting physics and non-physics questions during lunch time and Friday happy hours. I also appreciate the group activities such as group bike ride, group ski trip, and birthday celebrations. Special thanks to Brannon, you were the guy I always turned to when having computer problems and you were always willing to help.

I would like to thank the Varian second floor AMO society including Schleier-Smith group and Hogan group. Thank you for creating an atmosphere for discussions and mutual supports.

Thank you to the group administrators Ping Feng, Fang Tian, and Sha Zhang. Your help with all the paperwork and administration requirements made my PhD life so much easier. I would also like to thank Scott Barton for the help with package deliveries and Mehmet Solyali for teaching me how to use the machines in the machine shop. Thank you to the applied physics administrators Paula Perron, Patrice O'Dwyer, Fiona Chiu, and Claire Nicholas. You have helped me stay on track with every PhD milestone.

I would like to thank all my friends, both near and far. You made my PhD life so much colorful, enjoyable, and warm. We have spent a lot of good times hiking, backpacking, and cycling. We have also spent many good times playing fun games, trying delicious food, and chatting.

Last but not least, I would like to thank my parents. Thank you for your unconditinal love and support. Those thanks are more than words could express.

Contents

List of Tables

List of Figures

Chapter 1

Introduction

Physics has experienced many exciting discoveries in the second decade of the 21st century, such as the discovery of Higgs Boson in 2012, the last unverified part of the standard model; the first observation of gravitational waves in 2015, the last remaining directly undetected prediction of general relativity; and the capture of the first image of a black hole in 2019. The theories of the standard model and general relativity are mysteriously contradictory. Physicists are urged to research this mystery, in part by searching for new physics beyond the standard model such as dark matter, dark energy, matter-antimatter asymmetry, and charge, parity, time symmetry violations, and in part by conducting more precise tests on the theory of relativity. Other than exploring the universe with larger telescopes and colliders, physicists are also exploring with atoms and molecules [1, 2]. Atomic clocks set the world record for frequency standard, which reached and surpassed the 10^{-18} level so researchers can detect gravitational redshifts on atoms separated by a few centimeters [3, 4, 5, 6]. While atomic clocks utilize the atoms' internal states, atom interferometers study the momentum states of atoms, enabling the test of motion. Atom interferometric tests on the Equivalence Principle have been implemented at the 10^{-12} level [7]. Proposals using atom interferometers as dark matter and gravitational wave sensors are being investigated [8, 9, 10]. Both atomic clocks and atom interferometers are widely used atomic sensors. They potentially advance the field of fundamental physics and our daily lives. For example, atomic clocks are used in Global Positioning Systems (GPS); they also set the definition of a second. Atom interferometers serve as gyroscopes, gravimeters, and accelerometers [11, 12, 13, 14, 15]. However, most of these sensors use uncorrelated atoms, limiting their ultimate sensitivity to quantum projection noise (QPN), which is the limit after all the technique noise is identified and eliminated. With careful engineering, this limit has been achieved in many systems [16, 17, 18, 19, 20, 21]. The QPN scales with $1/\sqrt{N}$ where N is the number of atoms used in a sensor. One way to improve the sensitivity is by increasing N. However, the maximum number of atoms is limited by the volume and density of an atomic ensemble. Another way to improve the sensitivity is by using correlated atoms so QPN can be surpassed where the ultimate limit scales with $1/N$. We call this $1/N$ scaling the Heisenberg limit.

Quantum metrology explores quantum correlations among atoms to overcome QPN of measurements with the ultimate goal of reaching the Heisenberg limit [22]. Even though this limit is far reaching, recent experiments demonstrate the potential of spin squeezed states in metrologies where the limit scales with $1/\sqrt{N^{3/2}}$ [23, 24]. Spin squeezed states are experimentally generated using multiple methods such as collisional interaction [25, 26], QND measurement [27, 28, 29], and cavity feedback [30]. To date, the best metrological relevant squeezing is generated with cold atoms trapped in an optical lattice whose collective state is probed by an optical cavity mode [24, 31]. This method results in a squeezing level of 20dB, which is a hundred times reduction in the variance of the phase measurements. An atomic clock with sensitivity below QPN has also been demonstrated [27, 32, 24, 33]. However, in these clock demonstrations, atoms are spatially confined. No experiment has applied spin squeezed states to sensors that require atoms to move freely in space like atomic fountain clocks and atom interferometers. This thesis describes efforts towards building spin squeezed free space atomic sensors.

We generate spin squeezing with trapped atoms by the cavity method. The first step to apply these trapped spin squeezed atoms to free space atomic sensors is to release the atoms to free space and demonstrate the ability to retrieve squeezing from free space. In this thesis, after introducing the basic concepts in Ch2 and apparatus and sequence in Ch3, I will describe two methods to successfully retrieve free space spin squeezing. The first uses an optical cavity. I will introduce this method in Ch4 along with a study on atom-cavity coupling homogeneity loss that degrades retrieved squeezing. The second method is based on a camera and is described in Ch5. Ch5 also demonstrates a spin squeezed fountain clock sequence. After the success in integrating spin squeezing to a fountain clock sequence, we move on to build a spin squeezed atom interferometer. In Ch6, I will report our progress and efforts on this project.

Chapter 2

Basic concepts

This chapter presents basic concepts and theories that are relevant to the thesis work. I first cover the basic ideas for quantum state in general and spin squeezed state in particular. Next, I detail the light matter interactions for 2-level and 3-level systems that are relevant for quantum state manipulations in the experiment. Then I describe how spin squeezed state is generated using light matter interactions. Finally, I outline the concepts for atomic clocks and atom interferometers.

2.1 2-level system

2.1.1 Angular momentum operators

A 2-level system has two non-degenerate eigenstates $|a\rangle$ and $|b\rangle$ with eigenvalues E_a and E_b respectively. Since it has only two eigenstates, a 2-level system forms a pseudo-spin 1/2 system where $|a\rangle$ stands for spin up $|\uparrow\rangle$ and $|b\rangle$ stands for spin down $|\downarrow\rangle$. We define angular momentum operator $\vec{j} = (j_x, j_y, j_z)$ for this pseudo-spin 1/2 system where

$$\begin{aligned} j_x &= \frac{|\uparrow\rangle\langle\downarrow| + |\downarrow\rangle\langle\uparrow|}{2} = \frac{1}{2}\sigma_x \\ j_y &= -i\frac{|\uparrow\rangle\langle\downarrow| - |\downarrow\rangle\langle\uparrow|}{2} = \frac{1}{2}\sigma_y \\ j_z &= \frac{|\uparrow\rangle\langle\uparrow| - |\downarrow\rangle\langle\downarrow|}{2} = \frac{1}{2}\sigma_z. \end{aligned} \tag{2.1}$$

Here, σ_x, σ_y, σ_z are the traceless Pauli matrices. We have $\vec{j} = \vec{\sigma}/2$ where $\vec{\sigma} = (\sigma_x, \sigma_y, \sigma_z)$.

2.1.2 Quantum state

The quantum state of a system is represented by density operator $\rho = \sum_i p_i|\psi_i\rangle\langle\psi_i|$. This operator has two properties: 1. $Tr(\rho) = 1$ (the same as $\sum_i p_i = 1$); 2. $Tr(\rho^2) \leq 1$. When $Tr(\rho^2) < 1$, the system is in a mixed state; when $Tr(\rho^2) = 1$, the system is in a pure state.

For a 2-level system, the density operator ρ takes the form of a 2-by-2 matrix and is written as $\rho = (I + \vec{a} \cdot \vec{\sigma})/2$ where $\vec{a} = (u, v, w) \in \mathcal{R}^3$ is the Bloch vector and $\vec{a} = \langle \vec{\sigma} \rangle$. This equation establishes the one-to-one correspondence between the density operator ρ and $\vec{a}$. Based on the properties of the density operator, $|\vec{a}| \leq 1$. Thus, The system quantum state is geometrically represented by a unit sphere and is called the Bloch sphere. When $|\vec{a}| < 1$, the system is in a mixed state and the system state is represented by the inner space of the Bloch sphere; when $|\vec{a}| = 1$, the system is in a pure state and the system state is represented by the surface of the Bloch sphere. From the relation between $\vec{a}, \vec{\sigma}$, and $\vec{j}$, we find $\langle \vec{j} \rangle = \vec{a}/2$.

For a pure state, the density operator writes $\rho = |\psi\rangle\langle\psi|$. Thus, the state can be simply represented by $|\psi\rangle$. Using the Bloch sphere representation, the state is represented by its surface. Therefore, we only need two variables to describe the state. This can be seen by writing $|\psi\rangle = \cos(\theta/2)|\uparrow\rangle + \sin(\theta/2)e^{i\phi}|\downarrow\rangle$ up to a common phase term, where $0 \leq \theta \leq \pi$ and $0 \leq \phi < 2\pi$. We find $\vec{a} = (\sin\theta\cos\phi, \sin\theta\sin\phi, \cos\theta)$ by writing out each term in ρ with θ, ϕ and with u, v, w separately. Here, θ and ϕ are understood as the polar and azimuth angle of the Bloch sphere. ϕ is the phase between the $|\uparrow\rangle$ and $|\downarrow\rangle$ states.

2.1.3 Sensing

When a 2-level system senses the environment, the environmental perturbations cause differential energy shift between the two atomic states. This energy shift rotates $\vec{a}$ around the z axis, thus, the phase between the two states changes from ϕ to ϕ'. By measuring $\phi' - \phi$ we measure the environmental perturbations.

2.2 N 2-level systems

2.2.1 Collective angular momentum operators

For N 2-level systems we can define collective angular momentum operators $\vec{J} = (J_x, J_y, J_z)$. Here $J_m = \sum_{i=1}^{N} j_{m,i}$ where $j_{m,i}$ is the angular momentum of an individual system and $m \in \{x, y, z\}$. Theses collective operators satisfy commutation relations

$$[J_x, J_y] = iJ_z, \quad [J_z, J_x] = iJ_y, \quad [J_y, J_z] = iJ_x. \tag{2.2}$$

These commutation relations result in an uncertainty relation

$$\Delta J_y \Delta J_z \geq |\langle J_x \rangle/2|. \tag{2.3}$$

2.2.2 Coherent spin state and quantum projection limit

The 2^N eigenstates for the composite system containing N 2-level systems are formed by the direct product of eigenstates of individual systems. However, if the N 2-level systems are identically prepared, the number of eigenstates to form a complete basis reduces to $N+1$, because the system lives in the symmetric subspace. In this subspace, the total spin $J = N/2$. A well-known set of basis are the eigenstates of J_z, i.e. $J_z|J, M\rangle = M|J, M\rangle$ where $M \in \{-N/2, -N/2+1, \ldots, N/2-1, N/2\}$.

In the symmetric subspace, when no quantum correlations exist among individual systems and the composite system remains pure, the quantum state of this composite system is $|\Psi\rangle = |\psi\rangle_1 \otimes \cdots \otimes |\psi\rangle_N$ where $|\psi\rangle_i = \cos(\theta/2)|\uparrow\rangle_i + \sin(\theta/2)e^{i\phi}|\downarrow\rangle_i$. Because the states of individual systems are identical, we only need two real numbers θ and ϕ to describe $|\Psi\rangle$. For pictorial representation, the expectation values of the collective angular momentum form a vector (Bloch vector) with length $N/2$ and pointing with azimuth angle ϕ and polar angle θ similar to the Bloch sphere representation in the 2-level case. The z coordinate of this vector J_z represents half the population difference between $|\uparrow\rangle$ and at $|\downarrow\rangle$ states. The orientation of the vector projection in the xy plane as represented by ϕ stands for the phase difference between $|\uparrow\rangle$ and $|\downarrow\rangle$ states. When $\theta = \pi/2$ and $\phi = 0$, $\langle J_x\rangle = |J| = N/2$, $\langle J_y\rangle = 0$, and $\langle J_z\rangle = 0$. In this case, $\Delta J_y = \Delta J_z = \sqrt{N}/2$. This is called the quantum projection limit (QPL) and the state is called a coherent spin state (CSS). The state is pictorially shown in Figure 2.1 by its Wigner function. Even if the CSS state is defined with $\theta = \pi/2$ and $\phi = 0$, the state is still a CSS if the state vector is rotated to other azimuth and polar angles, because the minimum quantum uncertainty is satisfied and is equally distributed between two orthogonal quadratures [34].

2.2.3 Phase estimation

For phase estimation we consider the case where the quantum state is most sensitive to the environment, i.e. $\theta = \pi/2$. Similar to the 2-level case, environmental perturbations rotates the Bloch vector around the z axis, causing a phase change ϕ on the xy plane. This phase change can be experimentally measured by measuring the population difference after rotating the Bloch vector around its initial position by 90°, because after the rotation $\theta = \pi/2 \pm \phi$. Here ϕ is usually very small and the sign depends on the direction of the rotation. Thus, $J_z = N/2 \cdot \cos(\pi/2 \pm \phi) \approx \pm N\phi/2$, $\phi \approx \pm J_z/(N/2)$. For a coherent spin state, the phase resolution $\Delta\phi$ satisfies equation $(\Delta\phi)^2 \approx 4(\Delta J_z)^2/N^2 = 1/N$, $\Delta\phi = 1/\sqrt{N}$. This is the quantum projection limit for phase estimation. To increase the resolution (sensitivity) of ϕ, larger N should be used. However, the ability to increase N is limited. A spin squeezed state can reduce $\Delta\phi$ without increasing N.

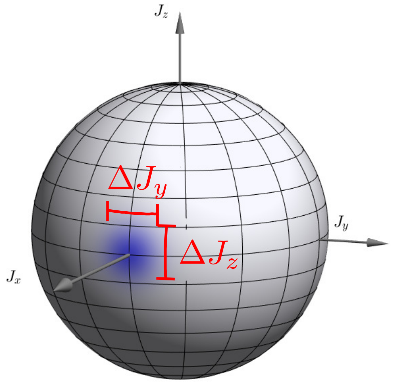

Figure 2.1: Wigner function of a coherent spin state. The uncertainty in the J_z and J_y directions are equal to $\sqrt{N}/2$. The state remains coherent state after rotations to other azimuth and polar angles

2.2.4 Spin squeezed state

Spin squeezed state is a type of entangled state that can beat QPL [34]. Compared to CSS, where the quantum uncertainty is equally distributed between two quadratures ($\Delta J_y = \Delta J_z = \sqrt{N}/2$), the uncertainty is not equally distributed for the spin squeezed state due to quantum correlations. A reduction of uncertainty in J_z causes an increase in uncertainty in J_y since the uncertainty relation Equation 2.3 must be satisfied. The state is shown in Figure 2.2 by its Wigner function. We call $\Delta J_z < \sqrt{N}/2$ squeezing and $\Delta J_y > \sqrt{N}/2$ anti-squeezing.

2.2.5 Metrological squeezing

When atoms are used for sensing, i.e. metrology, the Bloch vector rotates around the z axis as shown by the red arrows in Figure 2.3. It is important that the length of the arm L remains large where $L = C \cdot N/2$ and C is the coherence of the N 2-level systems. When $C = 1$, the systems are fully coherent. When $0 < C < 1$, the systems are partially decohered. When $C = 0$, the systems are fully decohered. We can see that when $C = 0$, there is no rotation any more. The larger the C, the easier it is to distinguish small rotations.

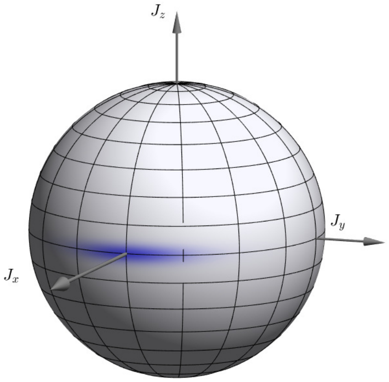

Figure 2.2: Wigner function of a spin squeezed state. The uncertainty in J_z is decreased below QPL (squeezing), while the uncertainty in J_y is increased above QPL (anti-squeezing).

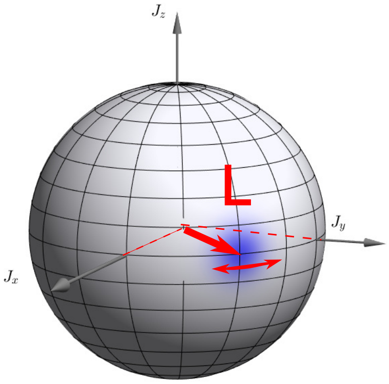

Figure 2.3: Picture for metrological purposes. When atoms are used for sensing, it is important that the arm length L remains large. This length corresponds to the coherence of the atoms.

Wineland criterion characterizes the metrological squeezing:

$$\xi^2 = (\frac{\Delta J_z}{\sqrt{N}/2} \cdot \frac{1}{C})^2 \tag{2.4}$$

[35, 36]. This criterion compares the J_z noise to the coherent state noise and takes into account the system coherence. We say metrological gain exists when $\xi^2 < 1$. In this case, the resolution is improved by spin squeezing. Not only is ΔJ_z smaller than coherent state noise, it is also small enough to compensate for decoherence. When $\xi^2 > 1$, there is no metrological gain. By convention, the Wineland criterion is represented in decibels (dB), which is $10 \log \xi^2$.

2.3 Atomic system

We use an ensemble of cold thermal ^{87}Rb atoms as the N 2-level systems in our experiment. Each atom forms a 2-level system. The two levels or two atomic states are the two magnetically insensitive hyperfine ground states as shown by Figure 2.4. They are denoted by $|\uparrow\rangle$ and $|\downarrow\rangle$, i.e. $|\uparrow\rangle = |F = 2, m_F = 0\rangle$ and $|\downarrow\rangle = |F = 1, m_F = 0\rangle$. Using the magnetically insensitive states means that the states are immune to first order Zeeman shifts and thus more robust against stray magnetic fields.

In our experiment, we use three different types of atom-light interactions to manipulate the quantum state of the atoms. The first is a direct interaction between a microwave signal and $|\uparrow\rangle$ to $|\downarrow\rangle$ transition. This interaction is described by a semi-classical picture of a 2-level system interacting with a single mode electromagnetic field. The second is a dispersive interaction between an optical mode and the D_2 line (the $5^2S_{1/2} \rightarrow 5^2P_{3/2}$ transition) to prepare spin squeezing. This interaction requires a quantum picture to describe. The third is a Raman transition that also utilizes the D_2 line. The Raman transition is used for atom interferometries. In the next two sections, I will describe the three types of interactions.

2.4 2-level system interact with electromagnetic fields

2.4.1 Semi-classical picture

To understand how we use a microwave to manipulate the quantum state of the 2-level system in our experiment, we need the semi-classical picture to describe the interaction between the microwave and the 2-level system.

We consider an electromagnetic field interacting with a 2-level system whose Hamiltonian is $H = E_a|a\rangle\langle a| + E_b|b\rangle\langle b|$. In electric dipole approximation, the interaction Hamiltonian is $V = \vec{p} \cdot \vec{E}$

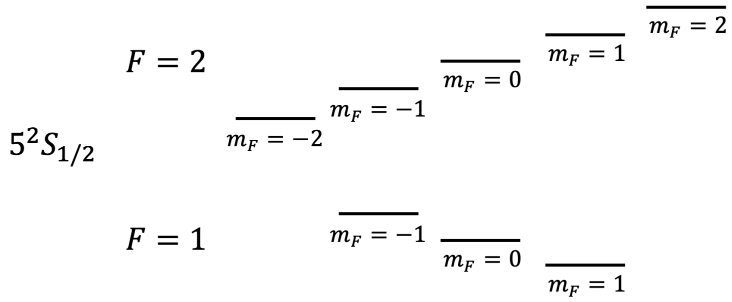

Figure 2.4: Magnetic sublevels of ^{87}Rb ground state hyperfine splittings. The degeneracy of the sublevels is lifted by a constant magnetic field. The relative energy differences are plotted against each other. The two $m_F = 0$ sublevels are the two magnetically insensitive states

where $\vec{p}$ is the dipole moment and $\vec{E}$ is the electric field. The system state can be written as $|\psi(t)\rangle = \psi_a(t)e^{-i\omega_a t}|a\rangle + \psi_b(t)e^{-i\omega_b t}|b\rangle$ where $E_a = \hbar\omega_a$ and $E_b = \hbar\omega_b$. This leads to a Schrodinger equation as below:

$$i\hbar \begin{pmatrix} \dot{\psi}_a \\ \dot{\psi}_b \end{pmatrix} = \begin{pmatrix} V_{aa} & V_{ab}e^{i\omega_{ab}t} \\ V_{ba}e^{i\omega_{ba}t} & V_{bb} \end{pmatrix} \begin{pmatrix} \psi_a \\ \psi_b \end{pmatrix} \tag{2.5}$$

where $V_{aa} = V_{bb} = 0$, because $\vec{p}$ is a parity odd vector (operator). $V_{ab} = \langle a|V|b\rangle$ and $V_{ba} = \langle b|V|a\rangle$.

If the electric field contains a single mode, i.e. $\vec{E} = E_0\vec{\epsilon}\cos(\omega t + \phi)$ where $\vec{\epsilon}$ is the polarization unit vector for the electric field. $V_{ab} = \langle a|\vec{p}\cdot\vec{\epsilon}|b\rangle E_0 \cos(\omega t + \phi)$ and $V_{ba} = \langle b|\vec{p}\cdot\vec{\epsilon}|a\rangle E_0 \cos(\omega t + \phi)$.

We substitute the equations for V_{ab} and V_{ba} in Equation 2.5 and get

$$i \begin{pmatrix} \dot{\psi}_a \\ \dot{\psi}_b \end{pmatrix} = \begin{pmatrix} 0 & \Omega\frac{e^{i(\omega t+\phi)}+e^{-i(\omega t+\phi)}}{2}e^{-i\omega_0 t} \\ \Omega^*\frac{e^{i(\omega t+\phi)}+e^{-i(\omega t+\phi)}}{2}e^{i\omega_0 t} & 0 \end{pmatrix} \begin{pmatrix} \psi_a \\ \psi_b \end{pmatrix} \tag{2.6}$$

where $\Omega = \langle a|\vec{p}\cdot\vec{\epsilon}|b\rangle E_0/\hbar$ is the Rabi frequency. Under rotating-wave approximation (RWA), the terms that vary at $e^{\pm i(\omega+\omega_0)t}$ are ignored, the equation becomes

$$i \begin{pmatrix} \dot{\psi}_a \\ \dot{\psi}_b \end{pmatrix} = \begin{pmatrix} 0 & \frac{\Omega}{2}e^{i(\delta t+\phi)} \\ \frac{\Omega^*}{2}e^{-i(\delta t+\phi)} & 0 \end{pmatrix} \begin{pmatrix} \psi_a \\ \psi_b \end{pmatrix} \tag{2.7}$$

where $\delta = \omega - \omega_0$ is the detuning. The solution to this equation is

$$\begin{pmatrix} \psi_a(t) \\ \psi_b(t) \end{pmatrix} = \begin{pmatrix} (\cos\frac{Wt}{2} - \frac{i\delta}{W}\sin\frac{Wt}{2})e^{\frac{1}{2}i\delta t} & -i\frac{\Omega}{W}\sin\frac{Wt}{2}e^{\frac{1}{2}i\delta t}e^{i\phi} \\ -i\frac{\Omega^*}{W}\sin\frac{Wt}{2}e^{-\frac{1}{2}i\delta t}e^{-i\phi} & (\cos\frac{Wt}{2} + \frac{i\delta}{W}\sin\frac{Wt}{2})e^{-\frac{1}{2}i\delta t} \end{pmatrix} \begin{pmatrix} \psi_a(0) \\ \psi_b(0) \end{pmatrix} \tag{2.8}$$

where $W = \sqrt{\delta^2 + |\Omega|^2}$.

Rotating-wave approximation is valid when $\delta \ll \omega_0$. Even so, the ignored fast rotating term can cause a very small shift on the true resonance frequency [37]. In addition, accurate solutions exist without RWA when considering circularly polarized light [38].

To understand the solution intuitively, we first discuss the solution of a first order differential equation as shown below:

$$\begin{pmatrix} \dot{\psi}_a \\ \dot{\psi}_b \end{pmatrix} = i \begin{pmatrix} A(t) & B(t) \\ B^*(t) & D(t) \end{pmatrix} \begin{pmatrix} \psi_a \\ \psi_b \end{pmatrix} \tag{2.9}$$

where $A(t), D(t) \in \mathcal{R}$. We do the following transformation for ψ_a and ψ_b:

$$\begin{aligned} |\psi_a|^2 &= \frac{1+w}{2} \\ |\psi_b|^2 &= \frac{1-w}{2} \\ \psi_a \psi_b^* &= \frac{u-iv}{2}. \end{aligned} \tag{2.10}$$

The new equations then become:

$$\begin{aligned} \dot{u} &= [A(t) - D(t)] \cdot v + 2\Im[B(t)] \cdot w \\ \dot{v} &= [D(t) - A(t)] \cdot u + 2\Re[B(t)] \cdot w \\ \dot{w} &= -2\Im[B(t)] \cdot u - 2\Re[B(t)] \cdot v. \end{aligned} \tag{2.11}$$

Thus

$$\frac{d\vec{a}}{dt} = \vec{\Omega}(t) \times \vec{a} \tag{2.12}$$

where $\vec{\Omega}(t) = (-2\Re[B(t)], 2\Im[B(t)], D(t) - A(t))$ and $\vec{a} = (u, v, w)$. The solution of a 2-level system can be understood as a rotation of a vector $\vec{a}$ around another vector $\vec{\Omega}(t)$. If A, B, D are time-independent, we call $2|B|$ and $D - A$ the Rabi frequency and the detuning of the interaction respectively.

We can get rid of the time dependency in the Hamiltonian of Equation 2.7 by applying a transformation

$$\begin{pmatrix} \psi_a \\ \psi_b \end{pmatrix} = \begin{pmatrix} e^{i\eta t} & 0 \\ 0 & e^{-i\eta t} \end{pmatrix} \begin{pmatrix} \tilde{\psi_a} \\ \tilde{\psi_b} \end{pmatrix} \tag{2.13}$$

to it. We find when $\eta = \delta/2$, the new equation becomes

$$\frac{d}{dt} \begin{pmatrix} \tilde{\psi_a} \\ \tilde{\psi_b} \end{pmatrix} = -i \begin{pmatrix} \frac{\delta}{2} & \frac{\Omega}{2} e^{i\phi} \\ \frac{\Omega^*}{2} e^{-i\phi} & -\frac{\delta}{2} \end{pmatrix} \begin{pmatrix} \tilde{\psi_a} \\ \tilde{\psi_b} \end{pmatrix}, \tag{2.14}$$

where the time-dependent terms are cancelled. According to Equation 2.9 to Equation 2.12, Equation 2.14 can be understood as a rotation of vector $\vec{a}$ around $\vec{\Omega} = (\Re[\Omega e^{i\phi}], -\Im[\Omega e^{i\phi}], \delta)$. The Rabi frequency is $2|\Omega|$ and the detuning of the interaction is δ.

In our experiment, the transition between $|\uparrow\rangle$ and $|\downarrow\rangle$ induced by the microwave is not because of the coupling to the electric field but the coupling to the magnetic field. Thus, the expression for Ω is proportional to the magnetic field and the magnetic dipole moment. However, the conclusion remains the same that the microwave field rotates the state vector $\vec{a}$ around $\vec{\Omega}$.

2.4.2 Quantum picture and dispersive interaction

To understand the interaction between the optical mode and the D_2 line for the generation of spin squeezing, we can use the quantum picture to describe this interaction.

In the quantum picture, the electromagnetic fields are quantized and the system under consideration includes both the two-level system and the quantized electromagnetic field. The total Hamiltonian then writes [38]

$$H = H_F + H_A + H_I.$$

The first term

$$H_F = \sum_{\vec{k}} \hbar(\omega_k a^\dagger_{\vec{k}} a_{\vec{k}} + 1/2)$$

is the total energy of the field. The second term

$$H_A = E_a|a\rangle\langle a| + E_b|b\rangle\langle b|$$

is the total energy of the 2-level system. The third term describes the interaction and writes

$$H_I = \hbar\sum_{\vec{k}}(g^{ab}_{\vec{k}}\sigma_{ab} + g^{ba}_{\vec{k}}\sigma_{ba})(a_{\vec{k}} + a^\dagger_{\vec{k}})$$

in the dipole approximation where $g^{ab}_{\vec{k}} = -e\langle a|\vec{r}|b\rangle\cdot\vec{\epsilon}_{\vec{k}}\mathcal{E}_{\vec{k}}/\hbar$, $g^{ba}_{\vec{k}} = -e\langle b|\vec{r}|a\rangle\cdot\vec{\epsilon}_{\vec{k}}\mathcal{E}_{\vec{k}}/\hbar$, and $\mathcal{E}_{\vec{k}} = \sqrt{\frac{\hbar\omega_k}{2\epsilon_0 V}}$. For simplicity, we assume $g_{\vec{k}} = g^{ab}_{\vec{k}} = g^{ba}_{\vec{k}}$ and up to a constant the total Hamiltonian becomes

$$H = \sum_{\vec{k}} \hbar\omega_k a^\dagger_{\vec{k}} a_{\vec{k}} + \frac{1}{2}\hbar\omega_0\sigma_z + \hbar\sum_{\vec{k}} g_{\vec{k}}(\sigma_+ + \sigma_-)(a_{\vec{k}} + a^\dagger_{\vec{k}}) \tag{2.15}$$

where $\omega_0 = (E_a - E_b)/\hbar$, $\sigma_z = |a\rangle\langle a| - |b\rangle\langle b|$, $\sigma_+ = \sigma_{ab} = |a\rangle\langle b|$, and $\sigma_- = \sigma_{ba} = |b\rangle\langle a|$. The interaction Hamiltonian includes 4 terms. The term $\sigma_+ a_{\vec{k}}$ describes the process where the 2-level system is taken from the ground state to the excited state by absorbing a photon. The term $\sigma_- a^\dagger_{\vec{k}}$

describes the opposite process. These two terms preserve the energy. The term $\sigma_+ a^\dagger_{\vec{k}}$ describes the process where the 2-level system is taken from the ground state to the excited state and emits a photon. In this process, the system gains approximate $2\hbar\omega_0$ energy. The term $\sigma_- a_{\vec{k}}$ leads to a loss of approximate $2\hbar\omega_0$ energy. Under RWA, the energy non-conserving terms are ignored, the system Hamiltonian becomes

$$H = \sum_{\vec{k}} \hbar\omega_k a^\dagger_{\vec{k}} a_{\vec{k}} + \frac{1}{2}\hbar\omega_0\sigma_z + \hbar\sum_{\vec{k}} g_{\vec{k}}(\sigma_+ a_{\vec{k}} + \sigma_- a^\dagger_{\vec{k}}). \tag{2.16}$$

Next we consider a single mode field and derive the effective system Hamiltonian in the dispersive regime following the steps in Ch3 of [39]. In the dispersive regime, the field frequency is far off resonant from the 2-level transition compared to the coupling term, i.e. $|\Delta| = |\omega - \omega_0| \gg g$. In this regime, we can apply a unitary transformation $U = e^\eta$ to remove the off-diagonal term from H that is first order in g. After the transformation, we have

$$\tilde{H} = UHU^\dagger = H + [\eta, H] + \frac{1}{2}[\eta, [\eta, H]] + ... \tag{2.17}$$

For a single mode field, using perturbation theory we write the system Hamiltonian $H = H_0 + V$ where

$$H_0 = \hbar\omega a^\dagger a + \frac{1}{2}\hbar\omega_0\sigma_z$$

and

$$V = \hbar g(\sigma_+ a + \sigma_- a^\dagger).$$

V is the off-diagonal term linear in g. Thus, Equation 2.17 becomes

$$\tilde{H} = H_0 + V + [\eta, H_0] + [\eta, V] + \frac{1}{2}[\eta, [\eta, H_0]] + \frac{1}{2}[\eta, [\eta, V]] + ... \tag{2.18}$$

To get rid of the off-diagonal term in the system Hamiltonian that is first order in g, we expect η to be of order g such that it is possible to have

$$V + [\eta, H_0] = 0. \tag{2.19}$$

In this case, $\tilde{H} \approx H_0 + \frac{1}{2}[\eta, V]$ ignoring terms higher than second order of g. We find

$$\eta = \frac{g}{\Delta}(a\sigma_+ - a^\dagger\sigma_-) \tag{2.20}$$

satisfies Equation 2.19. Thus, we arrive at the dispersive Hamiltonian

$$\tilde{H} = H_0 + \hbar\frac{g^2}{\Delta}(a^\dagger a + \frac{1}{2})\sigma_z. \tag{2.21}$$

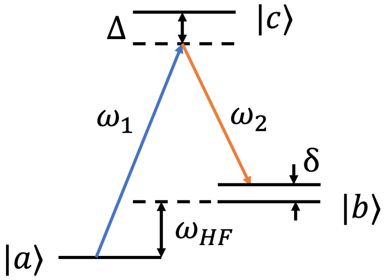

Figure 2.5: Λ system for Raman transitions. The system includes 3 energy levels that form a structure of Λ. Two laser beams with frequency ω_1 and ω_2 are used to drive the Raman transition. The single photon detuning is Δ and the two photon detuning is δ. ω_{HF} is the frequency difference between the two lowest energy levels.

This method of deriving effective Hamiltonian by applying a unitary transformation to the total Hamiltonian and keeping terms only up to some fixed order is common [40].

In our experiment, the optical mode is far off-resonant from the D_2 line. The interaction Hamiltonian hence takes the dispersive form. The squeezing is generated based on this dispersive interaction as will be shown later.

2.5 3-level system interact with electromagnetic fields

We use Raman transitions to manipulate the quantum state of the system for atom interferometries. The Raman transition requires at least 3 levels that form a Λ structure as shown by Figure 2.5. For our experiment, the Raman transition utilizes the D_2 line as well. The 3 levels are the two magnetically insensitive hyperfine ground states and the excited state $5^2P_{3/2}$. We start our discussions from the interaction between a 3-level system and electromagnetic fields in a general setting.

The Hamiltonian of a 3-level system can be written as $H = E_a|a\rangle\langle a| + E_b|b\rangle\langle b| + E_c|c\rangle\langle c|$. When interacting with electromagnetic fields, the interaction Hamiltonian is $V = \vec{p}\cdot\vec{E}$ under electric dipole approximation. The system state is $|\psi(t)\rangle = \psi_a(t)e^{-i\omega_a t}|a\rangle + \psi_b(t)e^{-i\omega_b t}|b\rangle + \psi_c(t)e^{-i\omega_c t}|c\rangle$ where $E_i = \hbar\omega_i$ and $i \in \{a, b, c\}$. Then, $\psi_a(t)$, $\psi_b(t)$, and $\psi_c(t)$ satisfy the Schrodinger equation:

$$i\hbar \begin{pmatrix} \dot{\psi}_a \\ \dot{\psi}_b \\ \dot{\psi}_c \end{pmatrix} = \begin{pmatrix} 0 & V_{ab}e^{i\omega_{ab}t} & V_{ac}e^{i\omega_{ac}t} \\ V_{ba}e^{i\omega_{ba}t} & 0 & V_{bc}e^{i\omega_{bc}t} \\ V_{ca}e^{i\omega_{ca}t} & V_{cb}e^{i\omega_{cb}t} & 0 \end{pmatrix} \begin{pmatrix} \psi_a \\ \psi_b \\ \psi_c \end{pmatrix} \tag{2.22}$$

2.5.1 Λ system and Raman transition

Raman transition requires a Λ system. For a Λ system, we assume $E_a < E_b < E_c$ and $V_{ab} = V_{ba} = 0$. Now the equation for ψ_a, ψ_b, and ψ_c becomes

$$\begin{aligned} i\hbar\dot{\psi_a} &= V_{ac}e^{i\omega_{ac}t}\psi_c \\ i\hbar\dot{\psi_b} &= V_{bc}e^{i\omega_{bc}t}\psi_c \\ i\hbar\dot{\psi_c} &= V_{ca}e^{i\omega_{ca}t}\psi_a + V_{cb}e^{i\omega_{cb}t}\psi_b \end{aligned} \tag{2.23}$$

When the electric field is far off resonant from neither $|a\rangle$ to $|c\rangle$ nor $|b\rangle$ to $|c\rangle$ transitions, the population of the excited state $|c\rangle$ is small and fast varying. Therefore, we can get the value of ψ_c by integrating the last differential equation of Equation 2.23 with the assumption of constant ψ_a and ψ_b [41]. We call this adiabatic elimination. Plugging ψ_c into the first two equations of Equation 2.23, we get

$$\begin{aligned} \dot{\psi_a} &= -\tilde{V_{ac}}e^{i\omega_{ac}t}\int_0^t \tilde{V_{ca}}e^{i\omega_{ca}\tau}d\tau \cdot \psi_a - \tilde{V_{ac}}e^{i\omega_{ac}t}\int_0^t \tilde{V_{cb}}e^{i\omega_{cb}\tau}d\tau \cdot \psi_b \\ \dot{\psi_b} &= -\tilde{V_{bc}}e^{i\omega_{bc}t}\int_0^t \tilde{V_{ca}}e^{i\omega_{ca}\tau}d\tau \cdot \psi_a - \tilde{V_{bc}}e^{i\omega_{bc}t}\int_0^t \tilde{V_{cb}}e^{i\omega_{cb}\tau}d\tau \cdot \psi_b \end{aligned} \tag{2.24}$$

where $\tilde{V_{ij}} = V_{ij}/\hbar$ and $i, j \in \{a, b, c\}$. The excited state is thus adiabatically eliminated and the 3-level system effectively becomes a 2-level system where the population transfer is between $|a\rangle$ and $|b\rangle$ states.

If $\vec{E} = E_1\vec{\epsilon_1}\cos(\omega_1 t + \phi_1) + E_2\vec{\epsilon_2}\cos(\omega_2 t + \phi_2)$, we have

$$\begin{aligned} \tilde{V_{ac}} &= \frac{\langle a|\vec{p}\cdot\vec{\epsilon_1}|c\rangle E_1}{\hbar}\cos(\omega_1 t + \phi_1) + \frac{\langle a|\vec{p}\cdot\vec{\epsilon_2}|c\rangle E_2}{\hbar}\cos(\omega_2 t + \phi_2) \\ \tilde{V_{ca}} &= \frac{\langle c|\vec{p}\cdot\vec{\epsilon_1}|a\rangle E_1}{\hbar}\cos(\omega_1 t + \phi_1) + \frac{\langle c|\vec{p}\cdot\vec{\epsilon_2}|a\rangle E_2}{\hbar}\cos(\omega_2 t + \phi_2) \\ \tilde{V_{bc}} &= \frac{\langle b|\vec{p}\cdot\vec{\epsilon_1}|c\rangle E_1}{\hbar}\cos(\omega_1 t + \phi_1) + \frac{\langle b|\vec{p}\cdot\vec{\epsilon_2}|c\rangle E_2}{\hbar}\cos(\omega_2 t + \phi_2) \\ \tilde{V_{cb}} &= \frac{\langle c|\vec{p}\cdot\vec{\epsilon_1}|b\rangle E_1}{\hbar}\cos(\omega_1 t + \phi_1) + \frac{\langle c|\vec{p}\cdot\vec{\epsilon_2}|b\rangle E_2}{\hbar}\cos(\omega_2 t + \phi_2) \end{aligned} \tag{2.25}$$

For simplicity and without loss of generality, we assume

$$\frac{\langle\alpha|\vec{p}\cdot\vec{\epsilon_i}|\beta\rangle E_i}{\hbar} = \frac{\langle\beta|\vec{p}\cdot\vec{\epsilon_i}|\alpha\rangle E_i}{\hbar} = \Omega_i^{\alpha\beta}$$

where $\alpha, \beta \in \{a, b, c\}$ and $i \in \{1, 2\}$. With this assumption and using RWA by ignoring all the fast rotating terms except the slowest one (compared to the evolution of the state population) in

Equation 2.24, we get

$$\begin{aligned}
&-\tilde{V_{ac}}e^{i\omega_{ac}t}\int_0^t \tilde{V_{ca}}e^{i\omega_{ca}\tau}d\tau = i\frac{(\Omega_1^{ac})^2}{4(\omega_{ca}-\omega_1)} + i\frac{(\Omega_2^{ac})^2}{4(\omega_{ca}-\omega_2)}\\
&-\tilde{V_{ac}}e^{i\omega_{ac}t}\int_0^t \tilde{V_{cb}}e^{i\omega_{cb}\tau}d\tau = i\frac{e^{i(\phi_1-\phi_2)}\Omega_1^{ac}\Omega_2^{bc}}{4(\omega_{cb}-\omega_2)}e^{i\delta t}\\
&-\tilde{V_{bc}}e^{i\omega_{bc}t}\int_0^t \tilde{V_{ca}}e^{i\omega_{ca}\tau}d\tau = i\frac{e^{i(-\phi_1+\phi_2)}\Omega_1^{ac}\Omega_2^{bc}}{4(\omega_{ca}-\omega_1)}e^{-i\delta t}\\
&-\tilde{V_{bc}}e^{i\omega_{bc}t}\int_0^t \tilde{V_{cb}}e^{i\omega_{cb}\tau}d\tau = i\frac{(\Omega_1^{bc})^2}{4(\omega_{cb}-\omega_1)} + i\frac{(\Omega_2^{bc})^2}{4(\omega_{cb}-\omega_2)}
\end{aligned} \tag{2.26}$$

where $\delta = -\omega_{ca}+\omega_{cb}+\omega_1-\omega_2$.

Using the conventions in Figure 2.5, we have $\omega_{ca}-\omega_1 = \Delta$, $\omega_{cb}-\omega_2 = \Delta+\delta$, and $\omega_{ca}-\omega_{cb} = \omega_{HF}$. Assuming $\delta \ll \Delta$, $\omega_{cb}-\omega_2 \approx \omega_{ca}-\omega_1 = \Delta$. Thus, Equation 2.24 becomes:

$$\begin{pmatrix}\dot{\psi}_a\\ \dot{\psi}_b\end{pmatrix} = i\begin{pmatrix} A & Be^{\delta t}\\ B^* e^{-\delta t} & D\end{pmatrix}\begin{pmatrix}\psi_a\\ \psi_b\end{pmatrix} \tag{2.27}$$

where

$$\begin{aligned}
A &= \frac{(\Omega_1^{ac})^2}{4\Delta} + \frac{(\Omega_2^{ac})^2}{4(\Delta+\omega_{HF})}\\
B &= \frac{\Omega_1^{ac}\Omega_2^{bc}}{4\Delta}e^{i(\phi_1-\phi_2)}\\
D &= \frac{(\Omega_1^{bc})^2}{4(\Delta-\omega_{HF})} + \frac{(\Omega_2^{bc})^2}{4\Delta}.
\end{aligned} \tag{2.28}$$

We apply transformation Equation 2.13 with $\eta = \delta/2$ to Equation 2.27 and get:

$$\begin{pmatrix}\dot{\tilde{\psi}}_a\\ \dot{\tilde{\psi}}_b\end{pmatrix} = i\begin{pmatrix} A-\frac{\delta}{2} & B\\ B^* & D+\frac{\delta}{2}\end{pmatrix}\begin{pmatrix}\tilde{\psi}_a\\ \tilde{\psi}_b\end{pmatrix}. \tag{2.29}$$

Thus, the 3-level system is solved as rotations on a Bloch sphere see Equation 2.12. The effective Rabi frequency of the interaction is

$$\Omega_{\text{Rabi}}^{\text{effective}} = \frac{\Omega_1^{ac}\Omega_2^{bc}}{2\Delta}$$

and the detuning is

$$\frac{(\Omega_1^{bc})^2}{4(\Delta-\omega_{HF})} + \frac{(\Omega_2^{bc})^2}{4\Delta} - \frac{(\Omega_1^{ac})^2}{4\Delta} - \frac{(\Omega_2^{ac})^2}{4(\Delta+\omega_{HF})} + \delta.$$

We call

$$\Delta\omega_{\text{stark}}^{\text{AC}} = \frac{(\Omega_1^{bc})^2}{4(\Delta-\omega_{HF})} + \frac{(\Omega_2^{bc})^2}{4\Delta} - \frac{(\Omega_1^{ac})^2}{4\Delta} - \frac{(\Omega_2^{ac})^2}{4(\Delta+\omega_{HF})}$$

the differential AC stark shift.

2.5.2 Λ system with multiple excited states

If we consider the hyperfine splittings of state $5^2P_{3/2}$, we are actually dealing with a Λ system with multiple excited states.

In this case, the excited state $|c\rangle$ has multiple splittings $|c_1\rangle$,$|c_2\rangle$,...,$|c_n\rangle$ and Equation 2.23 becomes

$$\begin{aligned}
i\hbar\dot{\psi_a} &= \sum_{k=1}^{n} V_{ac_k} e^{i\omega_{ac_k}t}\psi_{c_k} \\
i\hbar\dot{\psi_b} &= \sum_{k=1}^{n} V_{bc_k} e^{i\omega_{bc_k}t}\psi_{c_k} \\
i\hbar\dot{\psi_{c_k}} &= V_{c_k a} e^{i\omega_{c_k a}t}\psi_a + V_{c_k b} e^{i\omega_{c_k b}t}\psi_b.
\end{aligned} \tag{2.30}$$

Adiabatically eliminating all the excited states, the equations for ψ_a and ψ_b become

$$\begin{aligned}
\dot{\psi_a} &= -\sum_{k=1}^{n} \tilde{V_{ac_k}} e^{i\omega_{ac_k}t}\int_0^t \tilde{V_{c_k a}} e^{i\omega_{c_k a}\tau}d\tau\cdot\psi_a - \sum_{k=1}^{n} \tilde{V_{ac_k}} e^{i\omega_{ac_k}t}\int_0^t \tilde{V_{c_k b}} e^{i\omega_{c_k b}\tau}d\tau\cdot\psi_b \\
\dot{\psi_b} &= -\sum_{k=1}^{n} \tilde{V_{bc_k}} e^{i\omega_{bc_k}t}\int_0^t \tilde{V_{c_k a}} e^{i\omega_{c_k a}\tau}d\tau\cdot\psi_a - \sum_{k=1}^{n} \tilde{V_{bc_k}} e^{i\omega_{bc_k}t}\int_0^t \tilde{V_{c_k b}} e^{i\omega_{c_k b}\tau}d\tau\cdot\psi_b.
\end{aligned} \tag{2.31}$$

If $\vec{E} = E_1\vec{\epsilon_1}\cos(\omega_1 t + \phi_1) + E_2\vec{\epsilon_2}\cos(\omega_2 t + \phi_2)$, we have

$$\begin{aligned}
\tilde{V_{ac_k}} &= \frac{\langle a|\vec{p}\cdot\vec{\epsilon_1}|c_k\rangle E_1}{\hbar}\cos(\omega_1 t + \phi_1) + \frac{\langle a|\vec{p}\cdot\vec{\epsilon_2}|c_k\rangle E_2}{\hbar}\cos(\omega_2 t + \phi_2) \\
\tilde{V_{c_k a}} &= \frac{\langle c_k|\vec{p}\cdot\vec{\epsilon_1}|a\rangle E_1}{\hbar}\cos(\omega_1 t + \phi_1) + \frac{\langle c_k|\vec{p}\cdot\vec{\epsilon_2}|a\rangle E_2}{\hbar}\cos(\omega_2 t + \phi_2) \\
\tilde{V_{bc_k}} &= \frac{\langle b|\vec{p}\cdot\vec{\epsilon_1}|c_k\rangle E_1}{\hbar}\cos(\omega_1 t + \phi_1) + \frac{\langle b|\vec{p}\cdot\vec{\epsilon_2}|c_k\rangle E_2}{\hbar}\cos(\omega_2 t + \phi_2) \\
\tilde{V_{c_k b}} &= \frac{\langle c_k|\vec{p}\cdot\vec{\epsilon_1}|b\rangle E_1}{\hbar}\cos(\omega_1 t + \phi_1) + \frac{\langle c_k|\vec{p}\cdot\vec{\epsilon_2}|b\rangle E_2}{\hbar}\cos(\omega_2 t + \phi_2).
\end{aligned} \tag{2.32}$$

For simplicity and without loss of generality, we assume

$$\frac{\langle\alpha|\vec{p}\cdot\vec{\epsilon_i}|\beta\rangle E_i}{\hbar} = \frac{\langle\beta|\vec{p}\cdot\vec{\epsilon_i}|\alpha\rangle E_i}{\hbar} = \Omega_i^{\alpha\beta}$$

where $\alpha, \beta \in \{a, b, c_k\}$ and $i \in \{1, 2\}$. With this assumption and using RWA by ignoring all the fast rotating terms except the slowest one in Equation 2.31, we get

$$\begin{aligned}
-\sum_{k=1}^{n} \tilde{V}_{ac_k} e^{i\omega_{ac_k} t} \int_0^t \tilde{V}_{c_k a} e^{i\omega_{c_k a}\tau} d\tau &= i\sum_{k=1}^{n} [\frac{(\Omega_1^{ac_k})^2}{4(\omega_{c_k a} - \omega_1)} + \frac{(\Omega_2^{ac_k})^2}{4(\omega_{c_k a} - \omega_2)}] \\
-\sum_{k=1}^{n} \tilde{V}_{ac_k} e^{i\omega_{ac_k} t} \int_0^t \tilde{V}_{c_k b} e^{i\omega_{c_k b}\tau} d\tau &= i\sum_{k=1}^{n} \frac{e^{i(\phi_1 - \phi_2)}\Omega_1^{ac_k}\Omega_2^{bc_k}}{4(\omega_{c_k b} - \omega_2)} e^{i\delta t} \\
-\sum_{k=1}^{n} \tilde{V}_{bc_k} e^{i\omega_{bc_k} t} \int_0^t \tilde{V}_{c_k a} e^{i\omega_{c_k a}\tau} d\tau &= i\sum_{k=1}^{n} \frac{e^{i(-\phi_1 + \phi_2)}\Omega_1^{ac_k}\Omega_2^{bc_k}}{4(\omega_{c_k a} - \omega_1)} e^{-i\delta t} \\
-\sum_{k=1}^{n} \tilde{V}_{bc_k} e^{i\omega_{bc_k} t} \int_0^t \tilde{V}_{c_k b} e^{i\omega_{c_k b}\tau} d\tau &= i\sum_{k=1}^{n} [\frac{(\Omega_1^{bc_k})^2}{4(\omega_{c_k b} - \omega_1)} + \frac{(\Omega_2^{bc_k})^2}{4(\omega_{c_k b} - \omega_2)}]
\end{aligned} \tag{2.33}$$

where $\delta = -\omega_{c_k a} + \omega_{c_k b} + \omega_1 - \omega_2$.

Using the conventions in Figure 2.5, $\omega_{c_k a} - \omega_1 = \Delta_k$, $\omega_{c_k b} - \omega_2 = \Delta_k + \delta$, and $\omega_{c_k a} - \omega_{c_k b} = \omega_{HF}$. Assuming $\delta \ll \Delta_k$, $\omega_{c_k b} - \omega_2 \approx \omega_{c_k a} - \omega_1 = \Delta_k$. Thus, the effective Rabi frequency of the interaction $\Omega_{\text{Rabi}}^{\text{effective}}$ is

$$\Omega_{\text{Rabi}}^{\text{effective}} = \sum_{k=1}^{n} \frac{\Omega_1^{ac_k}\Omega_2^{bc_k}}{2\Delta_k}$$

and the AC stark shift $\Delta\omega_{\text{stark}}^{\text{AC}}$ is

$$\Delta\omega_{\text{stark}}^{\text{AC}} = \sum_{k=1}^{n} [\frac{(\Omega_1^{bc_k})^2}{4(\Delta_k - \omega_{HF})} + \frac{(\Omega_2^{bc_k})^2}{4\Delta_k} - \frac{(\Omega_1^{ac_k})^2}{4\Delta_k} - \frac{(\Omega_2^{ac_k})^2}{4(\Delta_k + \omega_{HF})}].$$

The effects of multiple excited states in real ^{87}Rb atoms are shown in the Appendix A.

2.5.3 Λ system with multiple driving fields

In our experiment, we use multiple frequency components to drive the Raman transition in order to balance the AC stark shift. We examine the theory for Λ system interacting with multiple frequency components.

For multiple driving fields $\vec{E} = \sum_{s=1}^{m} E_s \vec{\epsilon_s} \cos(\omega_s t + \phi_s)$, we have

$$
\begin{aligned}
\tilde{V_{ac}} &= \sum_{s=1}^{m} \frac{\langle a|\vec{p}\cdot\vec{\epsilon_s}|c\rangle E_s}{\hbar} \cos(\omega_s t + \phi_s) \\
\tilde{V_{ca}} &= \sum_{s=1}^{m} \frac{\langle c|\vec{p}\cdot\vec{\epsilon_s}|a\rangle E_s}{\hbar} \cos(\omega_s t + \phi_s) \\
\tilde{V_{bc}} &= \sum_{s=1}^{m} \frac{\langle b|\vec{p}\cdot\vec{\epsilon_s}|c\rangle E_s}{\hbar} \cos(\omega_s t + \phi_i) \\
\tilde{V_{cb}} &= \sum_{s=1}^{m} \frac{\langle c|\vec{p}\cdot\vec{\epsilon_s}|b\rangle E_s}{\hbar} \cos(\omega_s t + \phi_s)
\end{aligned}
\tag{2.34}
$$

Assuming $\frac{\langle\alpha|\vec{p}\cdot\vec{\epsilon_s}|\beta\rangle E_s}{\hbar} = \frac{\langle\beta|\vec{p}\cdot\vec{\epsilon_s}|\alpha\rangle E_s}{\hbar} = \Omega_s^{\alpha\beta}$ where $\alpha, \beta \in \{a, b, c\}$ and $s \in \{1, 2, ...m\}$, we solve for the integrations in Equation 2.26. The solutions contain multiple time-dependent terms that can not be dropped easily. The simplest case where we neglect all the fast varying terms except the slowest one is shown below:

$$
\begin{aligned}
-\tilde{V_{ac}} e^{i\omega_{ac} t} \int_0^t \tilde{V_{ca}} e^{i\omega_{ca}\tau} d\tau &= \frac{i}{4} \sum_{s=1}^{m} \frac{(\Omega_s^{ac})^2}{\omega_{ca} - \omega_s} \\
-\tilde{V_{ac}} e^{i\omega_{ac} t} \int_0^t \tilde{V_{cb}} e^{i\omega_{cb}\tau} d\tau &= \frac{i}{4} \sum_{\langle s,p\rangle}^{m} \frac{e^{i(-\phi_p+\phi_s)} \Omega_s^{ac} \Omega_p^{bc}}{\omega_{cb} - \omega_p} e^{i\delta t} \\
-\tilde{V_{bc}} e^{i\omega_{bc} t} \int_0^t \tilde{V_{ca}} e^{i\omega_{ca}\tau} d\tau &= \frac{i}{4} \sum_{\langle s,p\rangle}^{m} \frac{e^{-i(-\phi_p+\phi_s)} \Omega_s^{ac} \Omega_p^{bc}}{\omega_{ca} - \omega_s} e^{-i\delta t} \\
-\tilde{V_{bc}} e^{i\omega_{bc} t} \int_0^t \tilde{V_{cb}} e^{i\omega_{cb}\tau} d\tau &= \frac{i}{4} \sum_{s=1}^{m} \frac{(\Omega_s^{bc})^2}{\omega_{cb} - \omega_s}
\end{aligned}
\tag{2.35}
$$

where the sum $\sum_{\langle s,p\rangle}^{m}$ is over $\langle s, p\rangle$ pairs that satisfy the frequency relation $\delta = -\omega_{ca} + \omega_{cb} + \omega_s - \omega_p$. This result shows that the Rabi frequency of the Raman transition between $|a\rangle$ and $|b\rangle$ is a result of interference between different frequency pairs. In real experiment, there are cases where we need to consider more time-dependent terms besides the slowest one, the situation is more complicated and will be discussed in subsection 6.4.1.

2.5.4 Λ system with multiple driving fields and multiple excited states

For this case, we combine the results of Equation 2.35 and Equation 2.31. We get:

$$\begin{aligned}
-\sum_{k=1}^{n}\tilde{V_{ac_k}}e^{i\omega_{ac_k}t}\int_0^t\tilde{V_{c_ka}}e^{i\omega_{c_ka}\tau}d\tau &= \frac{i}{4}\sum_{k=1}^{n}\sum_{s=1}^{m}\frac{(\Omega_s^{ac_k})^2}{\omega_{c_ka}-\omega_s}\\
-\sum_{k=1}^{n}\tilde{V_{ac_k}}e^{i\omega_{ac_k}t}\int_0^t\tilde{V_{c_kb}}e^{i\omega_{c_kb}\tau}d\tau &= \frac{i}{4}\sum_{k=1}^{n}\sum_{\langle s,p\rangle}^{m}\frac{e^{i(-\phi_p+\phi_s)}\Omega_s^{ac_k}\Omega_p^{bc_k}}{\omega_{c_kb}-\omega_p}e^{i\delta t}\\
-\sum_{k=1}^{n}\tilde{V_{bc_k}}e^{i\omega_{bc_k}t}\int_0^t\tilde{V_{c_ka}}e^{i\omega_{c_ka}\tau}d\tau &= \frac{i}{4}\sum_{k=1}^{n}\sum_{\langle s,p\rangle}^{m}\frac{e^{-i(-\phi_p+\phi_s)}\Omega_s^{ac_k}\Omega_p^{bc_k}}{\omega_{c_ka}-\omega_s}e^{-i\delta t}\\
-\sum_{k=1}^{n}\tilde{V_{bc_k}}e^{i\omega_{bc_k}t}\int_0^t\tilde{V_{c_kb}}e^{i\omega_{c_kb}\tau}d\tau &= \frac{i}{4}\sum_{k=1}^{n}\sum_{s=1}^{m}\frac{(\Omega_s^{bc_k})^2}{\omega_{c_kb}-\omega_s}
\end{aligned} \tag{2.36}$$

where the sum $\sum_{\langle s,p\rangle}^{m}$ is over $\langle s,p\rangle$ pairs that satisfy the frequency relation $\delta = -\omega_{c_ka}+\omega_{c_kb}+\omega_s-\omega_p$.

2.6 Quantum Nondemolition Measurement for Spin Squeezing

In our experiment, we prepare spin squeezed states by applying a quantum nondemolition (QND) measurement on J_z [42]. This measurement-based quantum state preparation can be understood by an extreme case where we apply a strong projective measurement on J_z. In this case, the quantum state of the system will be projected onto an eigenstate of J_z, giving zero J_z uncertainty after the measurement. If we apply a slightly weaker measurement on J_z instead of a strong projective measurement, we will expect that the J_z uncertainty to be slightly larger than zero but still small compared to the quantum projection limit.

2.6.1 Introduction to quantum nondemolition measurement

In quantum mechanics, the measurement of one observable usually introduces perturbations, yielding different results for successive measurement of the same observable. For example, when measuring the position observable of a free particle to an arbitrary precision, this measurement perturbs the momentum observable as required by the Heisenberg uncertainty principle. This perturbation ruins the precision for the next position measurement. In order to avoid the back action of the measuring process, QND scheme is proposed. In a QND measurement, an observable can be measured repeatedly with the result completely determined by an initial precise measurement.

To describe this model or in general to describe a quantum measurement scheme, we have a signal observable A_S and a probe observable A_P. The signal observable A_S is measured by detecting a change in A_P during the measurement time. This change is induced by the coupling between the signal and the probe systems. During the measurement process, the signal and the probe systems are coupled, the coupled system evolves under Hamiltonian $H = H_S + H_P + H_I$ where H_S and H_P are Hamiltonians for the signal and the probe respectively, and H_I describes the interaction (coupling) between the two. The equations of motion for the signal observable A_S and probe observable A_P are

$$i\hbar \dot{A_S} = [A_S, H_S + H_I] \tag{2.37}$$

$$i\hbar \dot{A_P} = [A_P, H_P + H_I] \tag{2.38}$$

since $[A_S, H_P] = [A_P, H_S] = 0$.

For a QND measurement, the Hamiltonians have to satisfy [38]:

1. $\frac{\partial H_I}{\partial A_S} \neq 0$ because the signal information is extracted through its coupling to the probe system. This coupling is described by H_I, so H_I has to be a function of A_S.
2. $[A_P, H_I] \neq 0$ because A_P is used to extract information of the signal through H_I, H_I has to be able to affect the evolution of A_P.
3. $[A_S, H_I] = 0$ because the measurement process takes no effect on the signal evolution as required by QND.
4. $\frac{\partial H_S}{\partial A_S^C} = 0$ where A_S^C is the conjugate observable of A_S. This requirement ensures that evolution of A_S is not affected by its own measurement through the back action on A_S^C.

2.6.2 Cavity J_z measurement

In this work, the signal observable for the QND measurement is J_z and the probe observable is an optical mode. The optical mode is formed by an optical cavity and is detuned right between the two magnetically insensitive hyperfine ground states and the excited state $5^2P_{3/2}$ as shown by Figure 2.6. This means this cavity mode is blue detuned by Δ from the $|F = 2, m_F = 0\rangle$ to the excited state transition and red detuned by the same amount from the $|F = 1, m_F = 0\rangle$ to the excited state transition. This detuning is much larger than the hyperfine splittings of the excited state. The relevant interaction Hamiltonian is

$$H_I = \hbar \frac{2g^2}{\Delta} a a^\dagger J_z \tag{2.39}$$

where a and $a^\dagger$ are the annihilation and creation operators for the cavity mode respectively, and g is half the vacuum Rabi frequency that quantifies the interaction strength. In addition, $H_P = \hbar\omega a a^\dagger$ and $H_S = \omega_0 J_z$ where ω is the frequency of the cavity mode and ω_0 is the frequency difference

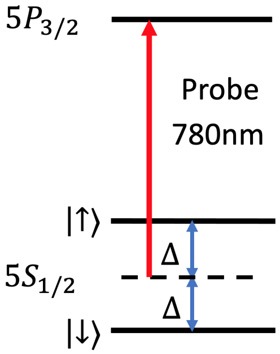

Figure 2.6: Probe detuning. The 780nm probe is detuned right between the two magnetically insensitive hyperfine ground states and the excited state $5P_{3/2}$. The detuning is Δ and blue detuning represents a positive value.

between $|\uparrow\rangle$ and $|\downarrow\rangle$ [43]. We can check that the Hamiltonian H_I and H_S satisfy all conditions for a QND measurement.

This interaction Hamiltonian tells that the coupling of the cavity mode to the atoms introduces a differential AC stark shift between the $|\uparrow\rangle$ and $|\downarrow\rangle$ states that is proportional to the photon number $aa^\dagger$. The photon number fluctuation leads to fluctuation on the AC stark shift, which causes a phase smear between the two ground states. This smear increases the quantum noise on J_y, giving rise to anti-squeezing. The interaction Hamiltonian also tells that this coupling introduces a shift on the cavity resonance frequency which is proportional to J_z. Thus, J_z is measured by measuring this cavity shift.

Since $J_z = (N_\uparrow - N_\downarrow)/2$ where $N_\uparrow$ ($N_\downarrow$) is the number of atoms in the $|\uparrow\rangle$ ($|\downarrow\rangle$) state, this interaction Hamiltonian can be written as

$$H_I = \hbar a a^\dagger \left(\frac{g^2}{\Delta} N_\uparrow + \frac{g^2}{-\Delta} N_\downarrow\right). \tag{2.40}$$

We can understand this interaction as a $|\uparrow\rangle$ atom shifts the cavity resonance frequency by g^2/Δ and a $|\downarrow\rangle$ atom shifts the cavity resonance frequency by $g^2/(-\Delta)$ where Δ $(-\Delta)$ is the detuning between the cavity mode and the $|\uparrow\rangle$ ($|\downarrow\rangle$) to the excited state transition. This cavity shifts by atoms at different ground states are given by Equation 2.21 in the low excitation limit (the excited state population is negligible). In cases where the detuning of the cavity mode is slightly off from the symmetric scheme, i.e. $\Delta \to \Delta + \delta$ and $-\Delta \to -(\Delta - \delta)$, the Hamiltonian becomes

$$H_I = \hbar a a^\dagger \left(\frac{g^2}{\Delta + \delta} N_\uparrow - \frac{g^2}{\Delta - \delta} N_\downarrow\right). \tag{2.41}$$

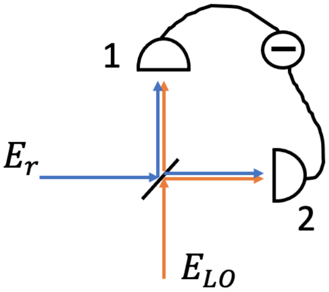

Figure 2.7: An illustration of the homodyne method that shows the signal field E_r, the local oscillator field E_{LO}, a beamsplitter that mixes the two fields, and a balanced photodiode. E_r and E_{LO} have the same frequency. 1 and 2 are two output ports. In our experiment, E_r is the electric field of the reflected mode.

This has a noticeable effect on the squeezing result and is discussed in subsection 5.4.2.

2.6.3 Homodyne method to measure cavity frequency shift

The cavity frequency shift is measured by a homodyne method. In this method, the reflected mode by the optical cavity carries the information about the cavity frequency shift and is mixed with a local oscillator at the same frequency by a beamsplitter as shown in Figure 2.7. The homodyne method measures the power difference between port 1 and 2 and is called balanced homodyne. I next derive the expression for the power difference.

We assume $E_r = A_r e^{i\phi_r}$, $E_{LO} = A_{LO}e^{i\phi_{LO}}$, and the beam splitter is a 50-50 dielectric beam splitter. Thus, the reflected and transmitted beams have a phase difference of $\pi/2$. The electric field at port 1 and 2 are

$$\begin{aligned} E_1 &= \frac{A_r}{2}e^{i(\phi_r+\pi/2)} + \frac{A_{LO}}{2}e^{i\phi_{LO}} \\ E_2 &= \frac{A_r}{2}e^{i\phi_r} + \frac{A_{LO}}{2}e^{i(\phi_{LO}+\pi/2)}. \end{aligned} \tag{2.42}$$

The power difference P_{12} is proportional to $|E_1|^2 - |E_2|^2$, i.e.

$$P_{12} \propto |E_1|^2 - |E_2|^2 = A_r A_{LO}(\cos\phi_{LO}\sin\phi_r - \sin\phi_{LO}\cos\phi_r). \tag{2.43}$$

Now I relate the phase ϕ_r to the cavity frequency shift using the cavity frequency response.

The electric field of the reflected beam E_r relates to that of the incident beam E_{in} by $E_r = E_{in}r_{cav}$ where r_{cav} is the reflection coefficient of the cavity. Assuming the phase of the incident beam is 0, then, $A_r sin\phi_r = E_{in}\Im[r_{cav}]$ and $A_r cos\phi_r = E_{in}\Re[r_{cav}]$ where $\Im[r_{cav}]$ is the imaginary part of r_{cav} and $\Re[r_{cav}]$ is the real part of r_{cav}. The real and imaginary parts of r_{cav} are

$$\Re[r_{cav}] = \frac{\kappa_L}{\kappa}\frac{1}{1+(\frac{\delta}{\kappa/2})^2} \tag{2.44}$$

$$\Im[r_{cav}] = -\frac{\kappa_0}{\kappa}\frac{\frac{\delta}{\kappa/2}}{1+(\frac{\delta}{\kappa/2})^2} \tag{2.45}$$

where κ_L is the rate of loss from the cavity mode, κ is the cavity linewidth, κ_0 is the cavity linewidth without loss, and δ is the detuning from the cavity resonance frequency [44]. Since the optical mode is set on resonance with the cavity when no atoms exist, the cavity frequency shift due to the atoms is the same as the detuning δ. Equation 2.45 tells us that when δ is small, $\Im[r_{cav}] = -\kappa_0\delta/(\kappa^2/2)$. Thus, when $\phi_{LO} = 0$, $P_{12} \propto A_{LO}A_r sin\phi_r = A_{LO}E_{in}\Im[r_{cav}] = -A_{LO}E_{in}\kappa_0\delta/(\kappa^2/2)$. We can measure the cavity frequency shift by measuring the power difference at the two output ports of the homodyne setup when the cavity frequency shift is small. The maximum cavity frequency shift that can be measured by the homodyne method is limited by the cavity linewidth.

2.6.4 Back-to-back measurement

To demonstrate spin squeezing generated by QND measurement, we need to apply two J_z measurement back-to-back. The first measurement measures a CSS and at the same time prepares the state to a SSS. The second measurement measures the SSS and reads out the state. The results of the two measurements are similar because the first measurement is QND. Spin squeezing is revealed by taking the subtraction of the two results. The difference between the two measurement results is given by photon shot noise and spin flip noise. These two noise sources are what limit the spin squeezing in our system [44, 24].

2.7 One-axis Twisting for Spin Squeezing

Originally described in [34], Kitagawa et al. proposed a Hamiltonian proportional to J_z^2 that generates unconditional squeezing. In our experiment where atoms interact with an optical cavity mode, this J_z^2 Hamiltonian is created by light that is detuned from the cavity mode [45]. This comes from the dispersive atom-light interaction Hamiltonian Equation 2.39. This Hamiltonian tells that the cavity resonance frequency is modified by atoms by an amount proportional to J_z. When the cavity input mode is tuned to the side of the cavity response, i.e. detuned from the cavity resonance, the intracavity photon number $\langle aa^\dagger \rangle$ changes linearly with the detuning due to the atoms that is proportional to J_z. Combined with the J_z term in the dispersive Hamiltonian, this gives the J_z^2 dependence. This J_z^2 Hamiltonian generates a J_z dependent phase shift on the quantum state (CSS), thus twisting the atomic state around J_z. After this twisting, a microwave rotation around

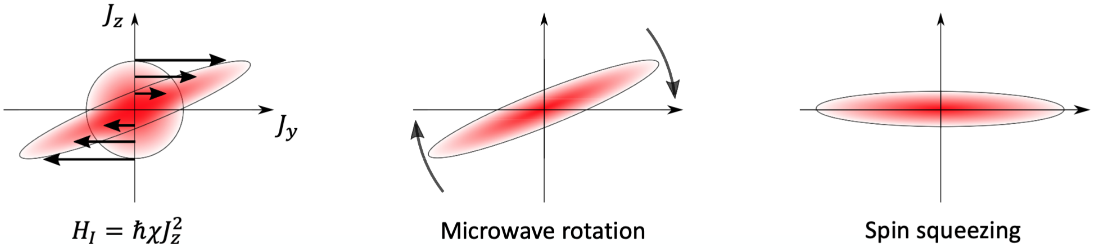

Figure 2.8: One-axis twisting for spin squeezing. The CSS is first sheared by a nonlinear Hamiltonian $H_I = \hbar\chi J_z^2$. Then the sheared state is rotated by a microwave around its center until the minimum J_z noise is reached. This is used as the presqueezing procedure.

the center of the state by a small amount is implemented to minimize the J_z noise. For specific angles the J_z noise can be below QPN. This process is shown in Figure 2.8. We use this method as a presqueezing procedure while the main squeezing is done by a QND measurement, because the QND measurement generates larger values of squeezing than one-axis twisting (details about presqueezing can be seen in subsection 3.5.2).

2.8 Atomic Clock

Atomic clocks offer time standards by comparing a local oscillator frequency to some atomic transition frequency and locking the local oscillator frequency to the atomic transition [46]. The local oscillator is a form of electromagnetic radiations. For hyperfine transitions, the local oscillator is in the microwave domain. For electron transitions, the local oscillator is in the optical domain. The local oscillator and atomic transition frequencies are compared by observing the excitation probability when the atoms interact with the local oscillator. The excitation probability depends on the frequency difference or we call it detuning. When on resonance (detuning equals to 0), the excitation probability is maximized. When detuning increases, the excitation probability decreases accordingly depending on the interaction sequence. The frequency spread is the full width half maximum (FWHM) of the excitation probability curve. The smaller the frequency spread, the easier it is to distinguish the detuning.

A simple interaction sequence is to interact atoms with a square pulse of radiation, i.e. an oscillating field of constant amplitude from time $t = 0$ to $t = \Delta t$. The frequency spread Δf is $1/\Delta t$. This is called Rabi sequence. A more common interaction sequence is to interact atoms with two $\pi/2$ pulses of length Δt and separated by time T. Here, the $\pi/2$ pulse is a pulse that rotates the state by $\pi/2$ in the Bloch sphere representation. In this case, the envelope of the excitation probability curve has a spread approximate to $1/\Delta t$ and the frequency spread is $1/(2T)$ [47]. The resolution of a Ramsey sequence increases by a factor of 2 compared to a Rabi sequence whose pulse length is the same as the pulse separation in the Ramsey sequence.

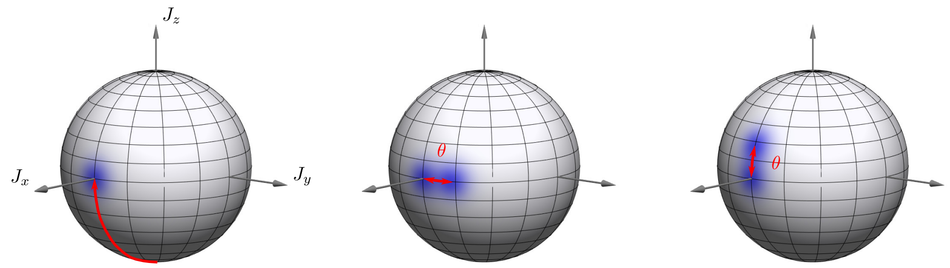

Figure 2.9: Ramsey spectroscopy for CSS. The state is brought from the bottom of the Bloch sphere to the equator by the first microwave $\pi/2$ pulse. During the interrogation time, the state accumulates a phase θ. The last microwave $\pi/2$ pulse converts the accumulated phase into population difference for the final measurement.

2.8.1 Ramsey spectroscopy

Ramsey spectroscopy compares the local oscillator frequency to the atomic transition frequency. It is used in atomic clocks to generate error signals for locking. Ramsey spectroscopy includes two microwave $\pi/2$ pulses described in the previous section as Ramsey sequence. The time between the two microwave pulses is called interrogation time. We denote it as T_{int}. Using the Bloch sphere representation, a coherent state under Ramsey spectroscopy is illustrated in Figure 2.9. The first $\pi/2$ pulse brings the atom state from the bottom of the Bloch sphere to the equator. The atom state then starts accumulating phase θ based on the detuning for time T_{int}. Finally, another $\pi/2$ pulse with a $\pi/2$ phase shift from the first $\pi/2$ pulse transforms the accumulated phase difference θ into population difference that can be experimentally measured. The accumulated phase θ is related to the final J_z by

$$\theta = \frac{J_z}{C(N/2)} \tag{2.46}$$

where C is the coherence of the atoms and N is the atom number.

2.8.2 Ramsey spectroscopy below quantum projection limit

We apply spin squeezing to free space Ramsey spectroscopy to demonstrate a proof-of-principle atomic fountain clock sequence that is below quantum projection limit. For this spin squeezed Ramsey spectroscopy, the atom state is initially prepared at $J_z = 0$ (on the equator of the Bloch sphere) and is spin squeezed. The first $\pi/2$ pulse rotates the state around its center and brings the state into a phase sensitive state. The phase sensitive state then accumulates a phase θ during the interrogation time T_{int}. The last $\pi/2$ with a π phase shift from the first $\pi/2$ pulse transforms

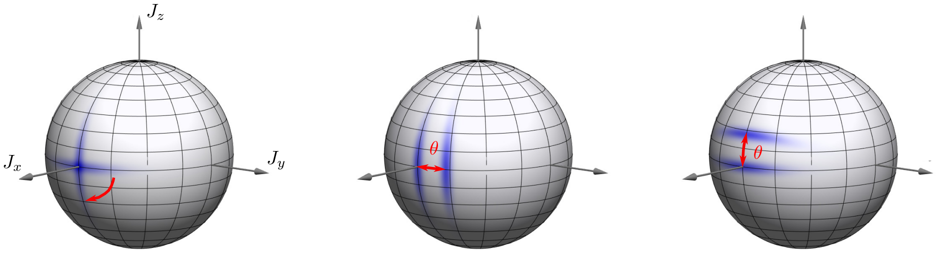

Figure 2.10: Ramsey spectroscopy for SSS. The first microwave $\pi/2$ pulse rotates the state from SSS to a phase sensitive state. During the interrogation time, the state acquires a phase θ. The last microwave $\pi/2$ pulse rotates the state back to SSS for the final measurement.

this accumulated phase into population difference. This process is shown in Figure 2.10. Compared to the coherent state clock shown in Figure 2.9, the squeezed clock has better resolution on the population difference, thus, better resolution on the accumulated phase. The accumulated phase θ is related to J_z by

$$\theta = \frac{J_z^{(2)} - J_z^{(1)}}{C(N/2)} \tag{2.47}$$

where $J_z^{(2)}$ and $J_z^{(1)}$ are the results of the first and second J_z measurements.

2.8.3 Allan variance

Allan variance characterizes the fractional frequency stability in clocks. It is defined as

$$\sigma_y^2(\tau) = \frac{1}{2(M-1)} \sum_{k=1}^{M-1} (\bar{y}_{k+1} - \bar{y}_k)^2 \tag{2.48}$$

where τ is the averaging time, $M = \text{floor}(T_{tot}/\tau)$ is the number of averaged samples (floor is a function that rounds its input to the nearest integer less than or equal to that input), T_{tot} is the total data collection time, and

$$\bar{y}_k = \frac{1}{L} \sum_{i=1}^{L} \phi((k-1)\tau + iT_c) \tag{2.49}$$

where $L = \tau/T_c$ is the size of each sample, T_c is the experimental cycle time that includes the measurement time T_{int} and the dead time, and

$$\phi(t) = \frac{\theta}{T_{int}\omega_0} \tag{2.50}$$

is the fractional frequency and ω_0 is the atomic transition frequency.

Allan deviation is the square root of Allan variance. An Allan deviation of $\sigma_y(\tau)$ can be interpreted as a fractional frequency instability between two observations τ apart with a relative root mean square of $\sigma_y(\tau)$. Thus if we have a clock with Allan deviation $\sigma_y(\tau)$ and running at frequency ν_0, its frequency will jitter by $\nu_0\sigma_y(\tau)$ within time τ. This means the period will jitter by $\sigma_y(\tau)/\nu_0$ from the original period of $1/\nu_0$. Thus, it will take the clock $1/\sigma_y(\tau)$ seconds to lose 1 second. Allan deviation directly tells the time keeping ability of a clock.

2.8.4 Clock enhancement

The Allan deviation of an atomic clock at the quantum projection limit is [46]:

$$\sigma_y^{(CSS)}(\tau) = \frac{1}{\omega_0 T_{int}}\sqrt{\frac{T_c}{N\tau}}. \tag{2.51}$$

To characterize clock enhancement, we compare the Allan deviation of a spin squeezed clock at $\tau = T_c$ to the quantum projection limit, i.e.

$$\xi_y^2 = \frac{\sigma_y^2(\tau = T_c)}{\sigma_y^{2(CSS)}(\tau = T_c)}. \tag{2.52}$$

2.9 Atom interferometer

Similar to optical interferometers that measure the phase of the optical waves, atom interferometers measure the phase difference of the atomic matter waves along different paths [48, 49, 50]. The optical interferometers use mirrors and beamsplitters to manipulate the states of the optical waves. In our experiments, the atomic counterparts of mirrors and beamsplitters for atom interferometers are π and $\pi/2$ laser pulses formed by Raman transitions (detailed in section 2.5). I will discuss the phase of the atomic matter waves and how it is measured by an atom interfereometer in this section.

2.9.1 Phase due to propagations

In the previous sections, only the internal degrees of freedom of a quantum state were discussed. We denoted the internal quantum state as $|\psi(t)\rangle$. The phase evolution of $|\psi(t)\rangle$ only depends on the internal energy. Now, we take the external degrees of freedom into account when dealing with atom interferometers. We denote the external quantum state as $|\varphi(t)\rangle$. The phase evolution of $|\varphi(t)\rangle$ depends on the atomic motion. Here, we use the Feynman path integral approach and follow similar steps as in [48] to present the phase evolution of $|\varphi(t)\rangle$ while the atoms are moving.

For an initial quantum state $|\varphi(t_i)\rangle$ that evolves under a unitary operator U, the state becomes

$$|\varphi(t)\rangle = U(t,t_i)|\varphi(t_i)\rangle$$

t time t. The wave function becomes

$$\varphi(x,t) = \int K(x,t,x_i,t_i)\varphi(x_i,t_i)dx_i$$

where $K(x,t,x_i,t_i) = \langle x|U(t,t_i)|x_i\rangle$ is the quantum propagator. According to Feynman's expression

$$K(x,t,x_i,t_i) = \mathcal{N}\sum_{\Gamma} e^{iS_\Gamma/\hbar}$$

where $\mathcal{N}$ is a normalization constant, $\sum_\Gamma$ denotes a functional integral over the space of all possible paths Γ connecting x, t and x_i, t_i, and

$$S_\Gamma = \int_{t_i}^{t} d\tau L[x(\tau), \dot{x}(\tau)]$$

is the action along the path Γ. According to this equation, only paths that are close to the classical path are expected to contribute to the integral. For a quadratic Lagrangian, the propagator becomes

$$K(x,t,x_i,t_i) = F(t,t_i)e^{\frac{i}{\hbar}S_{cl}(x,t,x_i,t_i)}$$

where F is just a functional integral that is independent of x and x_i. Thus, the wave function becomes

$$\varphi(x,t) = F(t,t_i)\int dx_i e^{\frac{i}{\hbar}S_{cl}(x,t,x_i,t_i)}\varphi(x_i,t_i).$$

If the initial wavefunction is a plane wave (a momentum eigenstate with eigenvalue p_0), i.e.

$$\varphi(x_i,t_i) = \frac{1}{\sqrt{2\pi\hbar}}e^{i\frac{p_0x_i - E_0t_i}{\hbar}},$$

using the stationary phase method the final wavefunction becomes

$$\varphi(x,t) = F(t,t_i)\sqrt{\frac{i\pi\hbar}{C(t,t_i)}}\varphi(x_0,t_i)e^{\frac{i}{\hbar}S_{cl}(x,t,x_0,t_i)}. \tag{2.53}$$

The initial point at time t_i on the classical trajectory has momentum p_0 and position x_0, and the final position at time t has position x. x_0 is called a stationary phase point. For a particle moving in a gravitational field $L = \frac{1}{2}m\dot{x}^2 - mgx$, its action S_{cl} is

$$S_{cl}(x, t, x_i, t_i) = \frac{m}{2}\frac{(x - x_i)^2}{t - t_i} - \frac{mg}{2}(x + x_i)(t - t_i) - \frac{mg^2}{24}(t - t_i)^3. \tag{2.54}$$

We can write the phase evolution of a quantum state $|a, p\rangle$ due to propagation as

$$\phi_{propagation} = -\frac{E_a}{\hbar}t + \frac{S_{cl}}{\hbar}. \tag{2.55}$$

The internal degree of freedom of $|a, p\rangle$ is described by state $|a\rangle$, an eigenstate of its internal Hamiltonian. The external degree of freedom of $|a, p\rangle$ is described by state $|p\rangle$, a momentum eigenstate.

2.9.2 Phase due to lasers

In our experiment, we use Raman transitions to manipulate the quantum state of the atoms. The interaction between atoms and the Raman lasers introduces phase shifts to the atoms. The solution to Equation 2.24 shows that the Raman transition is equivalent to a 2-level system interacting with a single mode electromagnetic field. Thus, we can use Equation 2.8 to analyze the phase shifts due to Raman lasers with the corresponding Rabi frequency and detuning. Also here $\phi = \phi_1 - \phi_2$ is the phase difference between two Raman lasers. Here, we assume the laser beams are plane waves whose magnitude and k vector are constant over the space.

Considering the on resonance case, Equation 2.8 becomes:

$$\begin{pmatrix} \psi_a(t) \\ \psi_b(t) \end{pmatrix} = \begin{pmatrix} \cos\frac{\Omega t}{2} & -i\sin\frac{\Omega t}{2}e^{i\phi} \\ -i\sin\frac{\Omega t}{2}e^{-i\phi} & \cos\frac{\Omega t}{2} \end{pmatrix} \begin{pmatrix} \psi_a(0) \\ \psi_b(0) \end{pmatrix}. \tag{2.56}$$

For a $\pi/2$ pulse, i.e. $\Omega t = \pi/2$, the equation becomes:

$$\begin{pmatrix} \psi_a(t) \\ \psi_b(t) \end{pmatrix} = \begin{pmatrix} \frac{1}{\sqrt{2}} & -\frac{i}{\sqrt{2}}e^{i\phi} \\ -\frac{i}{\sqrt{2}}e^{-i\phi} & \frac{1}{\sqrt{2}} \end{pmatrix} \begin{pmatrix} \psi_a(0) \\ \psi_b(0) \end{pmatrix}. \tag{2.57}$$

For a π pulse, i.e. $\Omega t = \pi$, the equation becomes:

$$\begin{pmatrix} \psi_a(t) \\ \psi_b(t) \end{pmatrix} = \begin{pmatrix} 0 & -ie^{i\phi} \\ -ie^{-i\phi} & 0 \end{pmatrix} \begin{pmatrix} \psi_a(0) \\ \psi_b(0) \end{pmatrix}. \tag{2.58}$$

Based on this result, we summarize the change in state coefficients due to the laser beams:

$$\begin{aligned} |a\rangle &\to -ie^{-i\phi}\,|b\rangle \\ |b\rangle &\to -ie^{i\phi}\,|a\rangle\,. \end{aligned} \tag{2.59}$$

The changes in state coefficients reflect the laser imprinted phases. An atom changes its state from $|a\rangle$ to $|b\rangle$ by absorbing a photon with momentum $\hbar\vec{k_1}$ and emitting another photon with momentum $\hbar\vec{k_2}$ where $\vec{k_1}$ and $\vec{k_2}$ are the wave vectors of the two Raman laser beams. Thus, the momentum state changes from $|p\rangle$ to $|p+\hbar(\vec{k_1}-\vec{k_2})\rangle$. In the meantime, the state changes its coefficient by $-ie^{-i\phi}$. When the atom changes its state from $|b\rangle$ to $|a\rangle$, it absorb a photon with momentum $\hbar\vec{k_2}$ and emits another photon with momentum $\hbar\vec{k_1}$. Thus, the momentum state changes from $|p\rangle$ to $|p+\hbar(\vec{k_2}-\vec{k_1})\rangle$. The state changes its coefficient by $-ie^{i\phi}$. Raman lasers couple the atomic external and internal degrees of freedom and also imprint phase shifts to the atomic state.

2.9.3 Atom interferometer phase

The atom interferometer phase is the phase difference along two different paths. The difference in phase is due to propagations, lasers, and separation between the two paths at the output port, i.e. $\Delta\phi = \Delta\phi_{propagation} + \Delta\phi_{lasers} + \Delta\phi_{separation}$. $\Delta\phi_{propagation}$ and $\Delta\phi_{lasers}$ can be calculated using the results from previous sections. $\Delta\phi_{separation} = \frac{1}{\hbar}\bar{p}\Delta x$ where $\bar{p}$ is the average canonical momentum of the two paths and Δx is the separation between the centers of the two paths in a given output port [51].

2.9.4 Mach-Zehnder atom interferometer

As an example, we calculate the phase of a Mach-Zehnder atom interferometer as shown in Figure 2.11. The Mach-Zehnder atom interferometer consists of a π and two $\pi/2$ pulses. Each pulse is separated by time T. We call T the interrogation time. We calculate the phase difference between path ACB and ADB and observe the interference at output port 1. Assume the two laser beams that drive the Raman transition are counter-propagating and have wave vector k_1 and $-k_2$, thus the momentum kick on the atoms are $\hbar(k_1+k_2)$ and the laser phase at position x is $(k_1+k_2)x+\phi_0$ where ϕ_0 is a constant.

We first calculate propagation phase using the conclusion from subsection 2.9.1:

$$\begin{aligned}\Delta\phi_{propagation} &= -\frac{E_a}{\hbar}T + \frac{S_{cl}^{CA}}{\hbar} - \frac{E_b}{\hbar}T + \frac{S_{cl}^{BC}}{\hbar} - (-\frac{E_b}{\hbar}T + \frac{S_{cl}^{DA}}{\hbar} - \frac{E_a}{\hbar}T + \frac{S_{cl}^{BD}}{\hbar}) \\ &= \frac{S_{cl}^{DA} + S_{cl}^{BD} - (S_{cl}^{CA} + S_{cl}^{BC})}{\hbar}\end{aligned} \tag{2.60}$$

$$S_{cl}^{DA} - S_{cl}^{CA} = \frac{m}{2T}[(x_D + x_C - 2x_A)(x_D - x_C)] + \frac{mg}{2}(x_C - x_D)T \tag{2.61}$$

$$S_{cl}^{BD} - S_{cl}^{BC} = \frac{m}{2T}[(2x_B - x_C - x_D)(x_C - x_D)] + \frac{mg}{2}(x_C - x_D)T \tag{2.62}$$

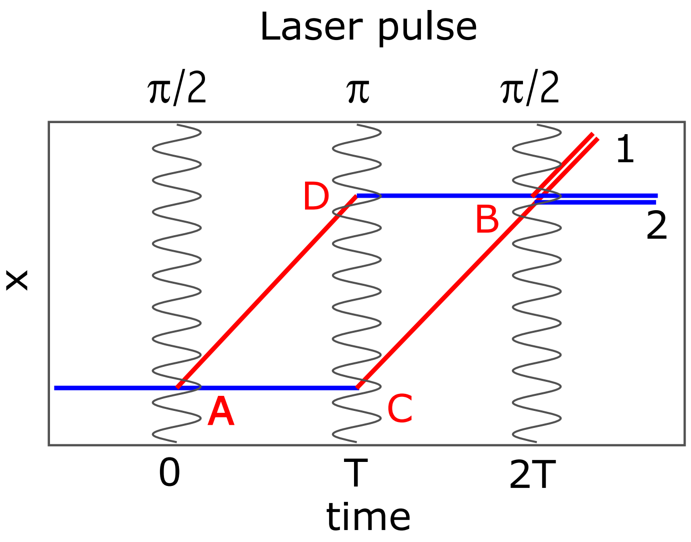

Figure 2.11: Space-time diagram for a Mach-Zehnder interferometer. This interferometer has a laser pulse sequence with $\pi/2 - \pi - \pi/2$ pulses. Each pulse is separated by time T. The laser pulses are formed by counter-propagating beams. Blue solid lines stand for the paths of state $|a, p\rangle$. Red solid lines stand for the paths of state $|b, p + \hbar(k_1 + k_2)\rangle$. The paths are represented in the frame of free-falling atoms.

$$\begin{aligned} x_C &= x_A + v_0 T - \frac{1}{2} g T^2 \\ x_D &= x_A + (v_0 + v)T - \frac{1}{2} g T^2 \\ x_B &= x_D + (v_0 - gT)T - \frac{1}{2} g T^2 \end{aligned} \tag{2.63}$$

where $v = \hbar(k_1 + k_2)/m$ is the velocity change due to the momentum kick and v_0 is the initial velocity. Thus,

$$S_{cl}^{DA} + S_{cl}^{BD} - (S_{cl}^{CA} + S_{cl}^{BC}) = 0. \tag{2.64}$$

Thus,

$$\Delta\phi_{propagation} = 0. \tag{2.65}$$

We next calculate the laser phase using the conclusion from subsection 2.9.2. For path ACB and output port 1, the first $\pi/2$ pulse imprints no phase. The π pulse changes the state from $|a, p\rangle$ to $|b, p + \hbar(k_1 + k_2)\rangle$, so it changes the state coefficient by $-ie^{-i\phi_C}$. The last $\pi/2$ pulse imprints no phase since the state remains the same. The total change in state coefficient for this path is thus $-ie^{-i\phi_C}$. For path ADB and output port 1, the first $\pi/2$ pulse changes the state coefficient by $-ie^{-i\phi_A}$. The π pulse changes the state coefficient by $-ie^{i\phi_D}$. The last $\pi/2$ pulse changes the state coefficient by $-ie^{-i\phi_B}$. Thus, the total change in state coefficient for this path is

$(-ie^{-i\phi_A})(-ie^{i\phi_D})(-ie^{-i\phi_B}) = ie^{i(-\phi_A+\phi_D-\phi_B)}$. The laser phase difference between path ADB and ACB is $\Delta\phi_{laser} = -\phi_A + \phi_D - \phi_B - (-\phi_C)$. Based on the phase equation:

$$\begin{aligned} \phi_A &= (k_1 + k_2)x_A + \phi_A^{(0)} \\ \phi_D &= (k_1 + k_2)x_D + \phi_D^{(0)} \\ \phi_B &= (k_1 + k_2)x_B + \phi_B^{(0)} \\ \phi_C &= (k_1 + k_2)x_C + \phi_D^{(0)}, \end{aligned} \tag{2.66}$$

the laser phase difference

$$\begin{aligned} \Delta\phi_{laser} &= (k_1 + k_2)(x_C + x_D - x_B - x_A) + 2\phi_D^{(0)} - \phi_A^{(0)} - \phi_B^{(0)} \\ &= (k_1 + k_2)gT^2 + 2\phi_D^{(0)} - \phi_A^{(0)} - \phi_B^{(0)}. \end{aligned} \tag{2.67}$$

Since the two atomic clouds (paths) overlap at the output port, $\Delta\phi_{separation} = 0$. The atom interferometer phase is thus $\Delta\phi = \Delta\phi_{laser} = (k_1 + k_2)gT^2 + 2\phi_D^{(0)} - \phi_A^{(0)} - \phi_B^{(0)}$.

The state of the output port 1 is a result of the interference between path ADB and path ACB. Only considering the laser effects, the state can be written as

$$\mathcal{N}'(-ie^{-i\phi_C} |b, p + \hbar(k_1 + k_2)\rangle + ie^{i(-\phi_A+\phi_D-\phi_B)} |b, p + \hbar(k_1 + k_2)\rangle) \tag{2.68}$$

where $\mathcal{N}'$ is a normalization coefficient. Now considering the total atom interferometer phase $\Delta\phi$, the state of the output port 1 is written as

$$\mathcal{N}(1 - e^{i\Delta\phi}) |b, p + h(k_1 + k_2)\rangle \tag{2.69}$$

where $\mathcal{N}$ is a normalization coefficient to ensure that the maximum probability of state $|b, p + h(k_1 + k_2)\rangle$ is 1. The probability of state $|b, p + h(k_1 + k_2)\rangle$ is then

$$P_b = |\mathcal{N}|^2(1 - e^{i\Delta\phi})(1 - e^{-i\Delta\phi}) = |\mathcal{N}|^2(2 - 2cos\Delta\phi). \tag{2.70}$$

Thus $|\mathcal{N}|^2 = 1/4$, $P_b = (1 - cos\Delta\phi)/2$. In reality, due to the inefficiency of the laser pulses, not all the atoms are transferred. This reduces the constrast of the interferometer, i.e. $P_b = (1 - C \cdot cos\Delta\phi)/2$ where $0 \leq C \leq 1$. Similarly the probability of state $|a, p\rangle$ at output port 2 is $P_a = (1 + C \cdot cos\Delta\phi)/2$. Thus, the normalized population difference between state $|a, p\rangle$ and $|b, p + h(k_1 + k_2)\rangle$ is $P = C \cdot cos\Delta\phi$. Since $P = 2J_z/N$ where N is the number of atoms, we have

$$\frac{\Delta J_z}{N} = \frac{1}{2}C \cdot \Delta(\Delta\phi), \quad \Delta\phi = \frac{\pi}{2}. \tag{2.71}$$

This equation tells us that reducing the J_z uncertainty improves the phase resolution. Spin squeezing will benefit the resolution of atom interferometers. This equation also tells us that ΔJ_z and the contrast C are two important parameters that characterize the atom interferometer performance. We should minimize ΔJ_z while maximize C.

Chapter 3

Apparatus and Sequence

This chapter gives an overview of the experimental setup and sequence that enable 20dB squeezing with atoms trapped inside an optical lattice. The infrastructure was constructed by the previous members in the Kasevich group. A more detailed description can be found in [52, 44, 53, 54]. The additions to the setup and adaptations to the sequence to suit the free space applications are going to be briefly mentioned but will be elaborated in later chapters.

3.1 Vacuum chamber

The vacuum chamber of this experiment is made of Zerodur glass. This glass has a very low thermal expansion coefficient. The low thermal expansion minimizes thermal drifts of the optical cavity length. Zerodur glass also has very good transmission for wavelength at 780nm. However, this glass shows birefringent under pressure that changes the polarization of the incident light.

The vacuum chamber consists of a Rb reservoir, a 2D MOT chamber, a 3D MOT chamber with cavity tubes, and a glass-to-metal indium seal leading to an ion pump. The ion pump maintains the vacuum with a pressure below 10^{-8}mbar.

3.2 Timing sequence

The experiment is run in continuous cycles. Every cycle consists a sequence of signals that control the lasers, magnetic fields, microwaves, data-taking instruments and etc. The control signals are managed by a digital signal processor (DSP). During one cycle, the atoms are cooled, squeezed, and used for sensor applications. Each cycle takes 1s to complete, constituting a single squeezing event of about 1ms and a sensing event of about 4ms.

3.3 Cold atom source

3.3.1 Atom cooling and trapping

The ^{87}Rb atoms for the experiment comes from heating the Rb reservoir. After escaping the reservoir, the Rb atoms are directed by a 2D magneto-optical trap (MOT) to a 3D MOT. The atom cooling starts with this 3D MOT and then goes on for a few far-detuned MOT stages with increasingly larger detunings. After MOT stages, the atoms are further cooled by molasses. While cooling, the atoms are loaded into an optical lattice formed by a cavity mode. The 3D MOT is formed close to the beam waist of the cavity mode to maximize the number of atoms loaded into the optical lattice. The cooling and trapping stages are optimized together, resulting in $\sim 25\mu$K atoms trapped in a $\sim 500\mu$K-deep optical lattice. The atom cloud includes $\sim 500,000$ atoms and takes about 1000 lattice sites. This is ~ 1.5mm long longitudinally (along the cavity axis) and $\sim 17\mu$m rms radius transversely. The cooling process takes 70% of the cycle time.

In contrast to other laser cooling experiments, our experiment includes an optical cavity, which complicates the process. As demonstrated in [55], the optical cavity together with the MOT laser beams form a Raman laser system. This lasing phenomenon heats up the atoms and makes the cooling process cavity length dependent. Since our experiment requires the cavity maintaining a specific length, special care needs to be taken when choosing cooling parameters. This cavity effect also affects the atom interferometer contrast as will be detailed in subsection 6.3.2.

3.3.2 State preparation

In our experiment, we utilize the two magnetically insensitive hyperfine ground states ($|F = 1, m_F = 0\rangle$ and $|F = 2, m_F = 0\rangle$) of ^{87}Rb atoms for squeezing and sensing. It is important to prepare the atoms in these two states with high fidelity. However, the atoms occupy different magnetic sensitive states after cooling, we thus run a sequence of repump and depump stages combined with microwave transitions to prepare greater than 99% of the atoms in $|F = 1, m_F = 0\rangle$ state before the squeezing sequence, leaving the effects on squeezing due to atoms from other magnetic sublevels negligible.

3.4 Dual-wavelength optical cavity

The optical cavity we use in our experiment is near confocal and symmetric. This cavity is also dual-wavelength that supports both a 780nm and a 1560nm mode with high finesse. The high finesse ensures that the light passes through the atoms tens of thousands of times. This increases the optical depth for the atom-light interactions, allowing the generation of highly spin squeezed state. The 780nm mode is used as the probe for the cavity J_z measurement and the 1560nm mode forms the

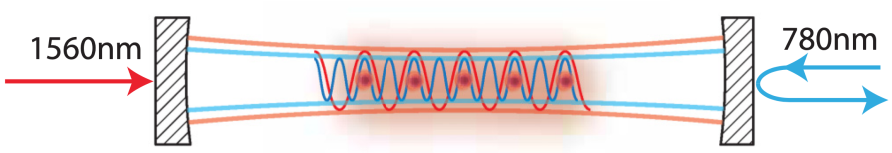

Figure 3.1: The commensurate configuration for the 1560nm optical lattice and 780nm probe light. The atoms are trapped at the maximum of the probe light in this configuration.

Parameters	780nm mode	1560nm mode
Mirror radius R	9.9cm	
Cavity length L	10.7cm	
Free spectral range ν_{fsr}	1.4GHz	
Finesse $\mathcal{F}$	175,000	117,000
Mode waist ω_0	111μm	157μm
Cavity FWHM linewidth κ	$2\pi \times 7.98$kHz	$2\pi \times 11.96$kHz
Maximum atom-cavity coupling strength g_0	$2\pi \times 142$kHz	
Single atom cooperativity $C = 4g_0^2/(\kappa\Gamma)$	1.68	

Table 3.1: List of cavity parameters. The values are taken from [44, 56]. The values of the cooperativity C and maximum atom-cavity coupling g_0 are calculated from cavity parameters. The atom distribution is not considered in deriving these values.

optical lattice for trapping. As the 1560nm is exactly twice the wavelength of 780nm, there exists a commensurate configuration between the two modes. This commensurate configuration allows trapping of the atoms at the maximum of the probe light as shown in Figure 3.1. This results in almost homogeneous atom-cavity coupling and less probe-induced decoherence on the atoms. Another feature of our optical cavity is that the cavity mode is slowly diverging at the waist and has relatively large mode volume. The large mode volume allows the cavity to accommodate large number of atoms. This enables large amount of squeezing. In addition, it is important to have large atom numbers for sensor applications. The slowly diverging mode at the waist contribute to homogeneous atom-cavity coupling, since the atoms are trapped near the beam waist. The parameters of the optical cavity are shown by Table 3.1.

3.4.1 Lattice and probe frequency stabilization

Two laser beams need to be frequency stabilized to the optical cavity. One is the 1560nm lattice beam. The other is the 780nm probe beam. The generation of the two beams is shown in Figure 3.2. The 1560nm lattice light is generated from a RIO Orion module, a low noise external cavity laser. This laser is locked to a scrubbing cavity through standard Pound–Drever–Hall (PDH) technique [57]. For this PDH, the slow feedback is the RIO laser current and the fast feedback is the fiber electro-optical modulator (EOM). This cavity filters out high frequency optical noise from the external

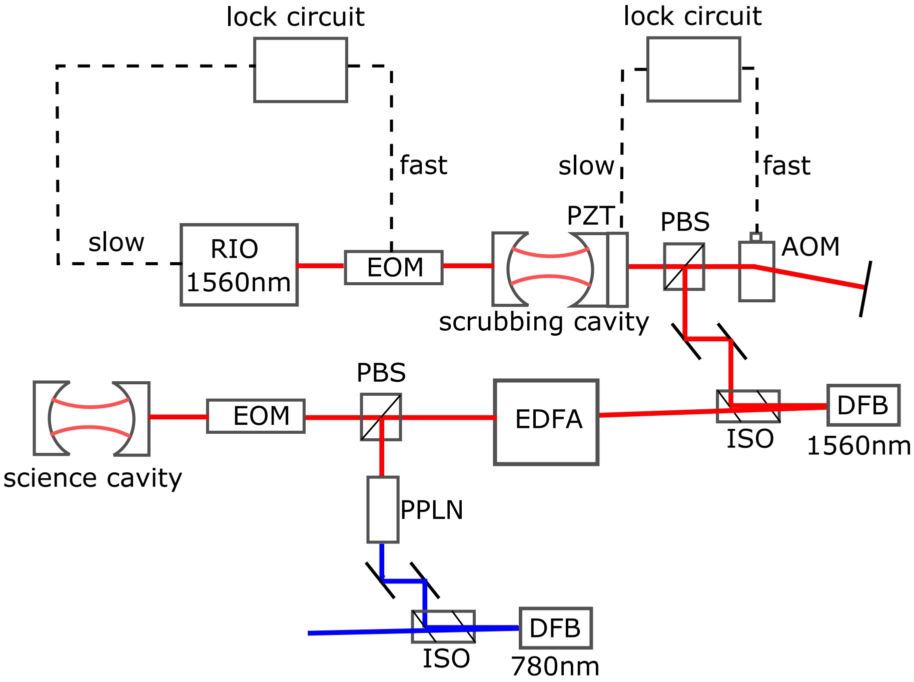

Figure 3.2: Lattice and probe laser frequency stabilization diagram. Red lines: 1560nm light. Blue lines: 780nm light. Dashed lines: electric feedback signals. Fast: fast feedback. Slow: slow feedback. RIO 1560nm: RIO Orion module external cavity laser. EOM: electro-optic phase modulator. PZT: piezo. PBS: polarized beam splitter. AOM: acousto-optic modulator. ISO: Faraday isolator. DFB: distributed feedback laser. EDFA: erbium-doped fiber amplifier. PPLN: periodically poled lithium niobate waveguide for frequency doubling.

cavity laser. The filtered light is double passed through an acousto-optic modulator (AOM) and then injected to a 1560nm diode laser. The diode laser is injection locked and serves as the seed for a fiber amplifier. The amplified light is split into two parts. One part is phase modulated and sent to the science cavity ($\sim$ 70mW). The generated first order sideband is then locked to the science cavity through a modified PDH whose fast feedback is the AOM before the injected 1560nm laser and slow feedback is the scrubbing cavity length that is controlled by a piezo. The other part ($\sim$ 200mW) is sent to a PPLN waveguide. This waveguide generates $\sim 100\mu$W 780nm light from the 1560nm input via second harmonic generation (SHG). After fiber coupling, $\sim$ 50% of the 780nm light is used to inject a probe laser. Thus, the 780nm probe light is from frequency doubled 1560nm carrier light. Since the 1560nm light is stabilized through PDH technique, the 780nm light is also stabilized. However, the 780nm probe is not automatically on resonance with the cavity. Its resonance is adjusted by the phase modulation frequency on the light that is sent to the science cavity.

3.4.2 Lattice intensity stabilization

The lattice frequency is stabilized to the science cavity. Its intensity is also stabilized via a feedback circuit. The lattice transmission intensity is measured and compared to the set points. The feedback is through the amplitude of the RF signal that modulates the 1560nm light sent to the science cavity.

3.4.3 Cavity length stabilization

The QND measurement requires the probe to be detuned right between the two hyperfine ground states. The detuning is measured by beating the probe light with the cooling light. Since the probe is locked on resonance with the cavity, this detuning is determined by the cavity length. In our experiment, we lock the cavity length to the atomic transition through a digital feedback on the heating of the cavity mirrors. The cavity mirrors expand due to heating, thus, changes the cavity length. In our experiment, this cavity length is stabilized such that the detuning between the probe and atomic transition varies within ±3MHz. The probe detuing is 3.417GHz. However, the beatnote between the probe light and the cooling light is 2.71GHz due to the AC stark shift on the atomic states caused by the optical lattice and frequency shifts on the light due to the AOMs.

3.5 Squeezing sequence

Figure 3.3 shows the sequence to generate spin squeezing. The atoms are initially prepared in $|F = 1, m_F = 0\rangle$ state. Then a microwave composite $\pi/2$ pulse (see subsection 3.5.1) is applied to the atoms to prepare a coherent spin state on the equator of the Bloch sphere. This microwave pulse is followed by presqueezing (see subsection 3.5.2). After presqueezing, two probes are applied back-to-back for the QND J_z measurement. ϕ_1 and ϕ_2 stand for the AC stark shifts on the atomic states induced by the probes. They characterize the probe strength. The atoms are trapped inside the optical lattice during the microwave and probe sequence until released for fluorescence imaging at the very end.

3.5.1 Microwave composite $\pi/2$ pulse

A microwave composite $\pi/2$ pulse is used to prepare the atoms on the equator of the Bloch sphere. In this composite $\pi/2$ pulse, a $\pi/2$ pulse first brings the $|F = 1, m_F = 0\rangle$ state (pointing to the south pole of the Bloch sphere) to the equator. Then, a π pulse 120° phase-shifted from the first $\pi/2$ pulse rotates the state back to the equator. The pulses are shown in Figure 3.4. This is designed to reduce the amplitude noise from the microwave source. For example, if the power of the first $\pi/2$ pulse is a little bit too high, it will bring the state slightly above the equator. The power of the

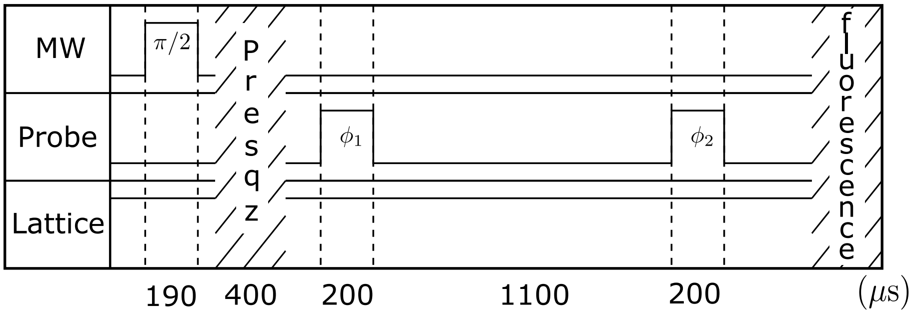

Figure 3.3: Squeezing sequence. The atoms are first prepared from the bottom to the equator of the Bloch sphere by a composite microwave $\pi/2$ pulse. Then a presqueezing procedure is applied. After that, two probe pulses are applied back-to-back for spin squeezing. ϕ_1 and ϕ_2 stand for the probe induced atomic phase shift and characterize the probe power. Finally, fluorescence imaging is applied to count the atom number. Atoms are trapped by the optical lattice until released for fluorescence imaging.

second π pulse will also be slightly higher. This compensates the effect from the first $\pi/2$ pulse and rotates the state back on the equator.

3.5.2 Presqueezing

When using large atom numbers, the QPL easily saturates the linear region of the cavity response. The saturation reduces the probe light that enters into the cavity (further away from resonance), reducing the amount of generated squeezing. Therefore, those cases need to be discarded. To increase the efficiency in squeezing generation, we apply a one-axis twisting procedure to reduce the spin noise before the QND measurement. A weak $\pi/8$ probe $6.25\kappa_0 \approx 50$KHz detuned from the cavity resonance is used to generate the one-axis twisting interaction. This interaction is followed by a $\pi/12$ microwave rotation around the center of the state to minimize spin noise. We call the one-axis twisting procedure presqueezing.

3.6 Free space application

We generate spin squeezed state with trapped atoms. To implement spin squeezing in sensors with freely moving atoms, devoid of perturbations due to an external confining potential, we release the atoms into free space. The lattice is turned off after the first probe measurement. Depending on our retrieval methods, the lattice will or will not be turned back on after release.

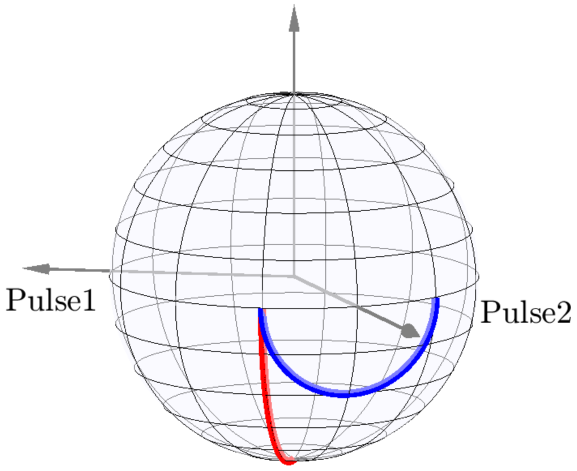

Figure 3.4: Composite microwave $\pi/2$ pulse. Pulse1 is a microwave $\pi/2$ pulse (red solid line) that brings the state from the bottom of the Bloch sphere (all $|\downarrow\rangle$ states) to the equator. Pulse2 is a microwave π pulse (blue solid line) whose phase is 120° away from Pulse1. This pulse brings the state closer to the equator.

Lattice ramp down time	v_{rms}	T	$\Delta\omega$
0.2ms	0.055m/s	32μK	$2\pi \cdot 141$KHz
7ms	0.032m/s	11μK	$2\pi \cdot 82$KHz

Table 3.2: Atomic temperature after release. The atomic rms velocity (v_{rms}) for short (0.2ms) and long (7ms) lattice ramp down time are measured by time-of-flight experiments. The temperature T is calculated by $T = mv_{rms}^2/k_B$. The Doppler width $\Delta\omega$ is calculated by $\Delta\omega = 2k\Delta v$.

3.6.1 Atomic temperature after release

We release the atoms into free space by turning off the optical lattice. We use two schemes. One is to turn off the lattice quickly in 0.2ms, and the other is to turn off the lattice relatively slowly in 7ms (compared to the lattice trapping period of 1.1ms in the transverse direction). Turning off the lattice in 7ms reduces atomic heating, because this process is close to adiabatic. We measure the atomic temperature after release using time-of-flight measurement. The temperature is calculated by

$$\frac{1}{2}k_B T = \frac{1}{2}mv_{rms}^2 \tag{3.1}$$

where k_B is the Boltzmann constant, v_{rms} is the rms velocity measured from time-of-flight measurement, and m is the mass of a ^{87}Rb atom. The Doppler width $\Delta\omega$ is calculated via

$$\Delta\omega = 2k\Delta v \tag{3.2}$$

where $\Delta v = v_{rms}$ is the velocity spread of the atoms and k is the wave vector of a single Raman beam. For Doppler sensitive Raman transition (counter-propagating beams), each laser contributes to the Doppler shift in the opposite direction. Thus, we need to use $2k$ for the Doppler shift calculation. The result of atomic temperature measurement is shown in Table 3.2.

3.6.2 Homogenous atom-cavity coupling

The success of spin squeezing retrieval from free space requires that the initial squeezed states are prepared in a spatially homogeneous way, i.e. that each atomic spin must contribute equally to the collective spin that is being measured. Otherwise, the retrieval of squeezing is hindered: once the atoms are free to move, the information about their individual contributions to the original collective spin is lost, and a different collective spin, which is not necessarily squeezed, is probed. In [24, 58], the homogeneity requirement in cavity-generated spin squeezing experiments has been realized.

In our experiment, the optical cavity apparatus is specifically designed to enforce homogeneous atom-cavity coupling as described in section 3.4. We use a cavity and a camera method to retrieve free space squeezing.

3.7 Magnetic field

Our experiment does not have magnetic field shielding. Instead, we use three bias magnetic field coils to cancel the Earth magnetic field and other stray magnetic fields (such as those due to MOT coils). They also provide the required bias fields for squeezing and sensing. Besides bias magnetic field coils, our magnetic field control includes a pair of anti-Helmholtz coils for 3D MOT and two pairs of anti-Helmholtz coils for 2D MOT.

During the cooling and loading processes, the bias magnetic field is set to be close to 0 at the atoms. After the processes, the magnetic field is turned up. For free space Ramsey spectroscopy, the bias magnetic fields are turned up to 600mG and are aligned to the microwave magnetic field. The alignment is found by maximizing the Rabi frequency. When aligned, the Rabi frequency depends on the direction of the magnetic field quadratically. Thus, it is less sensitive to the fluctuations of the magnetic field direction, reducing the noise in Ramsey spectroscopy. For atom interferometery, the magnetic fields are aligned to the Raman beams. This is adjusted by minimizing undesired transitions. The details are described in subsection 6.1.3. The bias magnetic fields are changed again during fluorescence imaging to give a Gaussian cloud shape. It takes tens of milliseconds for the bias magnetic field to stabilize after switching the coil currents.

3.8 Atom number calibration

In our work, a single spin flip between the $|\uparrow\rangle$ and $|\downarrow\rangle$ states results in a ~ 5.6Hz shift in the cavity resonance frequency, as determined from our cavity parameters and independently verified by measuring the quantum projection noise for coherent spin states [24]. The atom number is measured by preparing the atoms all at $|\downarrow\rangle$ state and measure the total cavity frequency shift, because in this case, the total cavity frequency shift is proportional to the total atom number with the constant of proportionality 2.8Hz/atom. While the total atom number is determined, we take a fluorescence image of the atoms. Thus, we can calibrate for the average fluorescence photon number collected from each atom. Using this calibration, we can infer the atom number from the fluorescence image of the atoms taken by a camera.

3.9 Homodyne path length stabilization

In subsection 2.6.3, I introduce the principle of the homodyne method. In this section, I will introduce a practical problem in implementing the method. In theory, the phase fluctuations between the local oscillator (LO) and the reflected probe is only due to the atom-light interaction. However, in reality, the phase fluctuations also come from path length fluctuations. In order to measure the phase fluctuations purely from the atom-light interaction, we have to stabilize the path length between the LO and the reflected probe. This is done by sending two sidebands 2MHz away from the probe to the cavity. This is a heterodyne scheme. The reflected sidebands then mix with the local oscillator and generate an error signal. The error signal is fed back on the probe frequency.

Chapter 4

Cavity retrieved free space spin squeezing and effects of homogeneity loss

In this chapter, we demonstrate that releasing atoms into free space from an optical lattice does not deteriorate cavity generated spin squeezing for metrological purposes. We use a cavity method to retrieve squeezing from free space. An ensemble of $500,000$ spin squeezed atoms in a high-finesse optical cavity with near-homogeneous atom-cavity coupling is prepared, released into free space, recaptured in the cavity, and probed. We show that up to ~ 10dB of metrologically relevant squeezing is retrieved for 700μs release times, and decaying levels of squeezing are measured for up to 3ms release times.

In this work, both the preparation and detection of squeezing are implemented by an optical cavity mode that interacts with the atoms. However, the atom distribution changes between preparation and detection. Therefore, the atom-cavity coupling changes. The detection probe is less homogeneous than the preparation probe. This results in the degradation of squeezing. Researchers have studied models that explores atom-cavity coupling inhomogeneity where the coupling inhomogeneity stays the same between the two measurements (preparation and detection). In our case, we quantitatively assess the impact of changes in coupling homogeneity between the squeezing and retrieval operations. A theoretical model is developed to quantify this degradation and this model is experimentally validated.

Inhomogeneous coupling is a general experiment condition and the change in coupling among different measurements is unavoidable in free-space applications. Even though our experiment studies this change by a detection scheme that uses a cavity mode, this study applies to other detection schemes such as fluorescence and absorption imaging. We apply this model to estimate the effects of homogeneity loss in fluorescence imaging at the end of this chapter.

Most of this chapter is adapted from [59].

4.1 Theory

4.1.1 Modeling the loss in atom-cavity coupling homogeneity

We use $J_{z,0}$ and N_0 to stand for collective J_z and atom number measured by the homogeneous preparation probe. When atoms are identically prepared and uncorrelated, $\langle J_{z,0}^{\max}\rangle = N_0/2$ and $\mathrm{var}(J_{z,0}) = N_0/4$. Following the formalism described in [60], we introduce effective observable $J_{z,r}$ and effective atom number N_r to model the quantities measured by the inhomogeneous readout probe so that the standard relations for uncorrelated particles $\langle J_{z,r}^{\max}\rangle = N_r/2$ and $\mathrm{var}(J_{z,r}) = N_r/4$ are satisfied. Here, $J_{z,r}^{\max}$ is shorthand for $J_{z,r}$ when the quantum state gives $j_z^{(i)} = 1/2$ for all the atoms. This state is represented by the Bloch vector that is pointing to the north pole of the Bloch sphere. Accordingly, we write $J_{z,r} = \langle\eta\rangle_e \sum_i \eta_i j_z^{(i)}/\langle\eta^2\rangle_e = N_r \sum_i \eta_i j_z^{(i)}/N_0\langle\eta\rangle_e$ and $N_r = N_0\langle\eta\rangle_e^2/\langle\eta^2\rangle_e$ where $\eta_i \in [0,1]$ is the fractional coupling of the i^{th} atom and N_0 is the actual total atom number. Here $\langle\cdot\rangle_e$ is the ensemble average of a quantity over the atoms, e.g $\langle\eta\rangle_e = \sum_i \eta_i/N_0$. Given the total cavity frequency shift $\delta_{\text{cav}} = \sum_i \delta_0\eta_i j_z^{(i)} = \delta_r J_{z,r}$, the frequency shift per spin flip seen by the readout probe can be defined as $\delta_r = \delta_0\langle\eta^2\rangle_e/\langle\eta\rangle_e$ where δ_0 is the frequency shift per spin flip seen by the preparation probe.

Now we relate the observations of $J_{z,r}$ to those of $J_{z,0}$. We rely on the fact that $\langle j_z^{(i)}\rangle$ and $\langle j_z^{(i)} j_z^{(i\neq k)}\rangle$ are independent of i and k owing to the homogeneity of the prepared states. Thus, we get

$$\langle J_{z,0}\rangle = \sum_i \langle j_z^{(i)}\rangle = N_0\langle j_z^{(i)}\rangle \tag{4.1}$$

$$\begin{aligned}\langle J_{z,0}^2\rangle &= \sum_{i,k}\langle j_z^{(i)} j_z^{(k)}\rangle \\ &= \sum_{i\neq k}\langle j_z^{(i)} j_z^{(k)}\rangle + \sum_i \langle j_z^{(i)2}\rangle \\ &= N_0(N_0-1)\langle j_z^{(i)} j_z^{(i\neq k)}\rangle + N_0\langle j_z^{(i)2}\rangle\end{aligned} \tag{4.2}$$

$$\langle J_{z,r}\rangle = \frac{\langle\eta\rangle_e}{\langle\eta^2\rangle_e}\sum_i \eta_i\langle j_z^{(i)}\rangle = \frac{N_r}{N_0}\langle J_{z,0}\rangle \tag{4.3}$$

$$\begin{aligned}\langle J_{z,r}^2\rangle &= \frac{\langle\eta\rangle_e^2}{\langle\eta^2\rangle_e^2}\sum_{i,k}\eta_i\eta_k\langle j_z^{(i)}j_z^{(k)}\rangle \\ &= \frac{N_r}{N_0}\langle J_{z,0}^2\rangle - \frac{N_r}{N_0}(1-\frac{N_r}{N_0})\langle j_z^{(i)}j_z^{(i\neq k)}\rangle N_0^2\end{aligned} \tag{4.4}$$

$$\langle J_{z,r}J_{z,0}\rangle = \frac{N_r}{N_0}\langle J_{z,0}^2\rangle. \tag{4.5}$$

Defining Bloch vector angles $\theta_0 = J_{z,0}/(N_0/2)$ and $\theta_r = J_{z,r}/(N_r/2)$ for the homogeneous and inhomogeneous probes respectively, we prove that $\langle\theta_r\rangle = \langle J_{z,r}\rangle/(N_r/2) = \langle J_{z,0}\rangle/(N_0/2) = \langle\theta_0\rangle$.

Assuming the atomic state is lying close to the equator of the Bloch sphere and each location in space contains only one atom, we obtain $\langle j_z^{(i)}\rangle = \sigma$ ($\sigma \ll 1$) and $\langle j_z^{(i)2}\rangle = 1/4 + \sigma^2$. Consequently, $\langle j_z^{(i)}j_z^{(i\neq k)}\rangle = (\xi^2-1)/4(N_0-1)+\sigma^2$, where the variance of $J_{z,0}$ with respect to the CSS noise is defined as $\mathrm{var}(J_{z,0})/(N_0/4) = \xi^2$. In addition, $\langle j_z^{(i)2}\rangle - \langle j_z^{(i)}j_z^{(i\neq k)}\rangle = [1+(1-\xi^2)/(N_0-1)]/4 \approx 1/4$, where the approximation is valid if the J_z noise is close to the CSS noise; for example for a J_z noise 20dB above CSS noise ($\xi^2 = 100$), the fractional correction is only 2×10^{-4} for 500 000 atoms. Therefore,

$$\begin{aligned}&\mathrm{var}(J_{z,r}) \\ &= \frac{N_r^2}{N_0^2}\mathrm{var}(J_{z,0}) + N_r(1-\frac{N_r}{N_0})(\langle j_z^{(i)2}\rangle - \langle j_z^{(i)}j_z^{(i\neq k)}\rangle) \\ &\approx \gamma_r^2\mathrm{var}(J_{z,0}) + (1-\gamma_r)\frac{N_r}{4}\end{aligned} \tag{4.6}$$

$$\mathrm{var}(J_{z,r}-J_{z,0}) \approx (1-\gamma_r)^2\mathrm{var}(J_{z,0}) + (1-\gamma_r)\frac{N_r}{4} \tag{4.7}$$

where $\gamma_r = N_r/N_0$ is the ratio of the effective atom number measured by the inhomogeneous readout probe to the atom number measured by the homogeneous preparation probe.

4.1.2 Beam splitter model for atom loss

The loss of atom-cavity coupling homogeneity can be understood as a form of atom loss with a probability $p = 1-\gamma_r$ of losing one atom irrespective of its internal state. The atom loss is modeled by a beam splitter as shown in this section.

The algebra of angular momentum operator and the algebra of two independent quantum oscillators are connected [61]. Assume we have two uncoupled oscillators whose annihilation and creation operators are $a_{\uparrow n}$, $a_{\uparrow n}^\dagger$, and $a_{\downarrow n}$, $a_{\downarrow n}^\dagger$ respectively. An angular momentum operator can be defined as

$$\begin{aligned} j_z^{(n)} &= \frac{1}{2}(a^\dagger_{\uparrow n} a_{\uparrow n} - a^\dagger_{\downarrow n} a_{\downarrow n}) \\ j_x^{(n)} &= \frac{1}{2}(a^\dagger_{\uparrow n} a_{\downarrow n} + a^\dagger_{\downarrow n} a_{\uparrow n}) \\ j_y^{(n)} &= \frac{1}{2i}(a^\dagger_{\uparrow n} a_{\downarrow n} - a^\dagger_{\downarrow n} a_{\uparrow n}). \end{aligned} \tag{4.8}$$

These operators satisfy the usual angular momentum commutation relations. The collective angular momentum operators and the total atom number operator are defined as

$$\begin{aligned} J_i &= \sum_n j_i^{(n)} \\ N &= \sum_n (a^\dagger_{\uparrow n} a_{\uparrow n} + a^\dagger_{\downarrow n} a_{\dagger n}). \end{aligned} \tag{4.9}$$

We model the atom loss as an atom changing from mode 'a' to mode 'b'. This process is described by the evolution of the annihilation operators in the Heisenberg picture:

$$\begin{aligned} a_{\uparrow n} \to a'_{\uparrow n} &= (1-p)^{1/2} a_{\uparrow n} + p^{1/2} b_{\uparrow n} \\ a_{\downarrow n} \to a'_{\downarrow n} &= (1-p)^{1/2} a_{\downarrow n} + p^{1/2} b_{\downarrow n}. \end{aligned} \tag{4.10}$$

Thus, the evolution of the collective angular momentum and the number operator are

$$\begin{aligned} J_z \to J'_z = \sum_n [\frac{1-p}{2}(a^\dagger_{\uparrow n} a_{\uparrow n} - a^\dagger_{\downarrow n} a_{\downarrow n}) + \frac{\sqrt{p(1-p)}}{2}(a^\dagger_{\uparrow n} b_{\uparrow n} + b^\dagger_{\uparrow n} a_{\uparrow n} - a^\dagger_{\downarrow n} b_{\downarrow n} - b^\dagger_{\downarrow n} a_{\downarrow n}) \\ + \frac{p}{2}(b^\dagger_{\uparrow n} b_{\uparrow n} - b^\dagger_{\downarrow n} b_{\downarrow n})] \end{aligned} \tag{4.11}$$

$$\begin{aligned} N \to N' = \sum_n [(1-p)(a^\dagger_{\uparrow n} a_{\uparrow n} + a^\dagger_{\downarrow n} a_{\downarrow n}) + \sqrt{p(1-p)}(a^\dagger_{\uparrow n} b_{\uparrow n} + b^\dagger_{\uparrow n} a_{\uparrow n} + a^\dagger_{\downarrow n} b_{\downarrow n} + b^\dagger_{\downarrow n} a_{\downarrow n}) \\ + p(b^\dagger_{\uparrow n} b_{\uparrow n} + b^\dagger_{\downarrow n} b_{\downarrow n})]. \end{aligned} \tag{4.12}$$

Because the initial state $|\psi_b\rangle$ for mode 'b' is empty state, when taking expectation values for J_z and N, the terms with the annihilation operator b acting left on the ket state and the terms with the creation operator acting right on the bra state vanish. Thus, $\langle N' \rangle = (1-p)\langle N \rangle$, $\langle J'_z \rangle = (1-p)\langle J_z \rangle$, $\langle J'^2_z \rangle = (1-p)^2 \langle J_z^2 \rangle + p\langle N' \rangle/4$, and

$$\mathrm{var}(J'_z) = (1-p)^2 \mathrm{var}(J_z) + p\langle N' \rangle/4. \tag{4.13}$$

This equation matches Equation 4.6, the result of homogeneity loss.

4.1.3 Modeling Back-to-back Conditional Measurement

Since J_z is inferred from the X-quadrature of a probe field through a calibrated discriminator, we label the X-quadrature of the two probes in the back-to-back measurements as X'_p and X'_r, where p and r stand for preparation and readout respectively. Since these two field modes are uncorrelated, $\mathrm{cov}(X'_p, X'_r) = 0$. We also label the collective spin operators for the atoms during the preparation and readout measurements as $J'_{z,0}$ and $J'_{z,r}$ respectively. Since before sending probes to the atoms, there are no correlations between the spins and the fields, i.e., $\mathrm{cov}(J'_{z,r}, X'_p) = \mathrm{cov}(J'_{z,0}, X'_p) = \mathrm{cov}(J'_{z,r}, X'_r) = \mathrm{cov}(J'_{z,0}, X'_r) = 0$; after probe interactions, the quadrature operators (in the Heisenberg picture) become

$$X'_p \rightarrow X_p = D_p J'_{z,0} + X'_p \tag{4.14}$$

$$X'_r \rightarrow X_r = D_r J'_{z,r} + X'_r \tag{4.15}$$

where D_i are calibrated discriminators determined by the strength of the probes. Thus the inferred J_z values from the two probes are $J_{z,0} = X_p/D_p$ and $J_{z,r} = X_r/D_r$. The variance of the inferred J_z difference is

$$\begin{aligned} &\mathrm{var}(J_{z,0} - J_{z,r}) \\ &= \mathrm{var}(J'_{z,r} - J'_{z,0}) + \frac{1}{D_p^2}\mathrm{var}(X'_p) + \frac{1}{D_r^2}\mathrm{var}(X'_r) \\ &\approx (1-\gamma_r)\frac{N_r}{4} + (1-\gamma_r)^2\mathrm{var}(J'_{z,0}) + \sigma_{Xp}^2 + \sigma_{Xr}^2. \end{aligned} \tag{4.16}$$

Here σ_{Xp}^2 and σ_{Xr}^2 are the squares of J_z resolutions by the preparation and the readout probes respectively due to optical shot noise and spin flips. $J'_{z,r}$ and $J'_{z,0}$ are J_z observables that are defined in subsection 4.1.1 without the prime. $J_{z,r}$ and $J_{z,0}$ are inferred quantities through cavity frequency measurements. The second term is an excess noise due to changes in J_z between the two probes whose value depends on the outcome of the preparation probe which itself is random.

To eliminate this noise, we work with Bloch vector angle θ. The angles inferred from the J_z measurements are defined as $\theta_0 = J_{z,0}/(N_0/2) = 2X_p/N_0 D_p$ and $\theta_r = J_{z,r}/(N_r/2) = 2X_r/N_r D_r$

respectively. The variance of the difference between the two inferred angles is

$$\begin{aligned}
&\mathrm{var}(\theta_r-\theta_0)\\
&=\mathrm{var}(\theta'_r-\theta'_0)+\frac{1}{D_p^2N_0^2/4}\mathrm{var}(X'_p)+\frac{1}{D_r^2N_r^2/4}\mathrm{var}(X'_r)\\
&\approx\frac{1-\gamma_r}{N_r}+\sigma_p^2+\sigma_r^2\\
&=\frac{1-\gamma_r}{\gamma_r}\frac{1}{N_0}+\sigma_p^2+\sigma_r^2.
\end{aligned}\tag{4.17}$$

Here $\theta'_r = J'_{z,r}/(N_r/2)$ and $\theta'_0 = J'_{z,0}/(N_0/2)$. This equation gives the angle resolution for our setup that accounts for the noise due to changes in atom-cavity coupling between the preparation and readout probes $(1-\gamma_r)/(\gamma_r N_0)$ and noise from the initial squeezing $\sigma_p^2+\sigma_r^2$.

4.2 Experiment protocol

The cavity method uses a release-recapture protocol where a lattice turn-off period is inserted between the preparation and detection measurements in the original QND squeezing protocol (section 3.5). This protocol is shown in Figure 4.1. The trapping lattice is turned off after the first probe to release the spin-squeezed atoms into free space. The lattice switching time is 50 μs, which is adiabatic for the motion in the longitudinal trapping direction but sudden for the transverse direction. After a variable release time Δt accompanied by a ballistic expansion (∼5 cm/s from a 17 μm rms radius), the lattice is turned on again with the same switching time as the release stage to recapture the atoms back into the cavity mode, which is necessary for the cavity detection. After the recapture, the atomic cloud size and position starts oscillating in the transverse direction of the 1D lattice. We placed the detection measurement while the atomic cloud is maximally compressed during such oscillations because this placement maximizes the recovered squeezing.

The ballistic expansion of the atom cloud and acceleration due to gravity lead to an asymmetry in the atom-cavity coupling between the two probes. This asymmetry between the two probes grows with the release time due to the (fixed) Gaussian spatial profile of the cavity mode. Therefore, the readout probe measures a different observable than the preparation probe that degrades the observed squeezing. In principle one can engineer more advanced release-recapture sequences to better preserve the symmetry in the atomic cloud shape between the two probes. However, such attempts lead to marginal improvements in recovered squeezing (see subsection 4.4.3). The loss of homogeneity can be treated as an effective atom loss irrespective of the details of the coupling inhomogeneity: $N_0 \to N_r$ and $J_{z,0} \to J_{z,r}$, where subscript 0 and subscript r stand for observables seen by the near homogeneously coupled state-preparation probe and the inhomogeneously coupled readout probe, respectively. In earlier squeezed-state measurement-based metrology demonstrations,

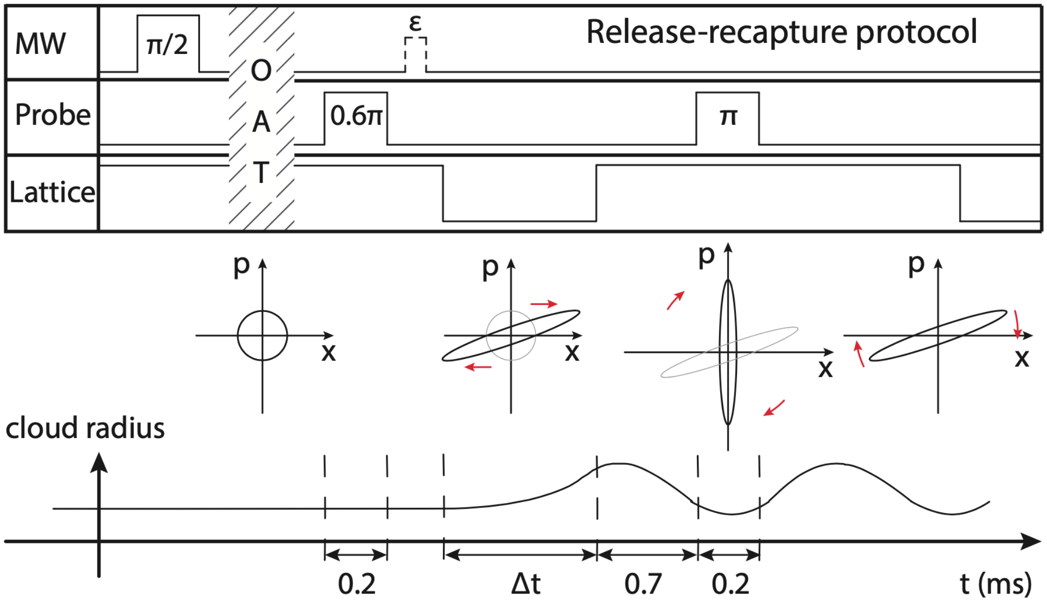

Figure 4.1: Release-recapture protocol: timing sequence (top), illustrations for phase-space evolution of the atomic cloud in the transverse direction of the cavity (middle), and rms transverse cloud size evolution (bottom). In the phase space illustration, clouds are modeled to execute harmonic oscillations when trapped in the lattice. MW: microwaves; OAT: one-axis twisting; $\pi/2$: composite microwave pulse that prepares the initial superposition state; 0.6π and π: probe power expressed in terms of the relative AC-Stark phase shifts induced between the two atomic states; Δt: free-fall time; ϵ: a small microwave rotation.

where the atom-cavity coupling did not substantially change between the state-preparation and readout probes, squeezing efficacy could be directly assessed through comparison of collective spin measurements resulting from back-to-back QND probes. In the current experiment, this approach is no longer accurate. The effective atom numbers and atom-cavity couplings result in different cavity frequency shifts in the two probes. In order to accommodate this change, we translate observed cavity shifts into Bloch vector angles: $\theta_0 = J_{z,0}/(N_0/2)$ and $\theta_r = J_{z,r}/(N_r/2)$ for the preparation and readout probes, respectively (in this experiment $J_{z,0} \ll N_0$ and $J_{z,r} \ll N_r$). While the measured cavity shifts differ, the mean values for θ_0 and θ_r preserve between the two probes (i.e., $\langle\theta_0\rangle = \langle\theta_r\rangle$).

4.3 Results

We demonstrate this equivalence experimentally by inserting an additional small microwave rotation between the preparation and readout probes (see Figure 4.1) whose phase is 90 degrees from the atomic phase in order to prepare a Bloch vector angle θ_0 away from the equator. We then compare $\langle\theta_r\rangle$ to $\langle\theta_0\rangle$ at different release times. Since θ_0, $\theta_r \ll 1$, these angles can be determined experimentally from the ratio of the observed cavity shift to the maximal shift observed when atoms are prepared in the $|\downarrow\rangle$ state. The result is shown in Figure 4.2. Linear regression to data points for all the release times with zero intercept gives a slope of 0.97 ± 0.01 (68% confidence interval), which shows that experimentally we find the angle $\langle\theta_r\rangle$ to be equal to $\langle\theta_0\rangle$ with less than 5% error. This discrepancy is from the uncertainty in the initial alignment of the microwave phase to the atomic phase. For this data, we use small atom numbers ($\sim 50,000$ atoms) so that the cavity shifts remain well within the linear response of the homodyne cavity readout.

The phase resolution $\Delta\theta$ of the squeezing protocol is determined experimentally from the measured values of θ_r and θ_0 over an ensemble of measurements. Specifically, $(\Delta\theta)^2 = \mathrm{var}(\theta_r - \theta_0)$. Figure 4.3 shows the measured resolution $\Delta\theta$ for ensembles of $N \sim 500,000$ spin-squeezed atoms (circles) as a function of release time Δt when the state is near the equator of the Bloch sphere. Each data point for $\Delta\theta$ is obtained using more than 700 independent measurements (inset Figure 4.3). The best observed angle sensitivity is 298(8) μrad. As expected, $\Delta\theta$ increases with release time since the asymmetry between the two probe couplings increases with this time. For comparison, the projection noise level associated with a coherent spin state with atom number N_0 measured by the preparation probe is also shown in Figure 4.3. $N_0 \approx N$ is determined from the observed cavity frequency shift, following [62].

Remarkably, the observed loss in phase resolution – fundamentally associated with the loss in coupling homogeneity of the readout probe – can be accurately described by a model which parameterizes this homogeneity loss in terms of a single parameter, the effective atom number N_r,

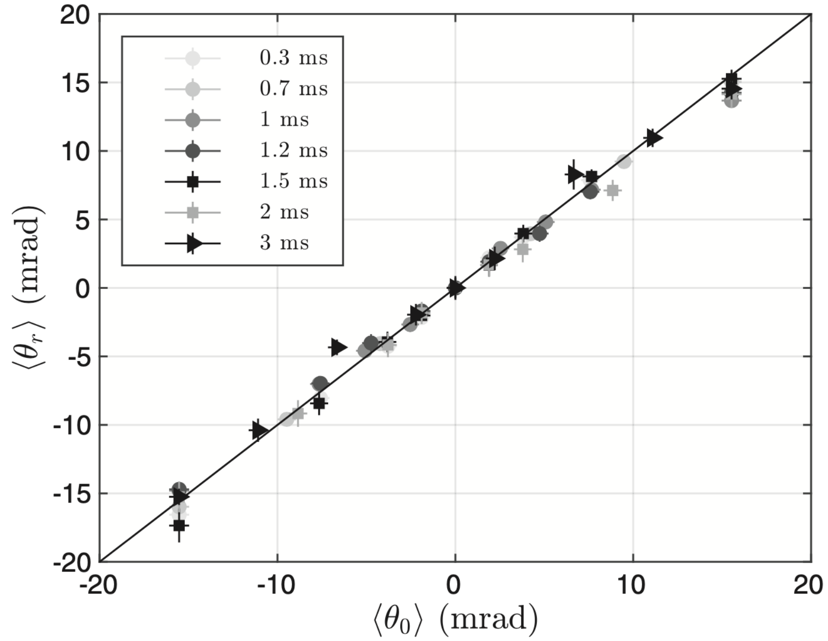

Figure 4.2: Relation between $\langle\theta_r\rangle$ and $\langle\theta_0\rangle$ for different free-fall times Δt. Black line: function $\langle\theta_r\rangle = \langle\theta_0\rangle$. Error bars stand for 68% confidence interval.

regardless of the detailed structure of the coupling. Explicitly, $N_r \equiv (\sum_{i=1}^{N} \eta_i)^2/\sum_{i=1}^{N} \eta_i^2$, where $\eta_i \in [0,1]$ is the fractional coupling of the i^{th} atom in the ensemble and N is the total atom number. From this definition, based on the derivation described in subsection 4.1.3 it is shown that

$$(\Delta\theta)^2 \simeq \frac{1-\gamma_r}{\gamma_r}\frac{1}{N_0} + \sigma_p^2 + \sigma_r^2, \tag{4.18}$$

where $\gamma_r \equiv N_r/N_0$ is the ratio of the effective atom number measured by the inhomogeneous readout probe to the atom number measured by the homogeneous preparation probe, and the terms σ_p^2 and σ_r^2 account for the photon shot noise and spin flip noise for the preparation and readout probes respectively. At longer release times, where coupling homogeneity loss plays a significant role, the σ_p and σ_r terms are dominated by the first term in Equation 4.18. In the limit of no homogeneity loss ($\gamma_r \to 1$), the expression approaches the noise of the initial spin squeezed state.

Comparison of the data shown in Figure 4.3 with Equation 4.18 requires experimental determination of γ_r. This can be done by noting that N_r is defined such that the projection noise in the corresponding effective spin component $J_{z,r}$ for an initially prepared coherent spin state is $\text{var}(J_{z,r}) = N_r/4$ while $|J_r| = N_r/2$ [31]. Combining these definitions yields $\text{var}(J_{z,r})/|J_r|^2 = 1/N_r$,

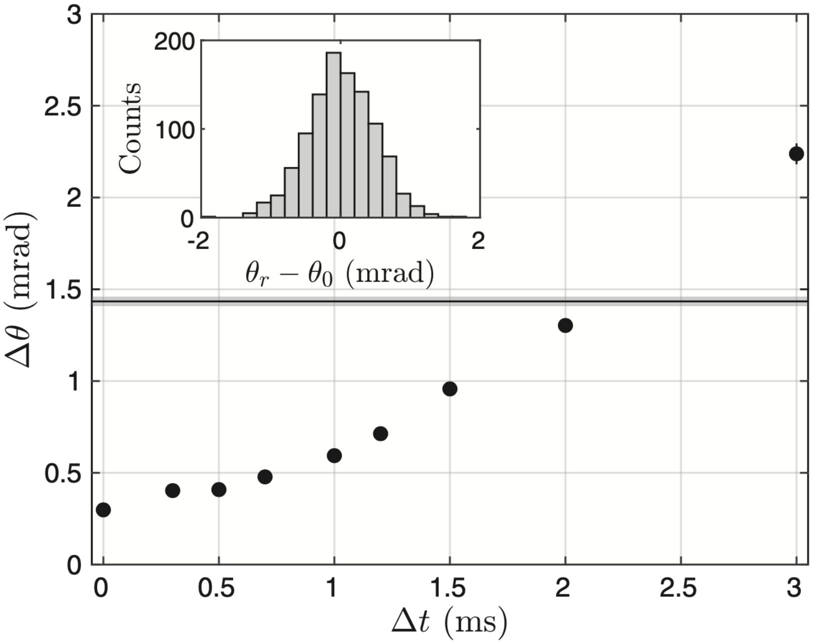

Figure 4.3: Single-shot phase sensitivity $\Delta\theta$ as a function of release time Δt. $\Delta t = 0$ indicates no release. Circles show $\Delta\theta$ for spin squeezed state. The solid line is the quantum projection noise level given by atom number N_0. The width of the shaded region is given by the uncertainty in determination of N_0 (68% confidence interval). Some of the error bars are smaller than the plotted data points. Inset: histogram of $\theta_r - \theta_0$ at $\Delta t = 0.7$ms.

which allows determination of N_r through measurement of the ratio $\mathrm{var}(J_{z,r})/|J_r|^2$ for coherent states. We experimentally determine the value of this ratio through the ratio of the observed fluctuations in the homodyne signal for a coherent spin state on the equator [proportional to $\mathrm{var}(J_{z,r})^{1/2}$] and the overall cavity shift observed when the atoms are instead prepared in the $|\downarrow\rangle$ state (proportional, with the same constant of proportionality, to $|J_r|$). Combined with an initial measurement of N_0, γ_r is thus determined. Figure 4.4(a) shows the resulting inferred values of γ_r as a function of release time. Since γ_r is independent of initial atom number, we determine γ_r with smaller ensembles of $\sim 100,000$ atoms to avoid the influence of microwave rotation noise in the preparation of the initial coherent spin state. Substitution of the measurement of γ_r, together with the known value of $\sigma_p^2 + \sigma_r^2$ and N_0, into Equation 4.18 leads to Figure 4.4(b).

Metrologically-relevant squeezing can be quantified with the Wineland parameter ξ^2 [35, 27], which compares the angle resolution $\Delta\theta$ obtained with a squeezed state to that obtained with an (unsqueezed) coherent spin state having the same number of atoms and also accounts for coherence

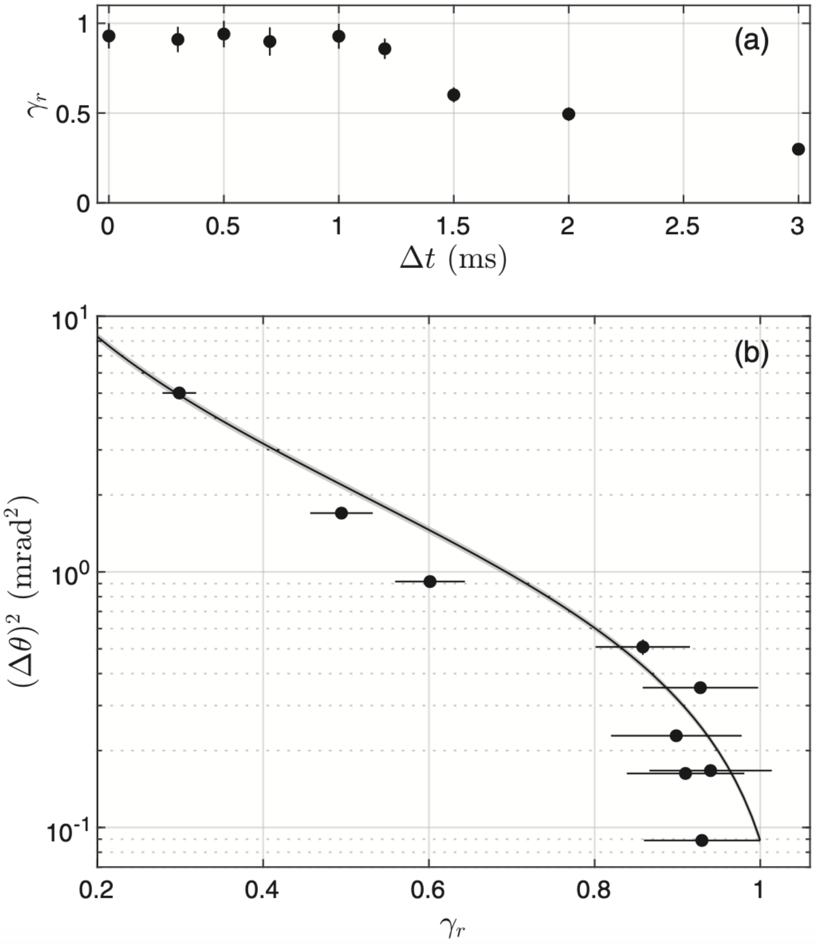

Figure 4.4: (a) Measured value of γ_r as a function of Δt. (b) $(\Delta\theta)^2$ as a function of γ_r. The solid line is a theory curve for $N_0 = 500,000$ and $\sqrt{\sigma_p^2 + \sigma_r^2} = 298\,\mu$rad using Equation 4.18. The shaded region is due to the uncertainty in determination of N_0 and $\sqrt{\sigma_p^2 + \sigma_r^2}$ (width indicates 68% confidence interval). Error bars show 68% confidence interval. Some of the error bars in y axis are smaller than the plotted points.

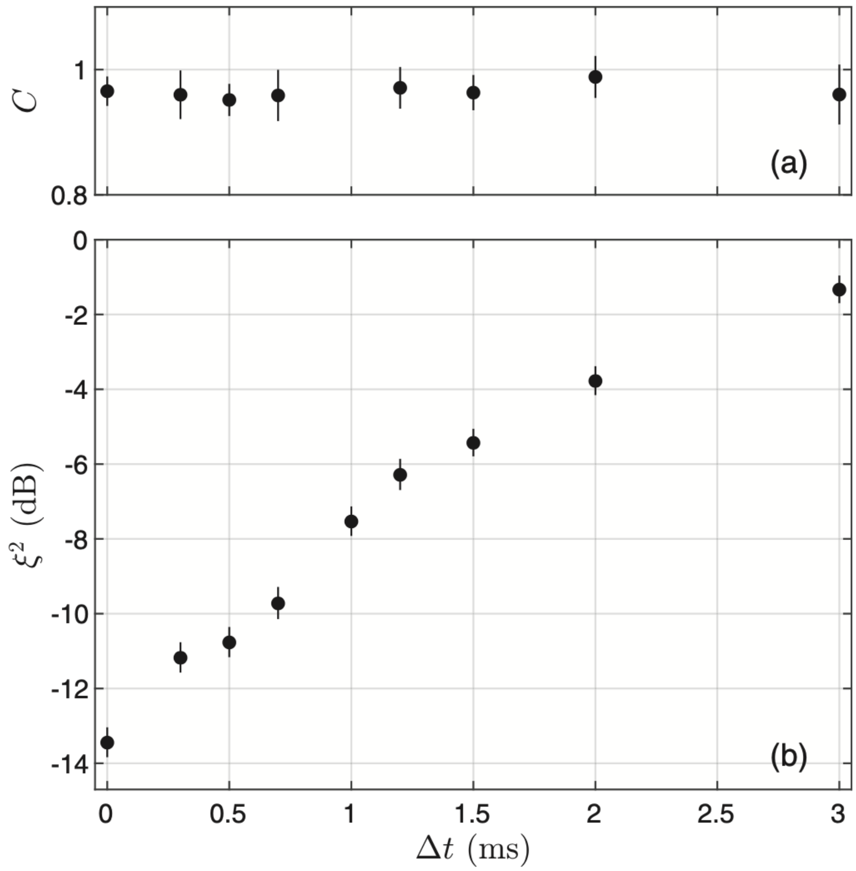

Figure 4.5: (a) Coherence of atoms during free falling and (b) retrieved metrologically-relevant squeezing ξ^2 as a function of free-fall time Δt. Error bars indicate 68% confidence interval.

C of the ensemble. Using the notation defined above, the Wineland parameter ξ^2 takes the form

$$\xi^2 = \left(\frac{\Delta\theta}{1/\sqrt{N_r}} \, \frac{1}{C} \right)^2 . \tag{4.19}$$

Experimentally, we characterize C with an additional microwave $\pi/2$ rotation just before recapturing the atoms. We find $C \simeq 0.96$, independent of the release time [see Figure 4.5(a)]. Figure 4.5(b) shows the inferred Wineland parameter as a function of Δt, given the measurements of $\Delta\theta$ and N_r with $N \sim 500,000$ atoms. Despite substantial loss of homogeneity, metrologically relevant squeezing is observed to persist for time scales as long as 3 ms. We can recover most of the initial squeezing ($\sim$ 13dB) for shorter release times ($\Delta t < 1$ ms).

Although the successful retrieval of squeezing was limited to ~ 3 ms free-fall times in this work, a substantial extension of this duration should be possible using a significantly colder atomic ensemble and a vertical cavity orientation with respect to gravity. We expect the model used to quantify the loss of squeezing to be useful in designing and predicting the performance of future squeezed-state sensors especially for those that require high bandwidth readout.

4.4 Experimental details

4.4.1 Cavity readout

We measure resonance frequency shifts of a high finesse optical cavity to infer the atomic state and calibrate the atom number in this experiment.

Linewidth broadening

The cavity frequency shift is measured by comparing the time-dependent homodyne signal to a normalized template taken in absence of atoms. Corrections for nonlinearities of the cavity frequency response and linewidth broadening factor κ_s due to atomic scattering are applied in the same way as in [24, 44]. However, the atom-cavity coupling is less homogeneous for the second probe after release-recapture, this effect changes the linewidth broadening factor to $\langle\eta\rangle_e\kappa_s$.

Measurement of maximum cavity frequency shift and $\langle\eta\rangle_e$

To measure the maximum cavity frequency shift and $\langle\eta\rangle_e$, we prepare all the atoms in $|\downarrow\rangle$ state. Since $500,000$ $|\downarrow\rangle$ state atoms give a cavity resonant frequency shift of more than 1MHz which is far more than the cavity linewidth $\sim$ 10kHz, we use a different method to measure the cavity frequency shift than the back-to-back method [24]. In this new method, the 780 nm probe is on continuously through the release-recapture (RR) sequence and its frequency is scanned from $+50$kHz to -50kHz detuned from cavity resonance in $200\mu s$ that overlaps with the time when the second probe is on during the RR sequence in the back-to-back method. This scan gives a dispersive signal by the homodyne detection when no atom is loaded. An example of this dispersive signal is shown in Figure 4.6. This dispersive signal changes its shape due to the added $|\downarrow\rangle$ atoms. Adjusting the starting frequency of the frequency scan brings the dispersive signal back to empty cavity shape, though the frequency range of the scan remains 100kHz. The amount of adjusted frequency tells the maximum cavity frequency shift caused by the amount of added atoms which is counted by fluorescent imaging.

Due to the bandwidth of the laser frequency lock, the maximum adjustment on the frequency scan starting point is limited to $\sim$ 900kHz. This also limits the maximum added atom number to

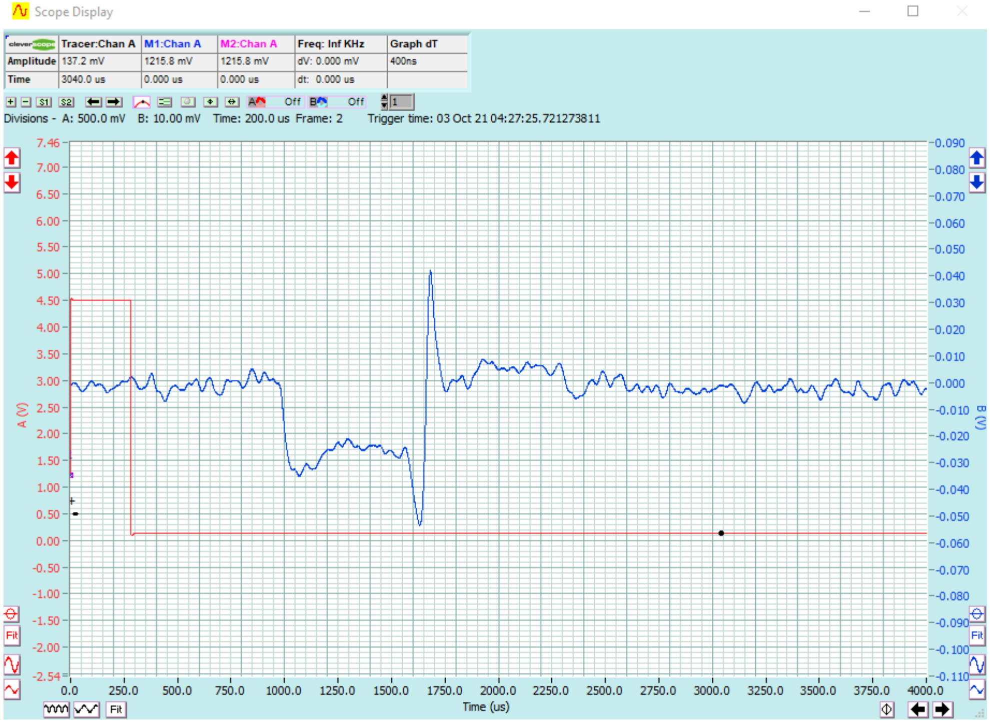

	Tracer:Chan A	M1:Chan A	M2:Chan A	Freq: Inf KHz	Graph dT
Amplitude	137.2 mV	1215.8 mV	1215.8 mV	dV: 0.000 mV	400ns
Time	3040.0 us	0.000 us	0.000 us	dt: 0.000 us	

Divisions - A: 500.0 mV B: 10.00 mV Time: 200.0 us Frame: 2 Trigger time: 03 Oct 21 04:27:25.721273811

Figure 4.6: Dispersive signal for maximum cavity frequency shift measurement. The blue trace is the homodyne signal. The dispersive shape is due to the frequency scan of the probe. No atom is loaded for this signal.

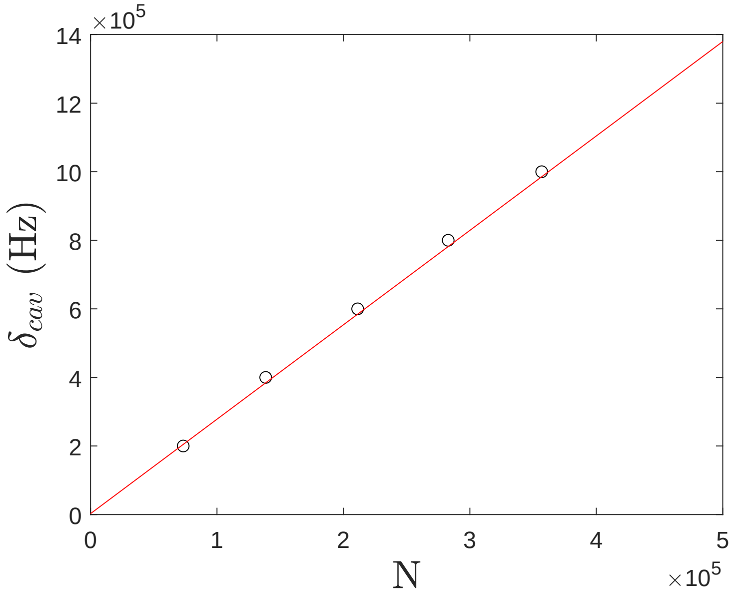

Figure 4.7: Maximum cavity frequency shift as a function of atom number. The data is taken for 0.7ms release time. The red line is a linear fit of the data points

$\sim 300,000$. To get the maximum cavity frequency shift for all different atom number ($\sim 50,000$, $100,000$ and $500,000$ in this work) and reduce uncertainties, we measure this shift as a function of atom number and fit this function with a straight line (as expected). Figure 4.7 shows an example of this relation for 0.7ms release time. The maximum cavity frequency shift that corresponds to a specific atom number is found by interpolation or extrapolation.

We measure and linearly fit this frequency shift as a function of atom number for each release time. The slope of each fitting is proportional to $\langle\eta\rangle_e$ with the same constant of proportionality. This constant can be calculated by fitting of the zero release time data whose $\langle\eta\rangle_e = 0.9254$ is known [24]. $\langle\eta\rangle_e$ for other free-fall times are thus calculated.

4.4.2 Coherence Measurement

The coherence of the atomic state is measured by a microwave-induced Ramsey oscillations. The first Ramsey $\pi/2$ pulse is the composite $\pi/2$ microwave pulse at the beginning of the experimental sequence to prepare the initial superposition state where the atoms are trapped by the lattice. The second $\pi/2$ pulse is applied after atoms have freely fallen for a certain amount of time. The phase of this pulse is adjusted to be roughly 90° to the phase of the atomic coherence by a frequency shift key and is scanned by a small amount. This scan covers the bottom (top) part of the Ramsey fringes. A quadratic fit is applied to this part of the fringes. An example of the data for 2ms release time is

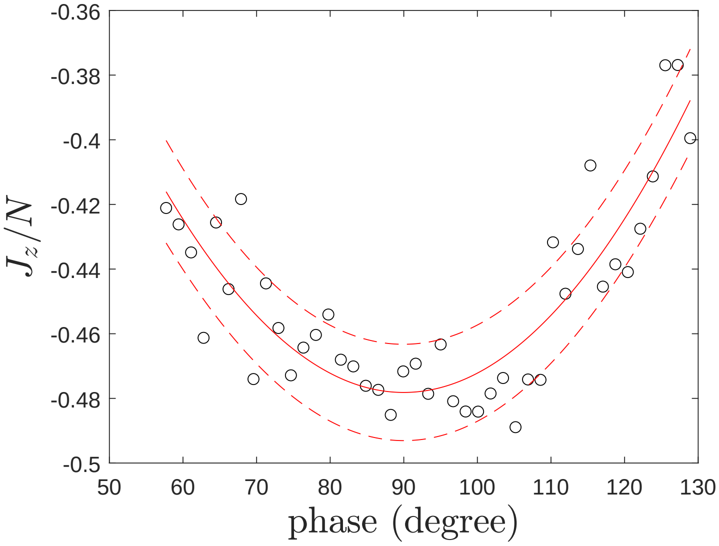

Figure 4.8: Coherence measurement. The release time for this data is 2ms. To measure the coherence of the atoms, the Ramsey fringe is scanned near the bottom. Two times the minimum of the fitted curve (red solid line) gives the coherence. The red dashed lines give 68% prediction uncertainty.

shown in Figure 4.8. Two times the lowest (highest) point of this fit stands for the coherence. Two times the 68% prediction interval of that point gives the uncertainty on the coherence measurement. Every step in the sequence before the release remains the same as the squeezing measurement. Since the cavity resonance is shifted out of the cavity linewidth, a fluorescence population spectroscopy is used to measure the collective J_z. This coherence is measured with $\sim 500,000$ atoms.

4.4.3 Delta-Kick protocol

In the delta-kick protocol (Figure 4.9), we utilize a series of lattice on-off sequences to reshape the phase space (position-momentum space) distribution of the atomic cloud. The timing in this protocol is based on a simulation assuming the lattice is a harmonic trap and is experimentally chosen (see Table 4.1). This protocol gives less coherence ($< 92\%$) compared to the RR protocol irrespective of release times, because the extra lattice on-off sequences induce more inhomogeneous AC-Stark shifts on the atoms. The metrologically-relevant squeezing decreases to 0 in less than 5ms release times.

4.4.4 Uncertainty calculations

We calculate uncertainties using standard error propagation formula where the uncertainty of each quantity represents a 68% confidence interval. These quantities are assumed to be independent and their errors are assumed to follow normal distributions. When determining the uncertainties of

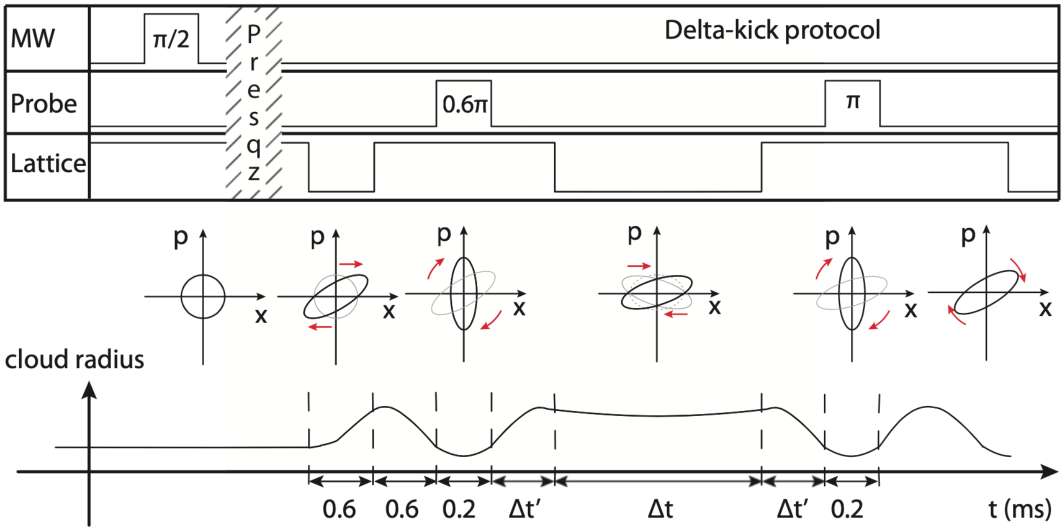

Figure 4.9: Delta-kick protocol: timing sequence (top), illustration for phase-space evolution of the atomic cloud in the transverse direction of the cavity (middle), illustration for rms transverse cloud size evolution (bottom). In the phase space illustration, clouds are modeled to execute harmonic oscillations when trapped in the lattice. MW: microwaves; Presqz: pre-squeezing by one-axis twisting; $\pi/2$: composite microwave pulse that prepares the 50-50 superposition state; 0.6π and π: probe power expressed in terms of the AC-Stark phase shifts induced between the two atomic states; $\Delta t'$: short free-fall time for atomic phase space reshaping; Δt: free-fall time. The values for $\Delta t'$ and Δt are shown in Table 4.1.

$\Delta t'$ (ms)	Δt (ms)
0.8	0.4
0.7	0.7
0.6	1.2
0.5	1.4, 2.0, 3.0, 4.0, 5.0, 6.0, 7.0

Table 4.1: The delta-kick protocol timing sequence. $\Delta t'$ stands for the short release time before the measurement sequence to reshape the phase space distribution of the cloud. Δt is the release time that is used for free space atomic sensors. Their definitions are seen in Figure 4.9.

$\Delta\theta$, only statistical uncertainty on cavity frequency measurements is considered. This uncertainty is estimated by a bootstrapping method where we re-sample 10 000 times from the measured frequency distribution, calculate 10 000 standard deviations from the resampled data and estimate this uncertainty as the standard deviation of these 10 000 standard deviations. Whereas the uncertainty of squeezing include uncertainties on cavity frequency and atom number measurements.

4.5 Application to Fluorescence imaging

To apply the theory developed here to other situations involving coupling inhomogeneity, we need to convert the inhomogeneity into the atom basis.

In fluorescence imaging, atoms in two atomic states are spatially separated. Since J_z is half the population difference between the two states, it is measured by shining a slightly red detuned beam on the atoms and counting the photon number scattered by each states. We can write J_z as:

$$J_z = \frac{1}{2}(\alpha \sum_{i=1}^{n_\uparrow} c_i - \alpha \sum_{i=1}^{n_\downarrow} c_i) = \frac{1}{2}\alpha \sum_{i=1}^{n} \tilde{c_i} \tag{4.20}$$

where α is the conversion factor from photon counts to atom number, $n_\uparrow$ ($n_\downarrow$) stands for the pixels that collect photons emitted by $|\uparrow\rangle$ ($|\downarrow\rangle$) atoms, n is the total pixel number, c_i is the photon number collected by the i^{th} pixel, and

$$\tilde{c_i} = \begin{cases} c_i, & i \in n_\uparrow \\ -c_i, & i \in n_\downarrow \end{cases}.$$

This equation of J_z is in the pixel basis. We now convert it to the atom basis. Assume pixel i collects photons from N_i atoms and each atom corresponds to a pixel, we label each atom as (i, j). This assumption is valid because the picture taken by the camera is an image of the atom cloud. The spatial location of each atom maps to the pixels on the camera. Using this label, (i, j) corresponds to the pixel index i that collects photons emitted by j^{th} atom where j runs from 1 to N_i and i runs from 1 to n. Atom (i, j) corresponds to c_{ij} photons. Thus, $c_i = \sum_{j=1}^{N_i} c_{ij}$. We can write J_z as:

$$\begin{aligned} J_z &= \frac{1}{2}(\alpha \sum_{i=1}^{n_\uparrow} \sum_{j=1}^{N_i} c_{ij} - \alpha \sum_{i=1}^{n_\downarrow} \sum_{j=1}^{N_i} c_{ij}) \\ &= \alpha \sum_{i=1}^{n} \sum_{j=1}^{N_i} c_{ij} j_z^{(ij)} \end{aligned} \tag{4.21}$$

where

$$j_z^{(ij)} = \begin{cases} \frac{1}{2}, & i \in n_\uparrow \\ -\frac{1}{2}, & i \in n_\downarrow \end{cases}$$

Assume within each pixels, the photon to atom number conversion factor is the same, i.e. $c_{ij} = 1/\beta_i$, J_z becomes

$$J_z = \sum_{i=1}^{N} \frac{\alpha}{\beta_i} j_z^{(i)}. \tag{4.22}$$

This assumption is valid because the imaging beam is homogeneous across the atom cloud due to saturation effects and the photon collection geometry is similar within one pixel. Thus $\eta_i = \alpha/\beta_i$.

We estimate the increase in variance in fluorescence imaging due to loss of coupling homogeneity to be 0.5% [63].

Chapter 5

Camera retrieved free space spin squeezing and fountain clock sequence below quantum projection limit

In this chapter, we retrieve cavity generated spin squeezing from free space using a camera method. The camera can measure J_z because J_z stands for half the population difference and the camera can be used to count the atom number in different states. This is done by spatially separating the two atomic states, counting the fluorescence photons emitted by the atoms at different locations, and inferring the atom number from the photon counts. This method is destructive and is called fluorescence population spectroscopy. The success of this method requires high fidelity atom counting by fluorescence imaging. Previous experiments have shown that fluorescence imaging is used to detect trapped ions [64], count single ^{87}Rb atoms [65], and detect spin-nematic quadrature squeezing in a spin-1 ^{87}Rb BEC system [66]. Here we demonstrate that fluorescence population spectrsocopy, when correlated to an initial QND J_z measurement, is able to reveal 5.8(0.6)dB metrological squeezing with $390,000$ atoms from free space. The squeezing level remains constant up to 4ms release time. This shows that squeezing survives atomic expansion and free fall. Particularly in our case, the atomic cloud expansion is from 17μm to roughly 200μm rms radius and the free fall is roughly 80μm in 4ms.

Since the camera method maintains squeezing for longer release time compared to the cavity method, we apply this method to realize a fountain clock sequence that performs below quantum projection limit. This sequence is called free space Ramsey spectroscopy. In our experiment, this sequence is realized with $240,000$ atoms and gives a single-shot fractional frequency instability of 8.4×10^{-12} at 3.6ms interrogation time, 3.8(0.2)dB below quantum projection limit.

Some parts of this chapter are adapted from [67].

5.1 Fluorescence Imaging

To do fluorescence population spectroscopy below the quantum projection limit, we installed a new fluorescence imaging system with a CMOS camera. Details and calibrations for the fluorescence imaging system can be found in [67, 68]. Here I provide a brief summary.

This camera is FLIR Blackfly S model BFS-U3-32S4M-C. It contains a 7.0mm by 5.3mm Sony IMX252 CMOS sensor whose pixel size is 3.45μm (3.2Mpx total). The camera is attached to a 1:1 relay lens system placed ~ 5 cm away from the atoms to collect light emitted by the atom clouds. The lens has focal length of ~ 5cm and diameter of ~ 25mm, giving a numerical aperture (NA) of ~ 0.25. This system is able to collect ~ 65 photons per atom over 3ms exposure time with a camera quantum efficiency of 35% at 780nm.

To separate atoms at different states, a push beam that is on resonance with the $|F = 2, m_F = 0\rangle$ ground state to the excited state transition is applied for 37μs. This push beam gives a momentum kick only to the atoms in the $|F = 2, m_F = 0\rangle$ state. After some time, the atoms at different states are separated into two clouds.

Then an imaging beam is applied and simultaneously excites both clouds. The simultaneous imaging reduces noises from sensor gain variations and imaging light intensity and frequency fluctuations [69]. The imaging beam is retroreflected and is 0.2Γ red detuned from the $|F = 2\rangle$ to excited state transition to reduce heating. A repump beam that is on resonance with the $|F = 1\rangle$ to excited state transition is used in the meantime to repump the atoms from $|F = 1\rangle$ state back to $|F = 2\rangle$ state for continuous fluorescencing. While the imaging beam is on, the camera collects fluorescent photons from the atom clouds and forms an image. In the image, each cloud is spatially well resolved with little overlap between them. Typical cloud sizes imaged by the camera are 3mm in diameter. The atom number is inferred from photon counts in the region of interest. Figure 5.1 is an example of the images taken by the camera. Figure 5.2 is an illustration for the imaging procedure.

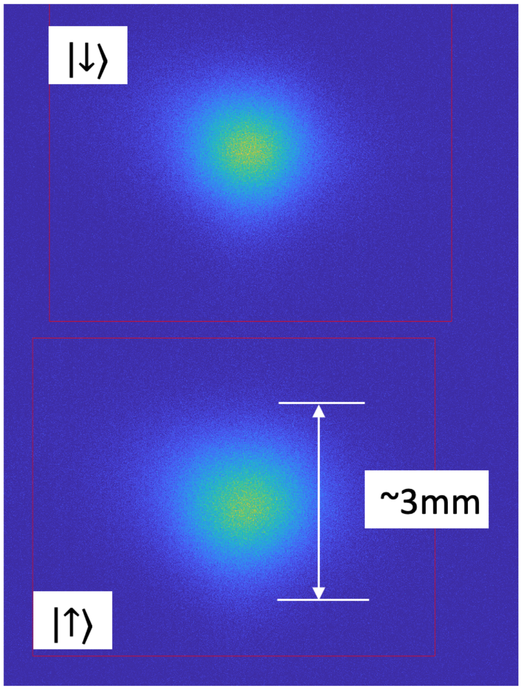

Figure 5.1: An example of the atom cloud images. The $|\uparrow\rangle$ and $|\downarrow\rangle$ atoms are well separated spatially with little overlap between the two clouds. The cloud size is about 3mm in diameter. The photon numbers are counted in the regions of interest (ROI) as shown by the red boxes. Atom number at different states are inferred from the photon counts. In this case, there are about 390 000 atoms. The exposure time is 3ms.

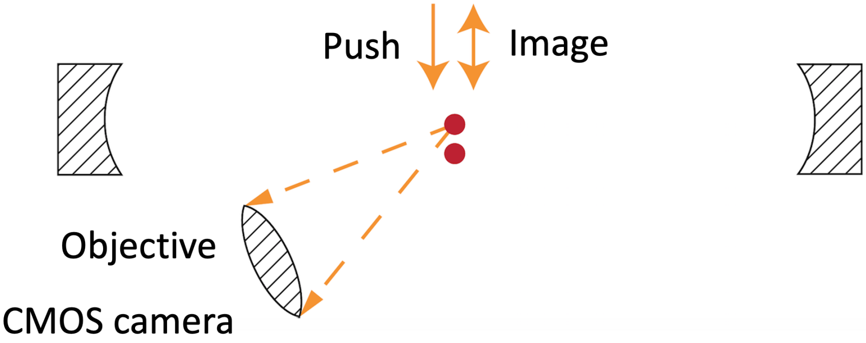

Figure 5.2: Illustration of the fluorescence imaging procedure. The imaging beam is applied vertically and is retroreflected. The push beam is also in the vertical direction. The objective lens of ~ 25mm diameter is about 5cm away from the atom clouds to collect fluorescent photons and form an image on the CMOS camera.

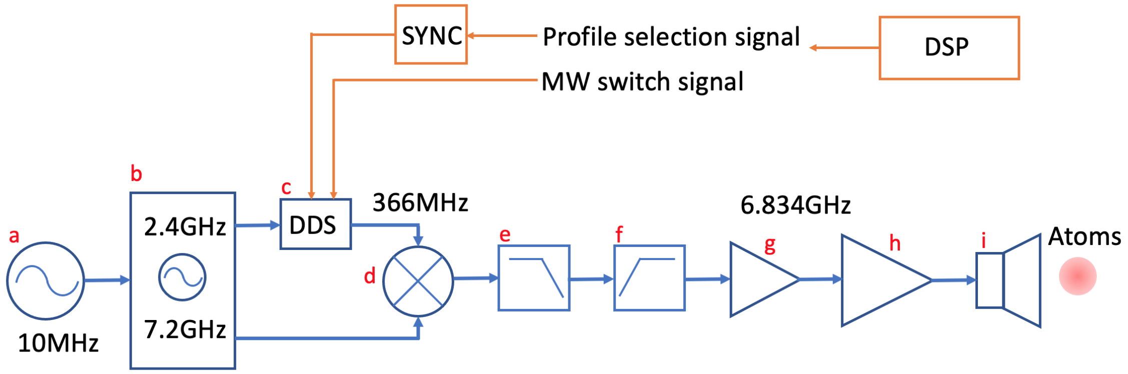

Figure 5.3: Schematic of the new microwave system. The blue components form the frequency chain of the microwave system: a. Hewlett Packard 10811-60111 10MHz crystal oscillator; b. Wenzel 2.4GHz and 7.2GHz Golden Multiplied Crystal Oscillator (P/N: 501- 30459); c. Analog Device AD9914 direct digital synthesizer; d. Mini Circuit frequency mixer ZX05–153LH-S+; e. Low pass filter: 2 Mini Circuit VLF-6400+ and 2 RF-Lambda RLPF13G07; f. High pass filter: 2 Mini Circuit VHF-6010+; g. Mini Circuit low noise amplifier ZX60-83LN-S+; h. Mini Circuit high power amplifier ZVE-8G+. The orange components represent the control parts: digital signal processor (DSP) is the control system that sends profile selection signals and microwave switch signals to the direct digital synthesizer (DDS); SYNC is the interface circuit that makes the profile selection signals from the DSP readable by the DDS.

5.2 Low Phase Noise Microwave System

Phase noise from the interrogation microwave signal in free space Ramsey sequence will deteriorate the application of squeezing. Our old microwave system has high phase noise that limits the performance of the Ramsey sequence. To demonstrate free space Ramsey spectroscopy below quantum projection noise with a few milliseconds interrogation time, we developed a low phase noise microwave system.

5.2.1 Frequency Chain

The details about the microwave frequency chain is shown in Figure 5.3. The hyperfine transition frequency of 6.834GHz is generated by mixing a 7.2GHz oscillator with a 366MHz direct digital synthesizer (DDS) signal and filtering out the upper sideband. The DDS clock is fed by the 2.4GHz frequency harmonics of the 7.2GHz oscillator. The 7.2GHz oscillator is phase locked to a 10MHz initial clock with type 2 loop and bandwidth < 10Hz.

Phase noise decreases when down converting frequency. This frequency chain design improves the phase noise performance in two ways: 1. it generates the desired frequency (6.834GHz) from a higher frequency (7.2GHz); 2. it uses low phase noise components such as the 7.2GHz oscillator and the AD9914 DDS.

5.2.2 Interface Circuit

Ramsey spectroscopy requires multiple microwave pulses with different phases or frequencies. We adjust the microwave parameters by phase shift key (PSK) or frequency shift key (FSK) to the AD9914 366MHz signal. To do PSK and FSK, we use the profile mode of the AD9914 with an Analog Device control software user interface. In the profile mode, the AD9914 has 8 profiles with pre-programmed frequencies, phases, and amplitudes. The profiles are selected according to the applied voltages on the 3 external profile selection pins on the AD9914 evaluation board. In order to select profiles correctly, the voltages applied to the 3 pins have to satisfy a certain setup time, requiring a fixed timing (synchronization) with the DDS internal clock (100MHz). However, in our experiment, this profile adjustment voltages are output from a digital signal processor (DSP) whose timing does not hold fixed to the DDS internal clock. Therefore, we designed and built an interface circuit to synchronize the profile adjustment voltages from the DSP to the AD9914 internal clock. This synchronization is implemented by D flip-flops. For FSK, it is also important to remain at a certain profile for a fixed amount of time every cycle. The interface circuit therefore includes a few more components besides D flip-flops to eliminate FSK duration jitters. These components are logical gates, binary counters, and clock buffers. The circuit diagram is shown in Figure 5.4. To sum up, this interface circuit takes in 3 digital voltage signals from the DSP (labeled as D0, D1, and D2 in the circuit diagram) and outputs 3 synchronized signals (labeled as O1, O2, and O3 in the circuit diagram) to the AD9914 profile selection pins. The synchronized signals have durations of multiples of 160ns plus an offset and are fixed every cycle.

5.2.3 Microwave switch

The 6.834GHz microwave is turned on and off by switching on and off the DDS output. When the DDS is off, the 6.834GHz signal is gone and the microwave only outputs a 7.2GHz signal. 7.2GHz is far detuned from the atomic transition, thus having no effect on the atoms. The microwave is effectively off. This method has high isolation and reduces phase shifts from the microwave switching.

5.3 Phase Noise Characterization

5.3.1 Additive phase noise measurement

Additive phase noise due to electronics after the initial clock is measured as shown by Figure 5.5. A 10MHz low phase noise crystal oscillator signal is split into two and each feeds a microwave (MW) chain. Thus, the measurement circuit contains two branches. Each branch has a microwave chain whose additive phase noise is to be measured. The two microwave chains are identical copies and

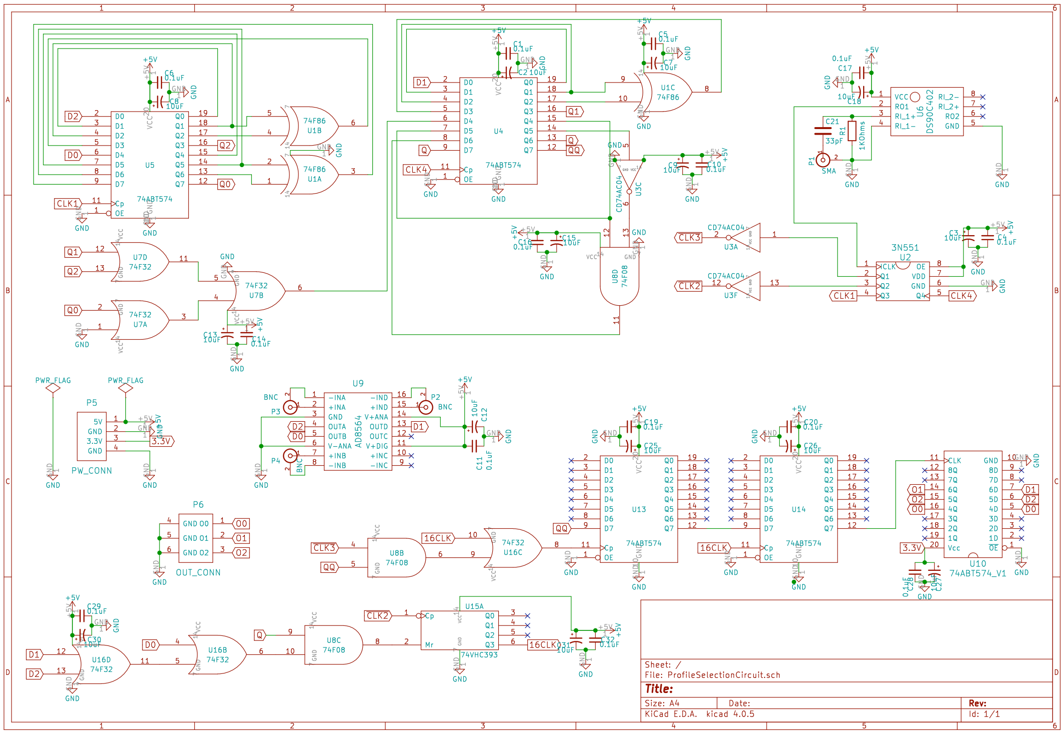

Figure 5.4: Circuit diagram for the interface circuit in the low phase noise microwave system. In the diagram, D1, D2, and D3 are the digital inputs from the DSP. O1, O2, and O3 are the digital outputs from this circuit. P1 is the synchronizing clock signal from the AD9914.

assumed to have the same additive phase noise. One of the branches has a phase shifter, while the rest of the two branches remain close in length in order to cancel the phase noise contribution from the initial clock effectively. The two branches are then routed to the RF and LO ports of a double-balanced mixer. The mixer functions as a phase detector. When the two branches are in quadrature, adjusted by zeroing the mixer IF output with the phase shifter on one of the branches, its IF output is proportional to the additive phase noise. This is proved as follows:

The signals of the branches are $V_1 = A_1 \sin(\omega t + \phi_0 + \Delta\phi_1)$ and $V_2 = A_2 \cos(\omega t + \phi_0 + \Delta\phi_2)$. Here, $\Delta\phi_1, \Delta\phi_2 \sim 0$ are the additive phase noise we want to measure. Using the multiplicative trigonometric identities,

$$V_1 V_2 = \frac{A_1 A_2}{2}[\sin(\Delta\phi_1 - \Delta\phi_2) + \sin(2\omega t + \Delta\phi_1 + \Delta\phi_2)]. \tag{5.1}$$

In this equation, there are two terms: one is twice the branch frequency, and the other is a DC term. The mixer IF output is proportional to the DC term since the high frequency term is filtered. We also have

$$\sin(\Delta\phi_1 - \Delta\phi_2) \approx \Delta\phi_1 - \Delta\phi_2,$$

because $\Delta\phi_1, \Delta\phi_2 \sim 0$. The IF output becomes:

$$V_{IF} = K(\Delta\phi_1 - \Delta\phi_2) \tag{5.2}$$

where K is a factor that converts phase into voltage. We measure K by phase shifting one branch by a known amount and measuring the corresponding voltage change at the mixer IF output. The phase shift need to be small in order to be in the linear regime.

The mixer IF output is then amplified by a low noise pre-amplifier (SR560). The amplified signal is measured by a spectrum analyzer, which reads out the power spectrum density. The power spectrum density has unit of $\mathrm{V}/\sqrt{\mathrm{Hz}}$ and it is converted to phase noise dBC/Hz by dividing the amplifier gain and the conversion factor K, taking the $\log_{10}$, and multiplying 20. We assume the additive phase noise of the two microwave chains to be uncorrelated. Thus, the phase noise for a single microwave chain is 3dB lower than what is measured from the spectrum analyzer. We have already assumed $\Delta\phi_1 \approx \Delta\phi_2$ to get this result. We measured the total additive phase noise from two MW chains and compare the results of both the new MW chain and the old MW chain in Table 5.1.

5.3.2 Absolute phase noise measurement

We want to examine if the initial clock introduces any extra noise to the microwave chain. This extra noise can easily come from improper grounding (ground loops), power supplies, interference

frequency (Hz)	phase noise (dBc/Hz)(new/old)
10	-69/-71
100	-96/-85
1,000	-120/-104
10,000	-134/-108
100,000	-140/-107

Table 5.1: The additive phase noise of the old and new microwave chains. The values are upper bounds since they are the total phase noise of the two branches in the measurement. The old microwave source limits the interrogation time to less than 1ms. The new microwave source has better performance at higher offset frequency and is expected to give squeezing for interrogation time larger than 1ms.

etc. To check the extra noise from the initial clock, we feed two independent microwave chains with two different initial oscillators (Wenzel small fry and HP crystal oscillator) and monitor the low frequency part of their beat signal.

When the two microwave chains are locked to different initial oscillators, the frequency of the two are not exactly the same and the phase between them is not a fixed value. We are not able to get a stable DC signal that is proportional to the phase noise as in the additive phase noise measurement case. However, when the low frequency part of the beat signal is close to 0, it is proportional to the total phase. Therefore, we adjust the frequency of the two microwave chains to be as close as possible and measure the low-passed beat signal only when it is close to 0. We are able to get a beat signal at 0.3Hz. With this frequency, the beat signal does not change its value significantly within 10ms. We measure the low passed amplified beat signal on an oscilloscope triggered by zero crossing with time span of 10ms. The trace directly reflects the phase jitter in the time domain. Phase noise at frequency higher than 100Hz is revealed by the trace. We find that when the two initial clocks are Wenzel and a HP crystal oscillator, a 1KHz oscillation shows up in the oscilloscope trace. However, this oscillation does not show up when the initial clocks are two HP crystal oscillators. We conclude that Wenzel small fry introduces phase noise peaked at 1KHz and decide not to use it as the initial clock. The initial clock in our experiment is selected to be the HP crystal oscillator.

5.3.3 Phase excursion due to microwave switch

Since we are sending microwave pulses to the atoms, we need to switch the microwave on and off. One possibility is to use a microwave switch. We measure the phase excursion on the microwave pulses due to the microwave switch. The measurement circuit is the same as Figure 5.5 except that the spectrum analyzer is replaced by an oscilloscope, and the measured voltage is converted to the phase by dividing the conversion factor K and the amplifier gain. For the phase excursion measurement, one branch is connected to a continuous signal, while the other branch is connected to

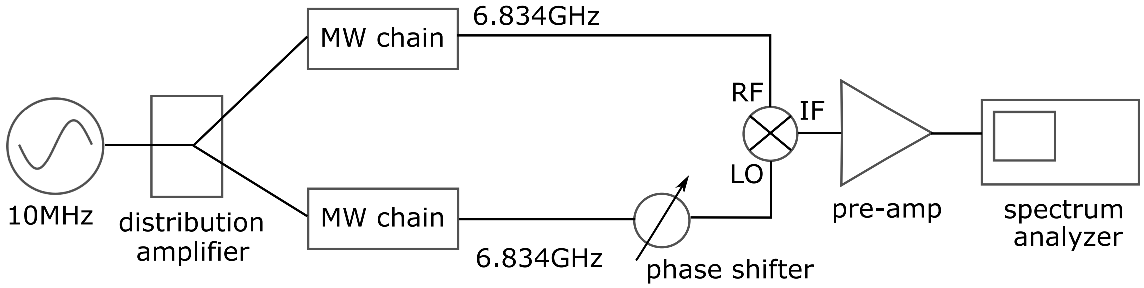

Figure 5.5: Additive phase noise measurement. A 10MHz crystal oscillator is used to fed two MW chains through a distribution amplifier. One of the two MW chains connects directly to the RF port of a double balanced mixer. The other MW chain passes through a phase shifter and then connects to the LO port of the mixer. The phase shifter ensures the two MW chain signals are in quadrature at the mixer. The IF output of the mixer, proportional to the phase noise of the MW chain, is then amplified by a low noise pre-amp. The power spectrum density of the amplified signal is measured by a spectrum analyzer. The path lengths of the two MW chains are kept similar except for the phase shifter.

a pulsed signal. The measured phase excursion during the microwave pulses is shown in Figure 5.6.

5.4 Camera retrieved free space spin squeezing

5.4.1 Protocol

Figure 5.7 presents the experimental sequence for the camera method to retrieve free space spin squeezing. Similar to the cavity method, we prepare spin squeezed states with a cavity J_z measurement and then release the atoms into free space. But unlike the cavity method, after release, we do not need to recapture the atoms back into the cavity mode any more. The camera measures the J_z of freely moving atoms at the end of the experimental sequence. This is represented by the fluorescence part in Figure 5.7. The release time is the time between lattice release and push beam on (part of the camera J_z measurement to separate atoms at different states). To retrieve spin squeezing, the camera J_z measurement is correlated to the probe (cavity) J_z measurement.

5.4.2 Squeezing Results

Two corrections are implemented when retrieving spin squeezing by the camera method. The first is the pushed cloud position correction to the camera measured J_z. Due to intensity fluctuation of the push beam, the pushed cloud position varies shot to shot. Because the photon collection efficiency depends on the cloud position, the photon number collected from the pushed cloud varies with the cloud position even if the pushed atom number remains unchanged. This leads to the camera measured J_z dependence on the pushed cloud position, if we do not count for the position

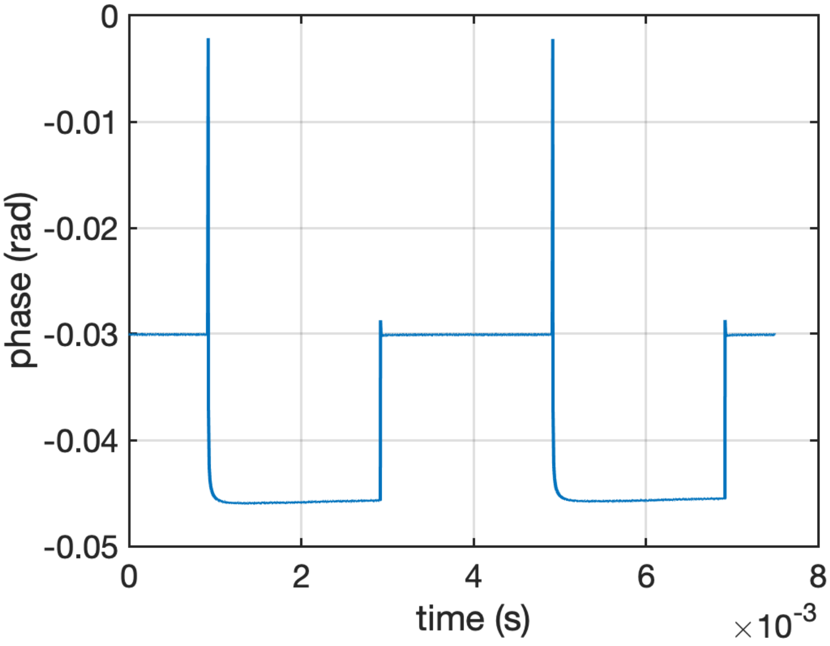

Figure 5.6: Phase excursion due to microwave switches. The blue trace is the phase difference between the mixer RF and LO inputs converted from the voltage output of the pre-amp as shown in Figure 5.5. To get the signal, the mixer RF input is connected to a continuous MW signal with constant phase, and the LO input is connected to a pulsed MW signal. Since the RF input is constant phase, the change in phase reflected by the trace is a result of the phase excursion due to the LO input, i.e. the pulsed signal. The phase of the pulsed signal starts at one phase (−0.002rad) and then changes to another phase (−0.046rad) while the pulse is on.

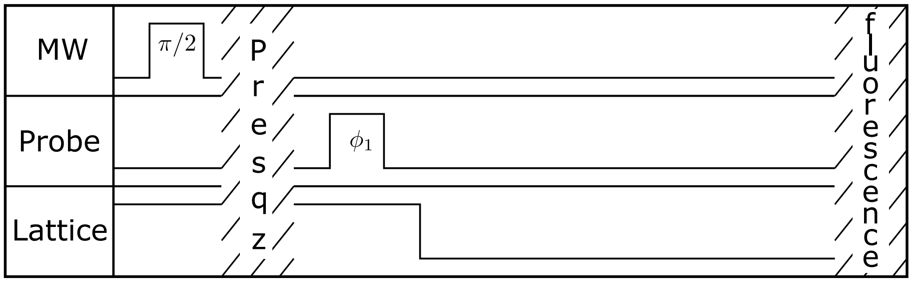

Figure 5.7: Sequence for spin squeezing retrieval by the camera. The atoms are released from the lattice after being squeezed by the first cavity J_z measurement. While the atoms are moving freely in space, fluorescence imaging is applied to measure the J_z by the camera. Squeezing is retrieved by correlating the camera J_z and the cavity J_z.

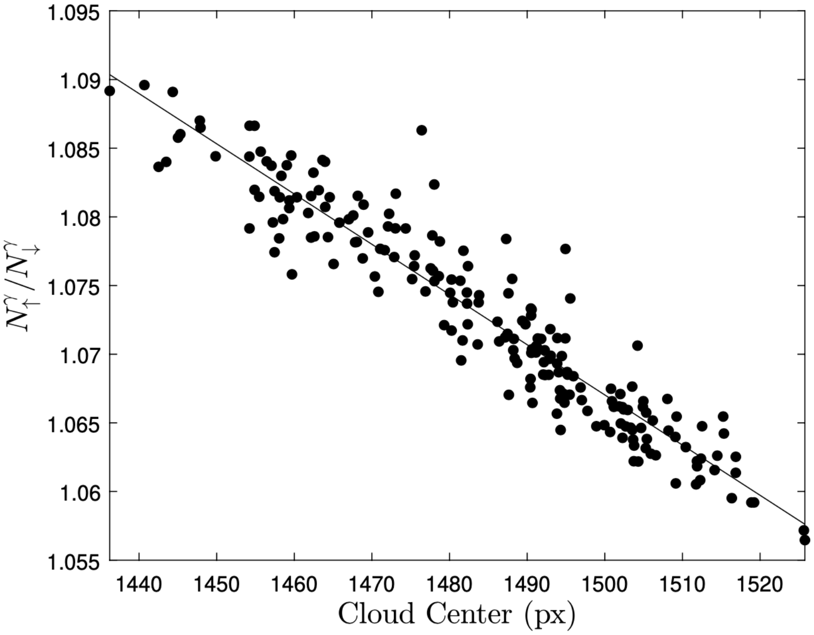

Figure 5.8: Photon count ratio between $|\uparrow\rangle$ and $|\downarrow\rangle$ atoms as a function of pushed cloud's center. Solid line is a linear fit to the data. The atomic state is prepared on the equator of the Bloch sphere. Thus, the atom numbers are the same for $|\uparrow\rangle$ and $|\downarrow\rangle$ states. The photon count ratio reflects the photon collection efficiency ratio between the two atomic states.

dependence of the pushed cloud photon collection efficiency and artificially assume the collection efficiency to be constant. This camera measured J_z is incorrect because the pushed cloud atom number is counted incorrectly. To get the correct atom number from the pushed cloud, we need to calibrate the pushed cloud photon collection efficiency as a function of the cloud position. This is done by preparing a squeezed state on the Bloch sphere equator and measure the photon count ratio between the pushed and unpushed clouds as a function of the pushed cloud position as shown in Figure 5.8. Because the two states have the same atom number when the system state is prepared on the equator, this photon count ratio reflects the photon collection efficiency ratio between the pushed and unpushed clouds. Since the photon collection efficiency remains fixed and well-known for the unpushed cloud, we get the position dependence of the pushed cloud photon collection efficiency from this ratio.

The second is a beatnote correction on the cavity measured J_z. The beatnote is from mixing the probe light and the cooling light as described in subsection 3.4.3. It reflects the probe light detuning with respect to the atomic transitions. After the cloud position correction is done on the camera measured J_z, we find the corrected J_z is correlated to this beatnote as shown in Figure 5.9. This shows that the preparation of J_z depends on the beatnote. However, we do not observe this

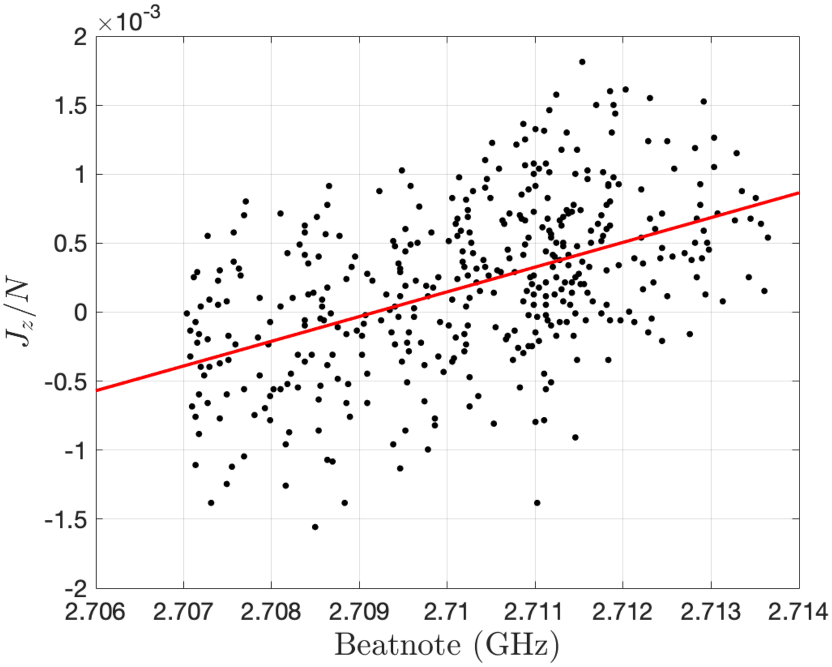

Figure 5.9: Beatnote dependence of normalized camera measured J_z. The red solid line is a linear fit to the data

correlation between the cavity measured J_z and beatnote. This is because the beatnote effect from the cavity measurement (see Equation 2.41) exactly cancels that from J_z preparation. Based on Equation 2.41, we derive the correction on cavity measured J_z:

$$J_z^{\text{corrected}} = J_z^{\text{measured}} + \frac{1}{2}\frac{N\delta}{\Delta} \tag{5.3}$$

where $J_z^{\text{corrected}}$ is the corrected cavity measured J_z, J_z^{measured} is the cavity measured J_z before correction, N is the atom number, δ is the beatnote shift from 2.71GHz, and $\Delta = 3.417\text{GHz}$ is the mean detuning of the probe.

After these two corrections, the camera measured J_z is correlated to the cavity measured J_z. Their correlation is shown as Figure (b) in Figure 5.10. Figure (a) in Figure 5.10 shows the correlation between two back-to-back cavity measured Jz for comparison. In our experiment, we use $390,000$ atoms and the correlation between the back-to-back cavity measured J_z reveals $\sim$ 14dB variance reduction, while the correlation between the camera and cavity measured J_z reveals 6.6(0.6)dB variance reduction (shown by the black solid line in Figure 5.11).

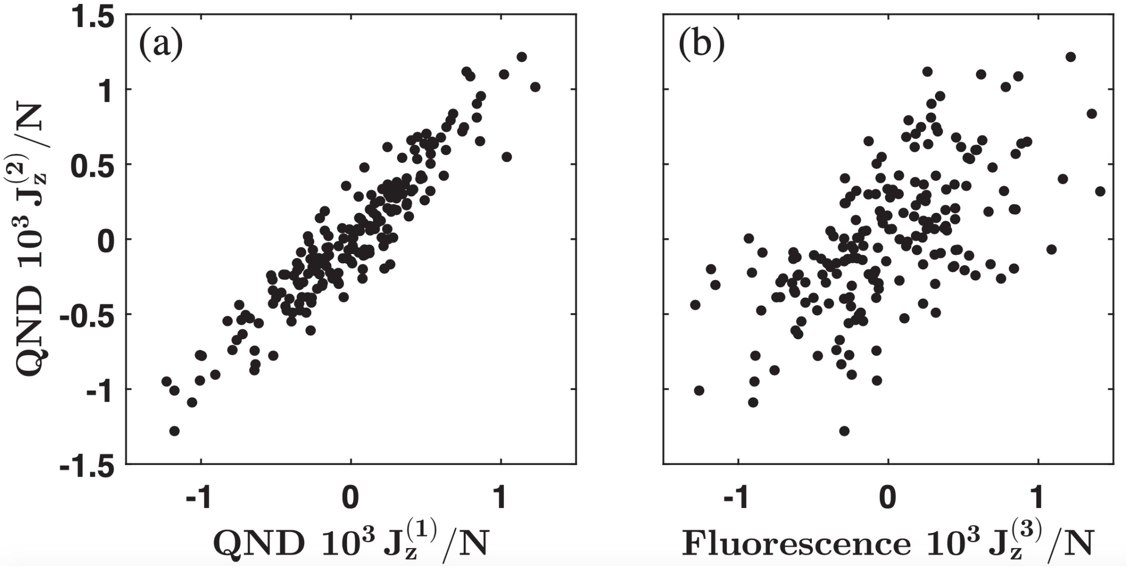

Figure 5.10: Correlations between J_z/N measurements for 390,000 atoms. $J_z^{(1)}$ and $J_z^{(2)}$ are cavity QND measurements. $J_z^{(3)}$ is the camera measurement. These J_z values are measured sequentially. (a) shows the correlation between two cavity measurements. It presents a stronger correlation than that of the cavity-camera measurements (b)

We also measured metrologically relevant squeezing. We present this value as a function of the release time. For this experiment, we use two schemes to release the atoms from the optical lattice. One scheme ramps down the optical lattice in 0.2ms (short ramp). This scheme allows maximum 4ms release time and $\sim 91\%$ coherence (constant for different release time). After that, the atom cloud expands out of the camera sensor area. The other scheme ramps down the optcial lattice adiabatically in 7ms (long ramp). This reduces the heating from the release process, thus, the atom cloud expands for longer time before hitting the limit of the camera sensor area. The release time goes up to 8ms. However, because the atoms stay in the lattice for longer, the coherence decreases to $\sim 73\%$ (constant for different release time). The data is shown in Figure 5.11. This data shows that metrologically relevant squeezing remains constant for different release time and the best value is 5.8(0.6)dB. Squeezing does not decay due to atomic expansion. The release time is only limited by the cloud expansion and the camera sensor size.

In addition, for metrological purposes, we define

$$\theta = \frac{J_z^{(2)} - J_z^{(1)}}{C(N/2)} \tag{5.4}$$

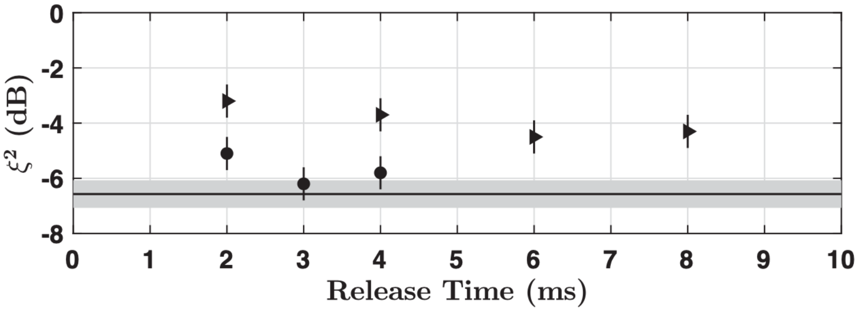

Figure 5.11: Metrologically relevant squeezing ξ^2 vs release time for both 0.2 ms (circles) and 7.0 ms (triangles) lattice release times with $N = 390000$ atoms. The mean coherence of the data sets are 0.91 ± 0.06 and 0.73 ± 0.05, respectively. Solid line: detection limit which is the same for both cases. Shaded area represents 68% confidence interval

where C is the coherence of the atoms, $J_z^{(2)}$ is the camera measured J_z, and $J_z^{(1)}$ is the cavity measured J_z. The physical meaning of θ is the angle tilted away from the equator as shown by Figure (b) in Figure 5.12. For a state near the equator, the best resolution of θ is 814(61)μrad for $390,000$ atoms (5.8(0.6)dB metrologically relevant squeezing).

5.4.3 Dynamic range

We measure the dynamic range of the camera method. The dynamic range is defined as the maximum tilting angle of the quantum state before metrologically relevant squeezing dies out. The result is shown in Figure 5.12. The dynamic range is up to $\sim$ 125mrad. This is more than 10 times the dynamic range of the cavity method. The increase in the value of $\Delta\theta$ is due to anti-squeezing. At large angles above the equator, the anti-squeezing causes a downward curvature that is projected onto J_z [70]. This data shows 36dB anti-squeezing. Since the initial squeezing verified by the cavity measurement is 14dB, this implies 12.6 times increase in the uncertainty area. The result does not preserve the uncertainty area, thus, the generation of squeezing is not unitary. The non-unitary mechanism is due to photon loss, inefficiency in extracting information from the cavity readout and additional spin-flip noise in J_z.

5.5 Fountain clock sequence below quantum projection limit

5.5.1 Protocol

We use free space Ramsey spectroscopy as the fountain clock sequence. For the spin squeezed clock, $240,000$ atoms are prepared at $J_z = 0$ state (by the microwave composite $\pi/2$ pulse and presqueezing procedure), spin squeezed (by the probe), and released into free space. While the atoms are moving

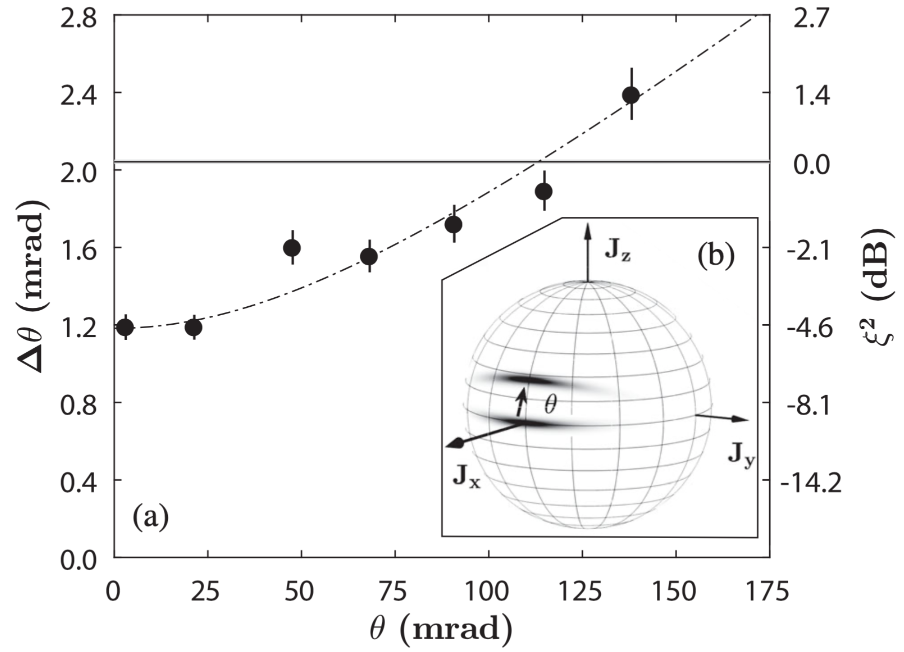

Figure 5.12: (a) Dynamic range of the camera method. It presents the angular sensitivity as a function of rotation angle for 240,000 atoms. Error bars represent 68% confidence intervals. Solid line: QPN limit, $1/\sqrt{N}$. Dashed line: fit to a squeezed state with anti-squeezing rotated on the Bloch sphere. Right size scale shows metrologically relevant squeezing. (b) Bloch sphere representation of a squeezed state tilted above the equator.

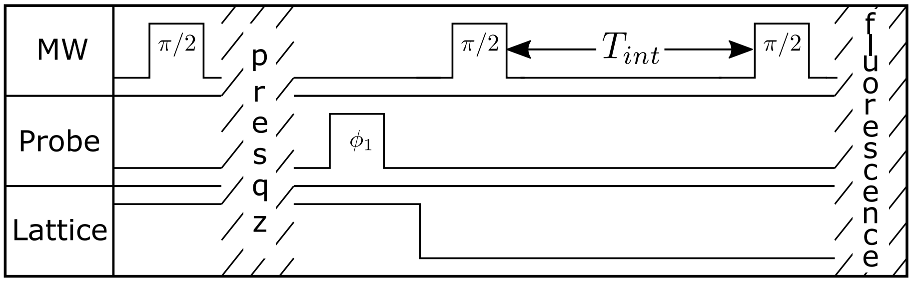

Figure 5.13: Free space Ramsey spectroscopy sequence. Spin squeezing is retrieved using the camera method. Two microwave $\pi/2$ pulses are inserted while the atoms are moving freely in space. The two pulses are separated by time T_{int}. T_{int} is called the interrogation time. The microwave sequence is called Ramsey spectroscopy.

freely in space, the two microwave $\pi/2$ pulses in Ramsey spectroscopy are inserted as shown in Figure 5.13. More details are explained in subsection 2.8.2. For the coherent state clock, the atoms are prepared at the bottom of the Bloch sphere, released, and then exposed by the two microwave pulses (see subsection 2.8.1).

5.5.2 Clock results

The performance of an atomic clock is characterized by the fractional frequency stability subsection 2.8.3. We measured the single-shot fractional frequency instability $\sigma_y(\tau = 1s)$ as a function of interrogation time T_{int}. The data is shown in Figure 5.14 (a). For an interrogation time of 3.6ms, we observe $\sigma_y(\tau = 1s) = 8.4(0.2) \times 10^{-12}$. This corresponds to 3.8(0.2)dB metrological enhancement in performance or 2.4 times reduction in averaging time. This performance is limited by the noise in the camera method and the microwave noise that runs independently of the atoms' dynamics. For $T_{int} \leq 1.3$ms, the metrological enhancement is limited by resolution of the camera method, giving 5.8dB enhancement. Furthermore, the fractional frequency stability can be averaged down while remaining below QPL as shown by Figure 5.14 (b). The ultimate resolution of the system is $\sigma_y \approx 4 \times 10^{-12}$. This is limited by the microwave amplitude and phase noise, as well as magnetic field fluctuations.

5.6 Noise Budget

The back-to-back cavity measured J_z reveals $\sim$ 14dB variance reduction, however, the camera measured J_z when correlated to the cavity measured J_z only reveals 6.6dB variance reduction. Various noise sources contribute to the uncertainty of the camera measured J_z. These are summarized in Table 5.2. The details can be found in [67, 68, 63].

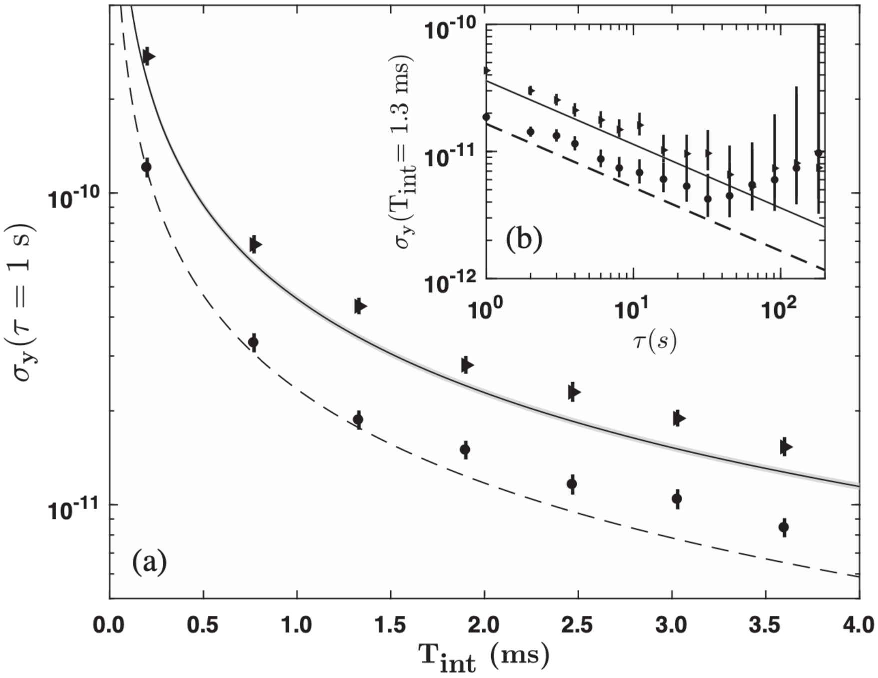

Figure 5.14: Circles: squeezed state. Triangles: CSS. All error bars represent 99% confidence intervals for visual clarity. (a) Single-shot fractional stability $\sigma_y(\tau = T_c = 1s)$ for several interrogation times T_{int} in a Ramsey spectroscopy sequence with 240000 atoms. Solid line: QPL, Equation 2.51. Dashed line: 5.8 dB SSS for reference. (b) Fractional stability for $T_{int} = 1.3$ms as a function of averaging time τ.

Source	Noise (dB)
push beam	-14
read noise & background scattered light	-14
trap inhomogeneity	-16
photon shot noise	-18
inhomogeneous photon collection efficiency	-14
total	-8

Table 5.2: Various noise sources to the uncertainty of camera measured J_z. They are represented in dB with respect to the QPL for $390,000$ atoms. The resolution of the camera method -6.6dB is a combination of the true quantum state noise ~ -14dB and ~ -8dB additional noise as shown in the table.

Chapter 6

Efforts towards Spin Squeezed Atom Interferometer

This chapter describes progress toward building a spin squeezed atom interferometer based on Raman transitions. I will first introduce the constructions for the interferometer and then analyze several factors that degrade the interferometer performance using an example of a Mach Zehnder sequence.

6.1 Experimental construction

6.1.1 Laser system

The Raman laser system is shown in Figure 6.1. The laser system starts with a 1560nm external cavity laser from RIO (RIO0165-5-01-1-H6). It has low phase noise, featuring a $\sim$ 4kHz linewidth (FWHM). Its frequency is adjustable by temperature and current tuning. Thus, we can adjust the laser detuning to minimize spontaneous emission. The output of this laser is then amplified by an Erbium-Doped Fiber Amplifier from Thorlabs (EDFA100P). After amplification, the light passes through a PPLN waveguide (NTTelectronics WH-0780-000-A-B-C) that converts 1560nm light to 780nm light through second harmonic generation (SHG). This output is then split into two paths. One is sent directly to a semiconductor optical amplifier (QPhotonics QSOAI-780PM) and we call this beam 2. The other is sent to an electro-optical modulator (Photline technologies NIR-MPX850LN10) before being sent to a semiconductor optical amplifier. We call this beam 1. The electro-optical modulator phase modulates the beam and generates multiple sidebands. On the one hand, the multiple sidebands provide us with the frequency difference we need to drive the Raman transition. On the other hand, they balance the light shift. The semiconductor optical amplifier amplifies the optical power from a few mW to tens of mW. This results in about 22mW light to

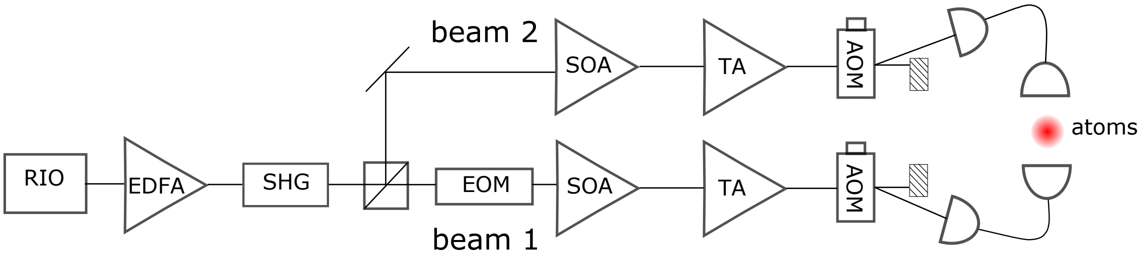

Figure 6.1: Laser system for atom interferometry. RIO: 1560nm external cavity laser; EDFA: Erbium-Doped Fiber Amplifier; SHG: frequency doubling crystal that generates 780nm light from 1560nm light; EOM: electro-optical modulator; SOA: semiconductor optical amplifier; TA: tapered amplifier; AOM: acousto-optical modulator.

inject the tapered amplifiers (Toptica photonics BoosTA pro 780) after losses along the optical paths. The Topcica TAs amplify the light to about 3W in order to give us enough power to do Raman transitions that cover the Doppler width of the atoms ($\sim$ 100KHz). Two 200MHz acoustic-optical modulators (3200-124 Gooch&Housego) are used to switch on and off the light sent to the atoms. They also offset the frequency of beam 1 and beam 2. In the end, more than 500mW optical power can be delivered to the atoms with beam size of 5.42mm $1/e^2$ beam diameter for each path. This gives more than 500kHz Rabi frequency, which ensures the coverage of the atomic Doppler width. In the end, beam 2 and the first order sideband of beam 1 serve as the two frequency components for Raman transitions. When driving Doppler sensitive transitions, the electro-optical modulator (EOM) is driven by a RF signal of frequency 6.434GHz, because opposite ordered diffracted beams from the acoustic-optical modulators (AOM) are used, giving a frequency offset of 400MHz between beam 2 and the carrier of beam 1. This scheme is used to avoid extra J_z noise due to multiple driving frequencies (see subsection 6.4.1). When driving Doppler free transitions, only the beam that passes through the EOM is turned on and the EOM driving frequency is 6.834GHz, which is the transition frequency for $|F=1, m_F=0\rangle$ and $|F=2, m_F=0\rangle$ transition.

6.1.2 Raman beam delivery system

The Raman laser beams are delivered by two Thorlabs TC25APC-780 triplet fiber collimators. The beam profile of the collimator direct output is shown in Figure 6.2. The high spatial frequency features are due to dust on the ND filter of the beam profiler. The profile has a nice Gaussian mode. After the vacuum chamber, the vacuum chamber wall introduces high frequency features and the Gaussian mode is distorted as shown in Figure 6.3.

The vacuum chamber wall not only distorts the beam profile, it also changes the polarization of the beam because of the pressure induced birefringence of the chamber wall. We examine this effect by sandwiching the vacuum chamber with two cross polarizers and examing the beam profile after each

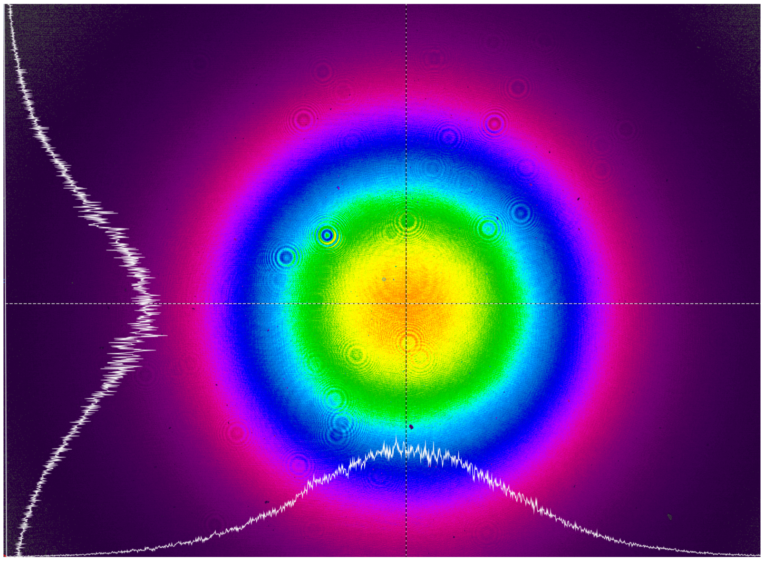

Figure 6.2: Beam profile of the laser beam that comes directly out of the triplet fiber collimator. The $1/e^2$ beam diameter is 5.42mm. The high spatial frequency features are due to the dust on the ND filter of the beam profiler rather than the beam mode.

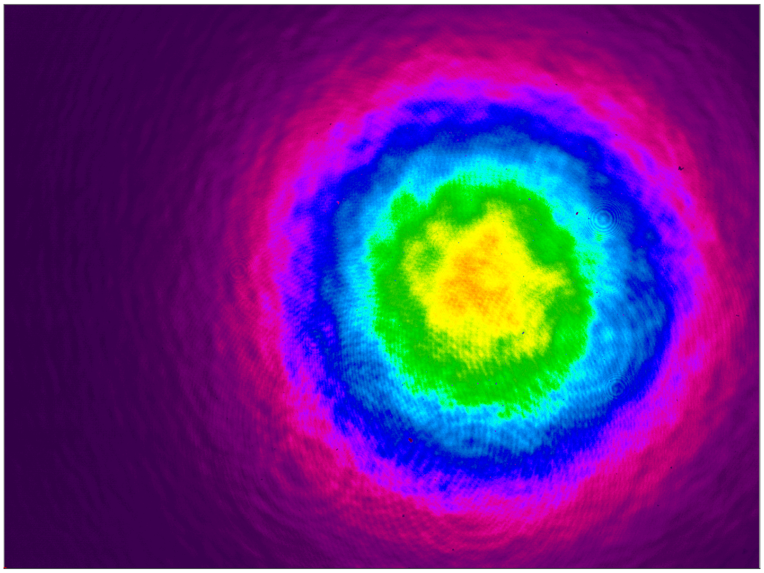

Figure 6.3: Beam profile of the laser beam after the vacuum chamber. The vacuum chamber introduces high spatial frequency features to the beam.

polarizer. We found within the resolution of this method, the vacuum chamber changes the beam polarization homogeneously. Thus, the effect of the vacuum chamber wall is modeled as an arbitrary waveplate (see Appendix B). For the Raman transition to happen between $|F=1, m_F=0\rangle$ and $|F=2, m_F=0\rangle$ states, we want the polarizations of the two beams to be cross linear or $\sigma^{+(-)}-\sigma^{+(-)}$ (see Appendix A). In our Raman beam delivery system, the beam coming out from the triplet first passes through a polarization beam splitter and then passes through a half and a quarter waveplate. The first polarization beam splitter prepares a perfectly linear polarization. The half and quarter waveplates compensate the effects from the chamber wall, preparing circularly or linearly polarized light for the atoms. Practically, we walked the half waveplate and quarter waveplate to maximize the Rabi frequency of the Doppler free Raman transition. This makes the polarization as circular as possible inside the vacuum chamber. We can also minimize the Doppler free transition to make the polarization as linear as possible. However, since it is hard to make the two linear polarizations perpendicular to each other, we choose to use the $\sigma^{+(-)}-\sigma^{+(-)}$ configuration.

6.1.3 Magnetic field

In our experiment, we only want to drive the Raman transition between $|F=1, m_F=0\rangle$ and $|F=2, m_F=0\rangle$ states. To suppress Raman transitions between other magnetic sublevels, the magnetic field direction needs to be aligned with the laser beam. This alignment is done by scanning the EOM driving frequency and minimizing the Doppler free transition peaks other than the desired one. Figure 6.4 shows the situation where the magnetic field direction is not aligned with the Raman beam. In this situation, there exists three Raman transition peaks. The center one is the desired one that corresponds to $|F=1, m_F=0\rangle$ to $|F=2, m_F=0\rangle$ transition, and the two side ones correspond to $|F=1, m_F=0\rangle$ to $|F=2, m_F=-1\rangle$ and $|F=1, m_F=0\rangle$ to $|F=2, m_F=1\rangle$ transitions. Figure 6.5 shows the situation where the magnetic field is aligned to the Raman beam. As we can see the side peaks are gone. The two small bumps next to the center peaks are result of the frequency response of a square pulse. They are suppressed when the transition is driven by a Gaussian pulse.

6.1.4 Spontaneous emission reduction

The tapered amplifier (TA) amplifies the optical signal, however, it also adds more spontaneous emission due to the amplified spontaneous emission (ASE). To reduce this effect on the atoms, we insert two Rubidium cells into the optical paths after the TAs to absorb light that is on resonance with the Rb atoms. The spontaneous emission level is measured by turning off the EOM driving signal and measuring the fractional $|\uparrow\rangle$ atom number as a function of the pulse length. Since the atoms start from $|\downarrow\rangle$ state and the Raman transition is off, the increase of $|\uparrow\rangle$ atoms is due to the spontaneous emission. The fractional $|\uparrow\rangle$ atom number is a good measure for the spontaneous emission rate. The spontaneous emission is largely reduced due to the existence of the Rb cells as

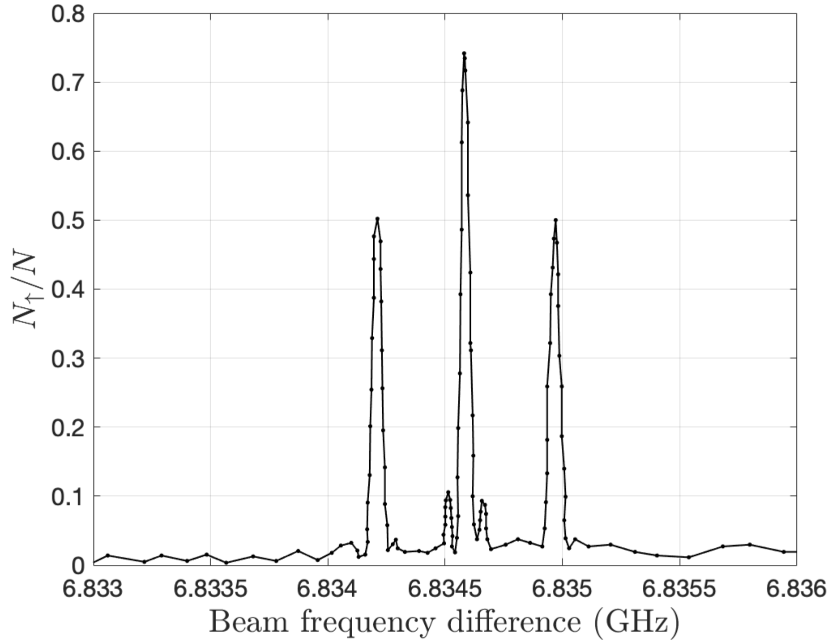

Figure 6.4: When the magnetic field is not aligned to the Raman laser beam, three Raman transition peaks exist. They correspond to $|F=1, m_F=0\rangle$ to $|F=2, m_F=-1\rangle$ transition, $|F=1, m_F=0\rangle$ to $|F=2, m_F=0\rangle$ transition, and $|F=1, m_F=0\rangle$ to $|F=2, m_F=1\rangle$ transition. The two small bumps next to the center peak are due to the frequency response of a square pulse.

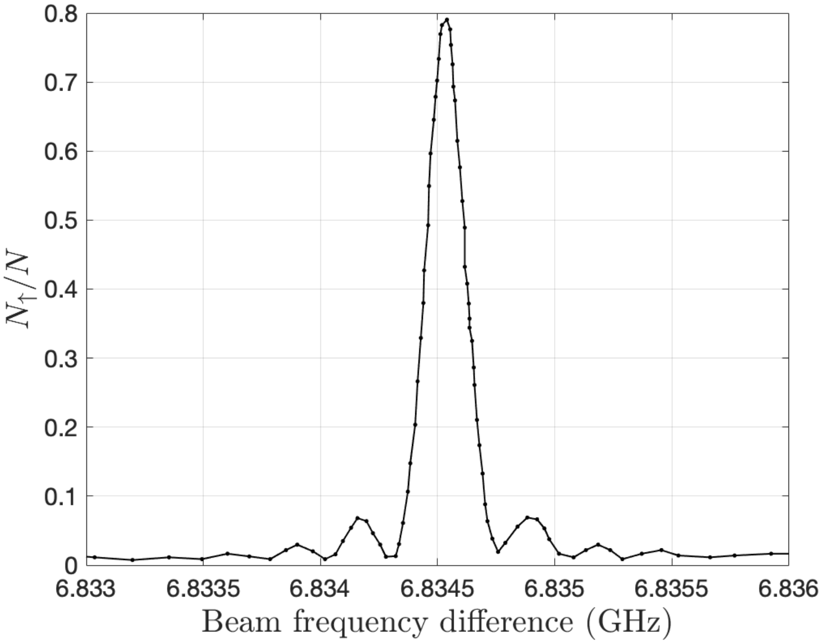

Figure 6.5: When the magnetic field is aligned to the laser beam, only the $|F = 1, m_F = 0\rangle$ to $|F = 2, m_F = 0\rangle$ transition peak exists. The small bumps next to the center peak is due to the frequency response of a square pulse.

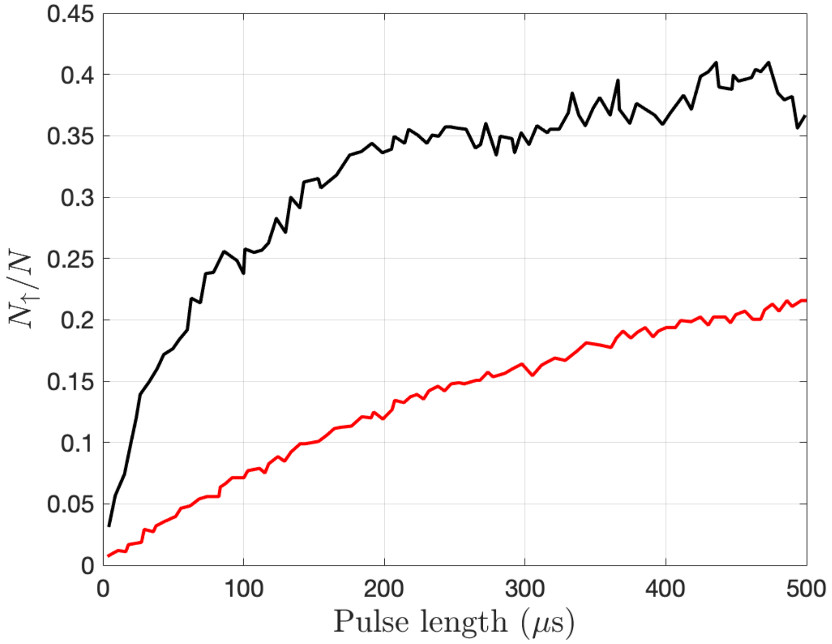

Figure 6.6: Spontaneous emission rate as a function of pulse length. Black solid line is the rate without Rb cells. Red solid line is the rate with Rb cells. The spontaneous emission rate is reduced due to the existence of Rb cells.

shown in Figure 6.6. In practice, we drive the Raman pulses of μs long. The spontaneous emission contribution is negligible in this regime.

6.2 Interferometer sequence

In order to benefit from spin squeezing, the interferometer sequence has to be first quantum projection noise limited. We run the Mach-Zehnder interferometer for coherent state and study the contrast and noise performance. The atoms are initially prepared at $|F=1, m_F=0\rangle$ state and then released into free space. While the atoms are in free space, Raman pulses are turned on to form the Mach-Zehnder sequence. Each pulse is separated by the interrogation time T (see section 2.9.4). The final J_z after interrogation is measured by the camera.

6.3 Contrast

The performance of the interferometer is tested by the contrast and J_z noise at the output port. In this section, I will study the contrast. In the next section, I will discuss the J_z noise.

6.3.1 Rabi oscillation

To maximize the contrast of the interferometer, we need to maximize the population transfer of a single Raman pulse. To do this, we optimize the alignment of the Raman beam so that the atoms are aligned to the maximum intensity of the beam, thus, the most homogeneous region for the intensity. The beam size is also chosen to be relatively large at 5.42mm compared to the atom cloud ($\sim$ 1.5mm along the cavity axis and $\sim 17\mu$m transverse to the cavity axis) to provide a relatively homogeneous intensity for the atoms. Doubling the beam size does not improve the population transfer, showing that the 5.42 mm beam diameter is not a limiting factor. The smallest possible diameter is used to maximize the light field intensity since the maximum power is limited by the optical amplifiers. A smaller beam size makes it easier to realize fast Raman transitions to cover the Doppler width of the atoms, another factor to maximize the population transfer. Another factor to increase the population transfer is to balance the AC stark shift by sending mult-sidebands to the atoms. We can balance the AC stark shift for each Raman beam. This gives maximum population transfer of 93.7% as shown by Figure 6.7. However, modulating both Raman beams introduces a position-dependent Rabi frequency subsection A.2.1. To get rid of this effect, we decide to use one modulated and one unmodulated beam. AC stark shift is balanced with both beams by adjusting their power ratio, however, individual beam is not AC stark shift balanced. The maximum population transfer in this case is 88%.

6.3.2 Cavity effect

Figure 6.8 shows the contrast as a function of the interrogation time. The data shows that the contrast decreases quickly at around 20μs interrogation time and slowly comes back. 20μs matches the photon lifetime of our optical cavity ($\tau = 1/(2\pi \cdot 8\text{KHz})$). We thus infer that the decrease of the contrast is due to the atomic interactions with some cavity modes excited by the Raman laser beams. We see that even if the contrast slowly increases when T becomes larger, it does not recover its initial value. Simply waiting for this cavity mode to die out is not enough to recover the full contrast. To get rid of this effect, we have to let the atoms free fall for longer before we turn on the Raman beams. This gives atoms enough time to fall out of the cavity mode. We measure the contrast as a function of the free fall time at $T = 25\mu$s when the cavity effect is maximized (Figure 6.9). The contrast increases with the free fall time. This effect is ruled out at 7ms free fall time as the contrast plateaus here. The atoms are now $\sim 245\mu$m away from its released location. The contrast remains constant with T at this free fall time (Figure 6.10).

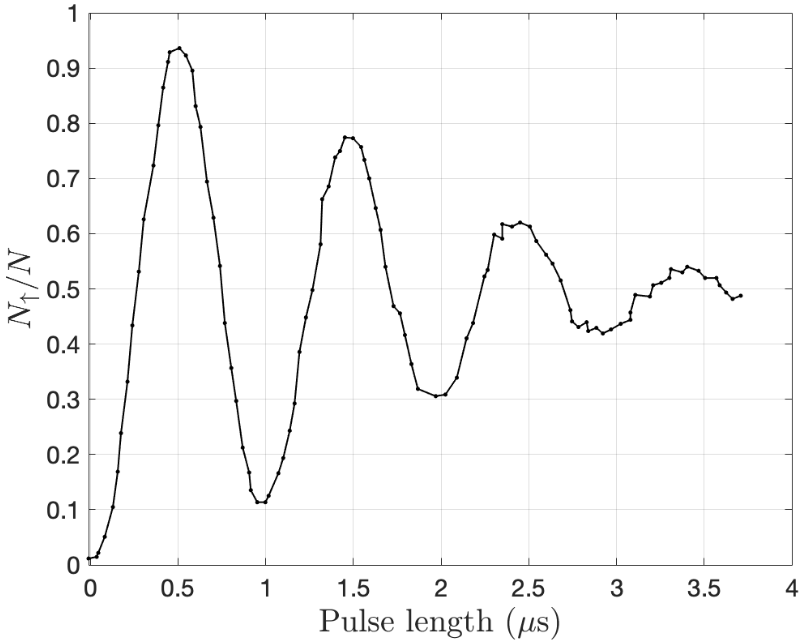

Figure 6.7: Population transfer as a function of the pulse length for Doppler sensitive Raman transitions. Each Raman beam is AC stark shift balanced. The population transfer is characterized by the fractional $|\uparrow\rangle$ atom number $N_{\uparrow}/N$. The maximum population transfer is 93.7%. The ring down is due to inhomogeneous Rabi frequencies across the atom cloud.

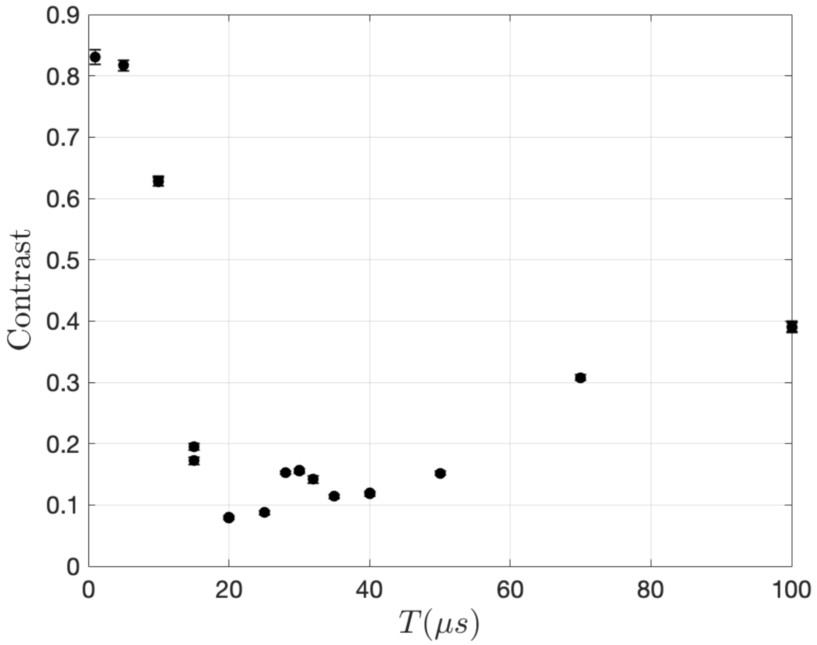

Figure 6.8: Interferometer contrast as a function of interrogation time. The atoms free fall for 0.2ms before the interferometer sequence turns on. The contrast decreases quickly at around $T = 20\mu$s interrogation time and then slowly comes back with increased T.

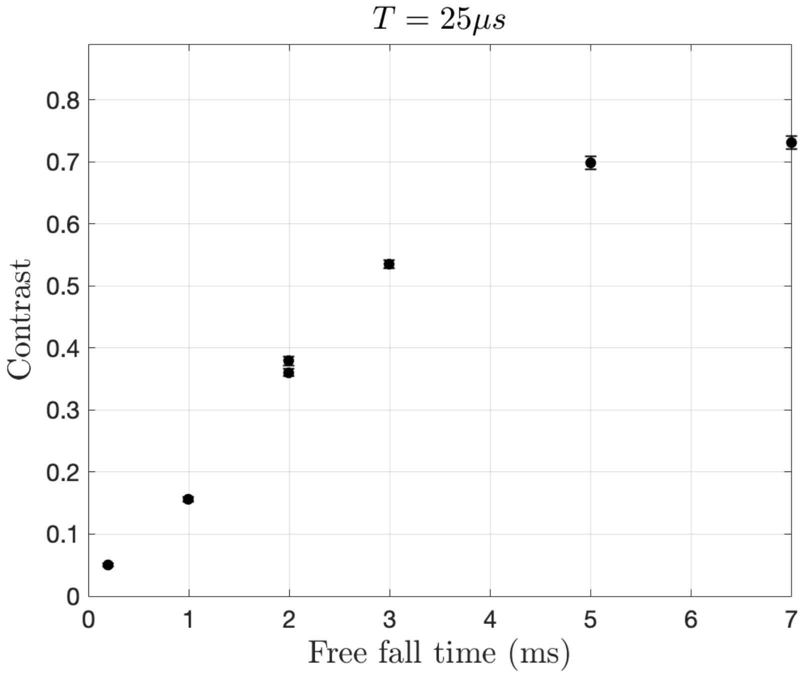

Figure 6.9: Interferometer contrast as a function of atom free fall time. The interrogation time $T = 25\mu$s. This is chosen because the cavity effect is most significant at around this interrogation time. The contrast increases with the free fall time as the atoms move farther away from the cavity modes. At 7ms, the contrast plateaus and the cavity effect is eliminated.

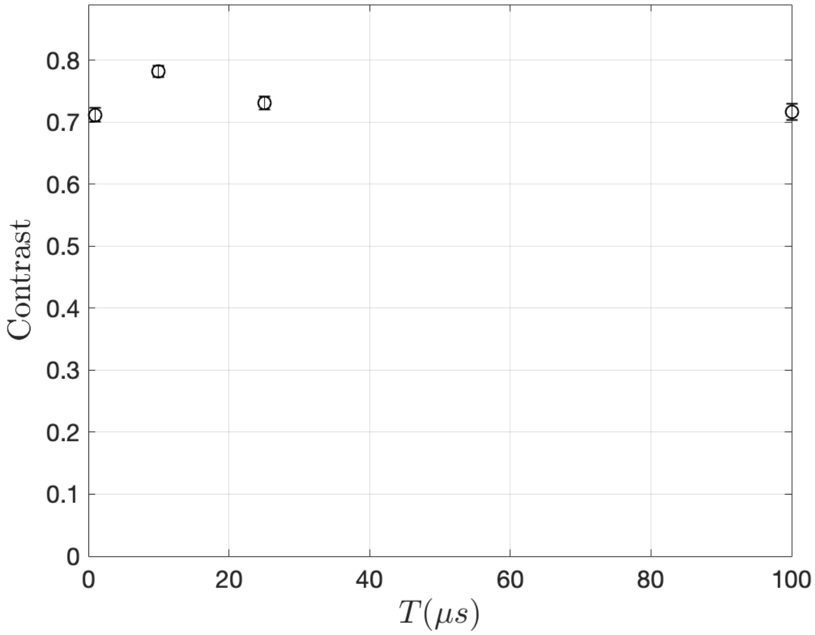

Figure 6.10: Interferometer contrast as a function of interrogation time. The free fall time of the atoms is 7ms. At this free fall time, the cavity effect is eliminated. Thus, the contrast remains constant for different interrogation times up to 100μs.

6.4 J_z noise

6.4.1 Effects from multi-sidebands

The laser spectrum seen by the atoms is shown in Figure 6.11. The solid arrows are frequency components from beam 1 in Figure 6.1. The multiple frequencies are due to the phase modulation by the EOM. We can write the electric field for the n^{th} frequency component of beam 1 as

$$E_{1,n} = E_{10} J_n(\beta) e^{i(\omega_{10}+n\omega_{EOM})t+i(n\phi_1+\phi_{10,n})} + c.c \tag{6.1}$$

where E_{10} is the electric field amplitude of beam 1 before modulation, J_n is the Bessel function, β is the modulation depth, ω_{10} is the beam 1 carrier frequency, ϕ_1 is the modulation phase, ω_{EOM} is the modulation frequency, and $\phi_{10,n}$ is the phase offset for the n^{th} frequency component. The red dashed arrow is beam 2 in Figure 6.1 and its electric field is

$$E_2 = E_{20} e^{i\omega_{20}t+\phi_{20}} + c.c \tag{6.2}$$

where E_{20}, ω_{20}, and ϕ_{20} are the electric field amplitude, frequency, and phase of beam 2. Each frequency component is circularly polarized in the same way. Thus, any pair of frequency components is able to drive Raman transitions between $|\uparrow\rangle$ and $|\downarrow\rangle$ states. Most of the combinations are detuned a few GHz away from the Raman transition and have negligible effects. These detunings are controlled by the EOM frequency. However, three combinations have detunings controlled by the AOM frequency and have the largest effects. The three combinations are: 1. the frequency components ω_{L2} and ω_{L1} that drive an on-resonance Raman transition; 2. the frequency components shown by the solid arrows that drive an off-resonance Raman transition detuned by ω_{AOM}; 3. the frequency components shown by the two red arrows that drive an off-resonance Raman transition detuned by $2\omega_{AOM}$. We measured the extra J_z/N noise above the QPL for a single π pulse as a function of the AOM frequencies. The data is shown in Figure 6.12. The effects from off-resonance Raman transitions decrease with the AOM frequency. Using the first order diffracted beam on the opposite side of the AOM, we are able to achieve an AOM frequency of 400MHz.

The effects from multi-sidebands can be described by Equation 2.35. Here, when ω_{AOM} is small, more time dependent terms remain in all four integrations in Equation 2.35. They are $\delta = 0$, $\delta = \omega_{AOM}$, and $\delta = 2\omega_{AOM}$ terms. In this case, we need to solve Equation 2.24 numerically to get a quantitative description. Meanwhile, due to the equivalence between a 3-level Raman system and a 2-level system, I will discuss a 2-level system driven by multiple frequency fields in Appendix C. This discussion provides a qualitative understanding of the 3-level case.

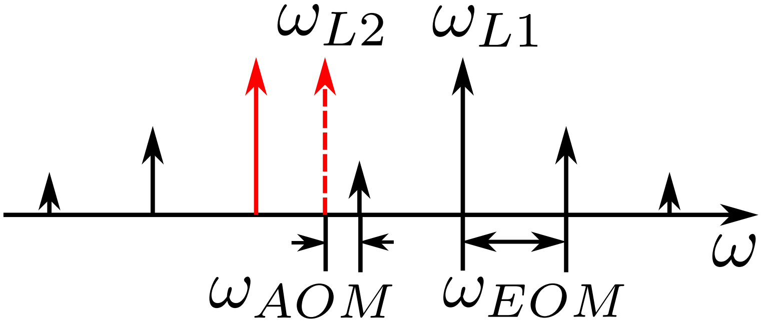

Figure 6.11: Laser spectrum for Raman transitions. The solid arrows are frequency components of beam 1 in Figure 6.1. Each frequency component is separated by an EOM frequency ω_{EOM}. Since the frequency components come from phase modulations, they are symmetric about the carrier of beam 1. The red dashed arrow is beam 2 in Figure 6.1. The frequency difference between beam 2 and the carrier of beam 1 is set by the AOM frequency ω_{AOM}. Beam 2 (ω_{L2}) and the first order sideband of beam 1 (ω_{L1}) is used to drive an on-resonance Raman transition.

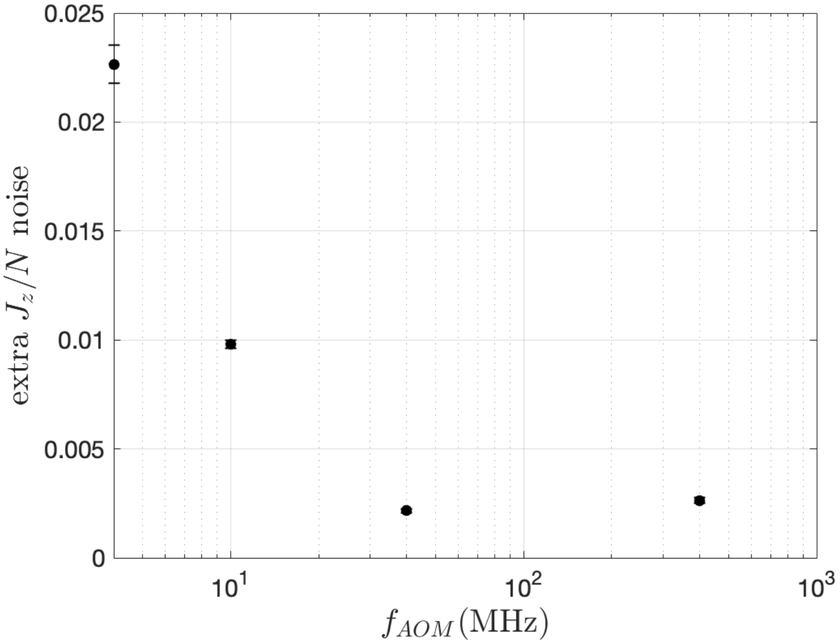

Figure 6.12: Extra J_z noise after a π pulse as a function of AOM frequency. $f_{AOM} = \omega_{AOM}/(2\pi)$. The extra J_z noise decreases with the AOM frequency and flattens when $f_{AOM} > 40$MHz. The atom number is around $200,000$ for this data set.

Pulse	Pulse area	Phase	Rotation axis tilting angle = Δ_r/Ω
Pulse1	$\frac{\pi}{2}(1+\Delta\theta_1)$	$\phi+\Delta\phi_1$	δ_1
Pulse2	$\pi(1+\Delta\theta_2)$	$\phi+\pi+\Delta\phi_2$	δ_2
Pulse3	$\frac{\pi}{2}(1+\Delta\theta_3)$	$\phi+\frac{\pi}{2}+\Delta\phi_3$	δ_3

Table 6.1: Parameters for Raman pulses in a Mach-Zehnder sequence.

6.4.2 Noise dependence on Raman transition parameters

As pointed out in subsection 2.5.1, the atomic state under Raman transitions can be viewed as Bloch vector rotations on the Bloch sphere. We use this conclusion to model the dependence of the final J_z noise on the Raman transition parameters after a Mach-Zehnder sequence. The Raman transition parameters include pulse area, phase, and detuning. They are listed in Table 6.1. Here, $\Delta\theta_i$ is the fractional pulse area fluctuation of pulse i; $\Delta\phi_i$ is the phase fluctuation of pulse i; δ_i is the rotation axis tilting angle of pulse i, and it is the ratio between detuning Δ_{ri} and Rabi frequency Ω_i of pulse i. Starting from the bottom of the Bloch sphere and after the Mach-Zehnder sequence, the final J_z normalized to the atom number becomes

$$\begin{aligned}\frac{J_z}{N} = \frac{1}{2}\{&\delta_1-\delta_3+\Delta\phi_1-2\Delta\phi_2+\Delta\phi_3\\ &+\frac{1}{4}\pi[2\delta_1\Delta\theta_1+4\delta_2(\Delta\theta_1-\Delta\theta_2)-2\delta_3\Delta\theta_3+\pi(\Delta\theta_1-2\Delta\theta_2)\Delta\theta_3]\}.\end{aligned} \tag{6.3}$$

Based on this equation, the final J_z noise depends on the phase noise and the rotation axis tilting angle, i.e. detuning Rabi frequency ratio, on the first order.

In our experiment, the Raman transition is tuned on resonance on average, i.e. $\bar{\Delta}_r = 0$. Thus, the δ fluctuation mostly comes from the Δ_r fluctuation. The Ω fluctuation is a second order effect on δ fluctuation. We examine the detuning fluctuation Δ_r. The detuning comes from differential AC stark shifts and laser frequency difference. The laser frequency difference is controlled by the microwave that modulates the EOM and thus is relatively stable. The differential AC stark shift contributes most of the detuning fluctuations. In our experiment the equation to calculate the differential AC stark shift is

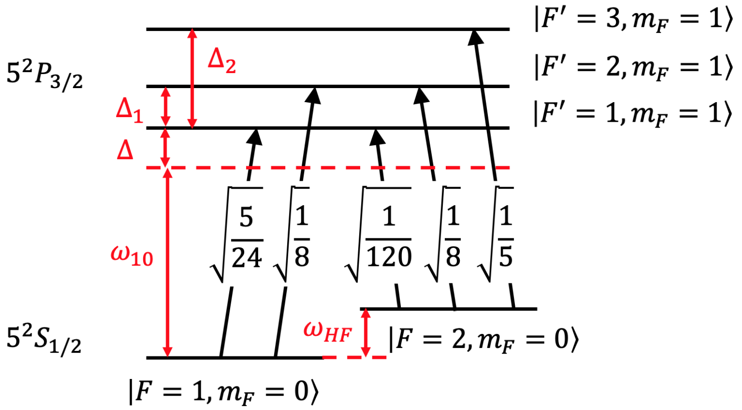

Figure 6.13: The relevant energy levels of ^{87}Rb atoms and laser detunings for the calculation of AC stark shift in our experiment. ω_{10} is the carrier frequency of beam 1. Each number with an black arrow stands for the hyperfine dipole matrix element expressed as multiples of $\langle J=1/2||er||J'=3/2\rangle$.

$$
\begin{aligned}
\Delta E_{|F=1,m_F=0\rangle\rightarrow|F=2,m_F=0\rangle} = \frac{\langle J'=\frac{3}{2}||er||J=\frac{1}{2}\rangle^2}{\hbar^2}&[\sum_n E_n^2(\frac{5/24}{\Delta-n\omega_{EOM}}+\frac{1/8}{\Delta+\Delta_1-n\omega_{EOM}}) \\
&+E_{20}^2(\frac{5/24}{\Delta+\omega_{AOM}}+\frac{1/8}{\Delta+\Delta_1+\omega_{AOM}}) \\
-\sum_n E_n^2(\frac{1/120}{\Delta-\omega_{HF}-n\omega_{EOM}}&+\frac{1/8}{\Delta-\omega_{HF}-n\omega_{EOM}+\Delta_1}+\frac{1/5}{\Delta-\omega_{HF}-n\omega_{EOM}+\Delta_2}) \\
-E_{20}^2(\frac{1/120}{\Delta-\omega_{HF}+\omega_{AOM}}&+\frac{1/8}{\Delta-\omega_{HF}+\omega_{AOM}+\Delta_1}+\frac{1/5}{\Delta-\omega_{HF}+\omega_{AOM}+\Delta_2})] \qquad (6.4)
\end{aligned}
$$

where $E_n=E_{10}J_n(\beta)$ is the electric field amplitude of the n^{th} frequency component of beam 1, ω_{HF} is the transition frequency between $|\uparrow\rangle$ and $|\downarrow\rangle$ states, Δ is the frequency difference between the $|F=1,m_F=0\rangle$ to $|F'=1,m_F=1\rangle$ transition and the carrier of beam 1, $\Delta_1=2\pi\cdot 156.9$MHz, and $\Delta_2=2\pi\cdot 423.6$MHz. This equation is from mapping Equation 2.36 to the Rb atoms. The relevant energy levels and laser detunings are shown in Figure 6.13. According to this equation, we see that the laser power fluctuations, laser frequency fluctuations, and modulation depth fluctuations all contribute to the detuning fluctuations due to the AC stark shift.

This detuning fluctuation is mostly reflected in a Doppler free sequence where the atoms start at $J_z=0$ state, and then two Raman π pulses are applied with a π phase shift between them. We notice that the final J_z noise for this sequence is maximized when the first π pulse is aligned with the atoms ($\pi_0-\pi_{180^\circ}$ sequence), while minimized when the first π pulse is 90° from the atoms

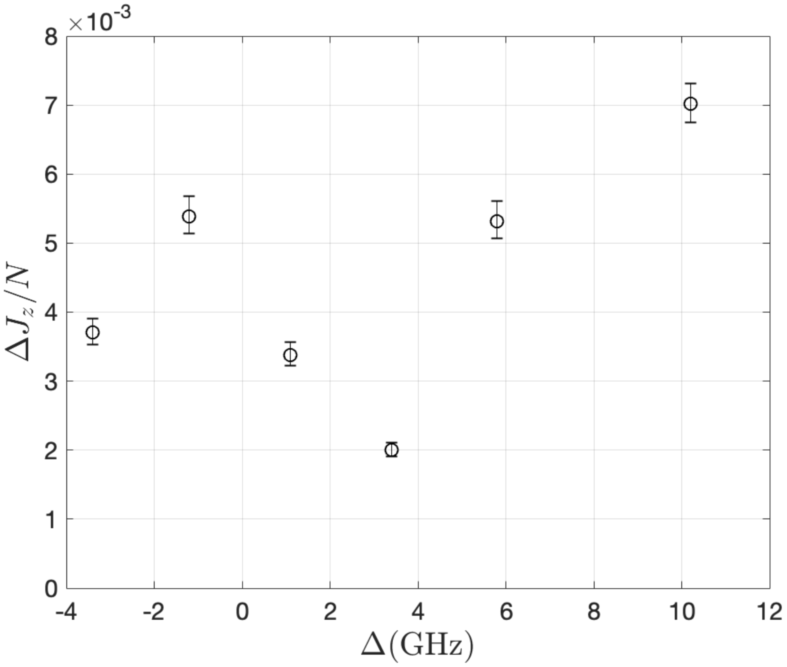

Figure 6.14: Normalized J_z noise after a Mach-Zehnder sequence as a function of the single beam detuning Δ. $T = 50\mu$s for the sequence. The detuning is measured relative to the frequency of the push beam. The noise does not depend on the detuning monotonically because of the complications from multiple laser frequencies. The atom number is around $250,000$ for this data set.

($\pi_{90^\circ} - \pi_{270^\circ}$ sequence). $\pi_{90^\circ} - \pi_{270^\circ}$ sequence is sensitive to pulse area fluctuations but insensitive to detuning fluctuations, while $\pi_0 - \pi_{180^\circ}$ sequence is sensitive to detuning fluctuations but insensitive to pulse area fluctuations. The detuning fluctuation outweighs pulse area fluctuations.

6.4.3 Effects from laser detuning

Another factor that affects the final J_z noise is the single photon laser detuning Δ (shown in Figure 6.13). The detuning affects the level of spontaneous emission, which contributes to J_z noise. We measure the J_z noise for different detunings (Figure 6.14). The J_z noise does not depend on the detuning monotonically. This is because we drive the Raman transition with multiple frequency components. The increase in detuning for a single frequency component will decrease the detunings for other frequency components and vice versa. Their effects compensate each other and lead to a detuning value that minimizes J_z noise. In addition, the detuning also affects noise in AC stark shift balancing, which contributes to the final J_z noise.

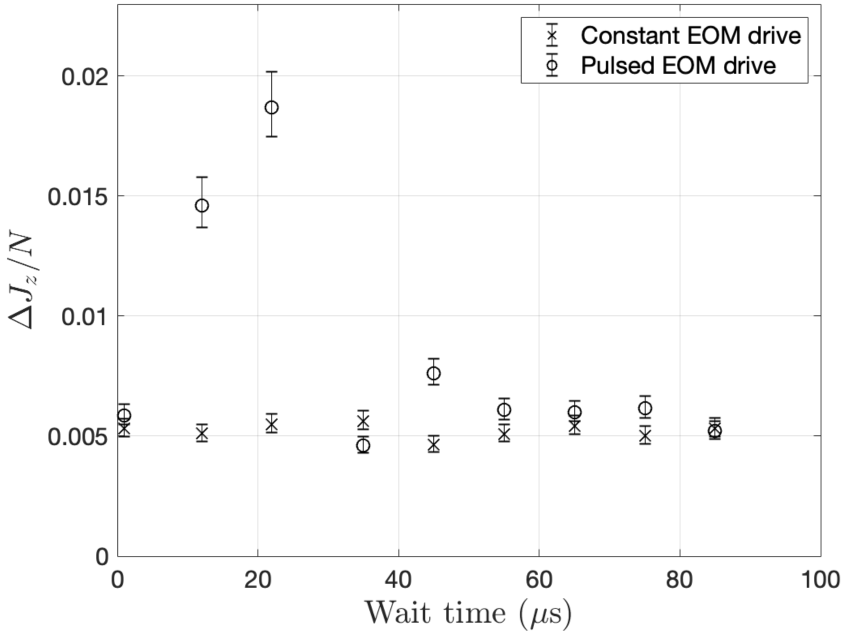

Figure 6.15: An EOM transient effect on the normalized J_z noise after a Mach-Zehnder sequence. $T = 100\mu$s for this data. The wait time is the time between the EOM driving signal on (when pulsed) and the Raman beam on. The transient is suppressed when we drive the EOM with a constant RF signal. The atom number is around $100,000$ for this data set.

6.4.4 Effects from EOM

In our experiment, an EOM is used to generate the frequency difference between two Raman beams. It imprints the 6.834GHz microwave frequency to the optical domain. Ideally, this imprint maintains the good properties of the microwave signal. However, due to imperfections of the EOM, extra noise is introduced to the optical domain. We find that when the EOM is driven by microwave pulses, depending on when we turn on the Raman beams with repsect to these pulses, the J_z noise increases significantly (Figure 6.15). When the EOM is driven by a constant microwave signal, this effect is suppressed. We attribute this phenomenon to the EOM thermal effects [71]. The microwave signal sent to the EOM heats up the crystal of the EOM and changes its modulation index. This introduces extra noise to the final J_z.

6.4.5 Laser phase noise

The phase noise comes from the relative phase jitter between frequency component ω_{L2} and ω_{L1} of the laser spectrum Figure 6.11. In the design of our laser system, even if these two frequency components are from the same seed, the optical amplifications and modulations along the path

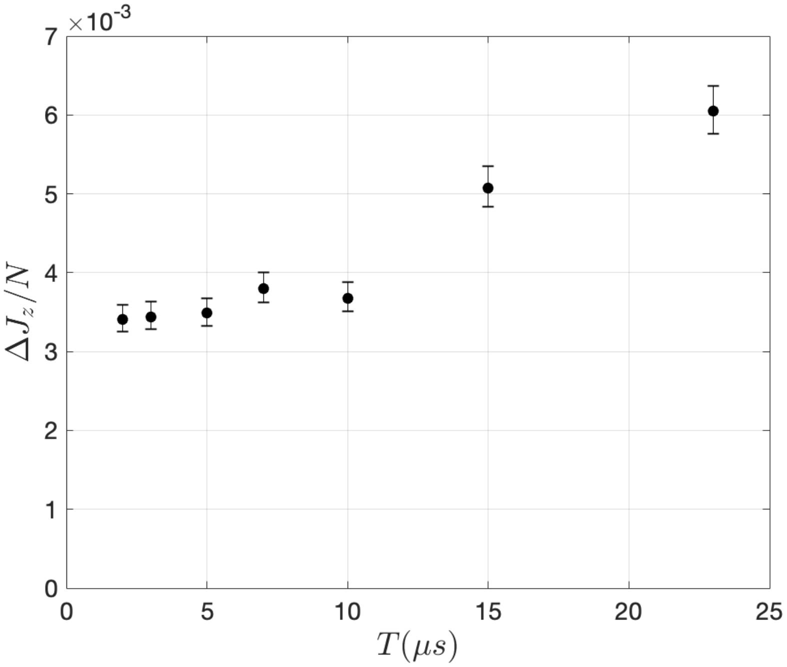

Figure 6.16: Normalized J_z noise after a Mach-Zehnder sequence as a function of interrogation time T. The increase in noise with a larger T is due to the mixing of more low frequency phase noise.

introduce extra phase jitters, increasing the laser phase noise. We measured the final J_z noise after a Mach-Zehnder sequence as a function of interrogation time T as shown in Figure 6.16. When T is larger, the interferometer sequence sees more low frequency phase noise, thus increasing final J_z noise. The Rabi frequency is larger than 500kHz, resulting in the pulse length less than 1μs. This means high frequency phase noise up to 1MHz is mixed into the final J_z noise. This measurement is done with $N \sim 300,000$ atoms. The QPL is $\sim 10^{-3} = 1/(2\sqrt{N})$. The minimum J_z noise from our data is more than 3 times the QPL. This implies the need to suppress laser phase noise.

6.4.6 Noise due to optical components

In our experiment, we use fibers to transmit light from the TA to the atoms. The fiber can introduce additive phase noise due to thermodynamic fluctuations, chromatic dispersion, double scattering from discrete points, and double Rayleigh scattering [72]. We found no difference in final J_z noise when comparing the results with light sent to the atoms through free space and with light sent to the atoms through fibers. This means this additive phase noise due to fibers is relatively small.

Besides noise due to double scattering from discrete points in fibers, other optical components can also double reflect light and form etalons. This effect introduces extra intensity and phase fluctuations [73]. We reduce this effect by tilting all the optical components by an angle and use anti-reflection coatings. When an etalon is formed, tapping the relating optics will change the transmitted optical power significantly. We did not observe this effect during our constructions.

Chapter 7

Conclusions and future work

The work in this thesis provides evidence for utilizing cavity generated spin squeezing in free space atomic sensors. The cavity method provides a high level of squeezing for short release time. Thus, it is suitable for sensors that require high bandwidth readout. To reduce squeezing degradation and increase the release time, more complicated lattice release-recapture sequences can be explored. The model we developed to explain squeezing degradation demonstrates the importance of maintaining homogeneous atom-cavity coupling. This model works to explain not only the atom-cavity coupling inhomogeneity but also other inhomogeneous scenarios, and is generally applicable.

The camera method maintains constant levels of squeezing with maximum release time of 8ms and is only limited by the camera sensor size and cloud expansion. The release can be extended to much longer times with colder atom clouds and bigger camera sensors. Various sources that contribute to the camera J_z noise are explored and suppressed. The most significant contributions come from the push beam, read noise, background scattered light and inhomogeneous photon collection efficiency. Further improvement can be made with a higher quantum efficiency camera, a well designed vacuum chamber to reduce background scattering, easier camera access, and a larger objective lens to allow higher and more homogeneous photon collection efficiency. Using this camera method, a spin squeezed fountain clock sequence was implemented. A clock enhancement of 5.8dB below QPL is achieved when $T_{int} \leq 1.3$ms, limited by the resolution of fluorescence imaging. This is a proof of principle demonstration of a squeezing-enhanced free space atomic sensor. Although the current fractional stability is limited to 4×10^{-12} ($\tau \sim 40$s), we expect the clock sequence to reach lower fractional frequency stability with better engineering such as magnetic field shielding and lower phase noise microwave source.

Even if squeezing survives with microwave interactions in the clock demonstration, it is harder to maintain squeezing after laser interactions as in the application of atom interferometry. The laser interaction brings us a few additional challenges: 1. We need high-power optical beams with low relative laser phase noise, meaning we need to imprint the low phase noise microwave signal to the optical domain with high fidelity and we need to suppress the large amount of ASE due to laser amplifications. 2. Laser interactions induce light shift on atoms, resulting in extra detuning noise that we need to take care of. 3. Laser interactions introduce spontaneous emission; even if we decrease this effect by choosing an appropriate single photon detuning, this effect still adds extra noise. 4. When using lasers, we need to optimize the beam wavefronts and spatial modes, another layer of complications. 5. Atomic motion comes into play, affecting the interaction homogeneity. In our exploration, we realize a Mach-Zehnder interferometer with noise 3 times above the quantum projection limit. Therefore, we are not at the stage to see enhancement from spin squeezing yet.

Currently, the application of spin squeezing to atom interferometry is limited by the laser phase noise and possibly the detuning noise. To reduce the detuning noise, we need better control over AC stark shift balancing. To reduce laser phase noise, on the one hand, we can decrease the atomic temperature. Thus, we can drive the Raman transition with lower Rabi frequency, decreasing the high frequency phase noise. The reduced Rabi frequency also simplifies the procedure to phase lock two lasers. Phase locking two lasers gets rid of the use of EOM. This eliminates phase noise due to EOM imperfections such as thermal effects. On the other hand, we can take a differential measurement scheme, where we build two atom interferometers interrogated by the same laser beams. In this case, the laser noise becomes a common mode and does not contribute to the differential readout.

Appendix A

Raman transition for ^{87}Rb D_2 line

A.1 Raman transition driven by two frequency components

For Raman transitions between the two magnetically insensitive hyperfine splittings of the ^{87}Rb ground states $|F=2, m_F=0\rangle \rightarrow |F=1, m_F=0\rangle$ utilizing the D_2 line, we discuss four polarization configurations of the driving E&M fields. They are circular-circular ($\sigma_{+(-)} - \sigma_{+(-)}$), cross linear ($\vec{\epsilon_1} \perp \vec{\epsilon_2}$), linear-linear ($\vec{\epsilon_1} \parallel \vec{\epsilon_2}$), and $\pi-\pi$ polarizations. For the first three configurations, the B field is aligned to the $\vec{k}$ of the E&M fields. For the last configuration, the B field is aligned to the electric field of the E&M fields. Based on the hyperfine dipole matrix elements shown in Figure A.1 [74], $\pi-\pi$ polarization does not cause Raman transitions, because there is no common excited state that connects the two hyperfine ground states. The hyperfine dipole matrix elements for circular-circular, cross linear, and linear-linear polarizations are shown in Figure A.2 [74].

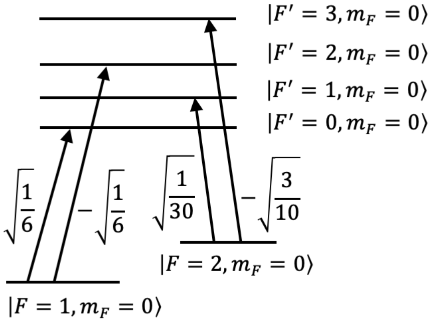

Figure A.1: ^{87}Rb D_2 line ($5^2S_{1/2}$ to $5^2P_{3/2}$ transition) hyperfine dipole matrix elements for π transition, expressed as multiples of $\langle J=1||er||J'=3/2\rangle$.

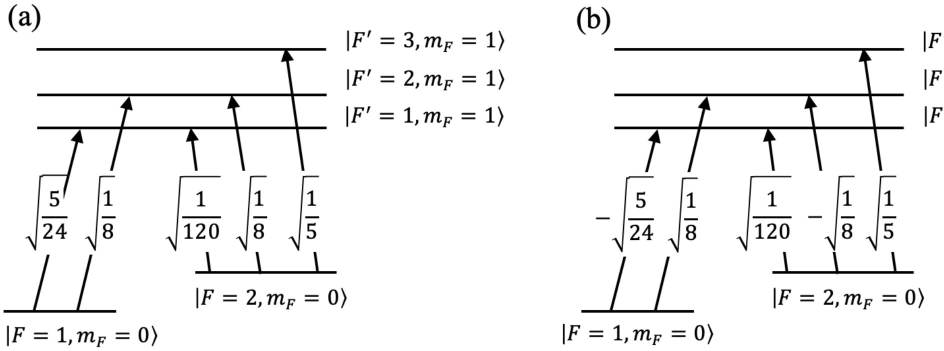

Figure A.2: ^{87}Rb D_2 line ($5^2S_{1/2}$ to $5^2P_{3/2}$ transition) hyperfine dipole matrix elements for σ_+ transition (a) and for σ_- transition (b), expressed as multiples of $\langle J = 1||er||J' = 3/2\rangle$.

Since there are multiple excited states, we take the equations from subsection 2.5.2 for circular-circular, cross linear, and linear-linear polarizations. We define $|a\rangle = |F = 1, m_F = 0\rangle$, $|b\rangle = |F = 2, m_F = 0\rangle$, $|c_1\rangle = |F' = 1, m_F = 1\rangle$, $|c_2\rangle = |F' = 2, m_F = 1\rangle$, $|c_3\rangle = |F' = 3, m_F = 1\rangle$, $|c_4\rangle = |F' = 1, m_F = -1\rangle$, $|c_5\rangle = |F' = 2, m_F = -1\rangle$, $|c_6\rangle = |F' = 3, m_F = -1\rangle$.

A.1.1 Circular-circular polarization

Assume the circular polarization is σ_+ (same result for σ_- polarization). This means $\vec{\epsilon_1} = \vec{\epsilon_2} = -\frac{\hat{e_x}+i\hat{e_y}}{\sqrt{2}}$. Using the tensor operator expression and Wigner-Eckart Theorem, the matrix elements for the transition Hamiltonian are

$$\begin{aligned}
\tilde{V}_{ac_k} &= C_{\sigma_+}^{a,c_k}\frac{\langle J||er||J'\rangle E_1}{\hbar}\cos(\omega_1 t+\phi_1) + C_{\sigma_+}^{a,c_k}\frac{\langle J||er||J'\rangle E_2}{\hbar}\cos(\omega_2 t+\phi_2)\\
\tilde{V}_{c_k a} &= C_{\sigma_+}^{c_k,a}\frac{\langle J'||er||J\rangle E_1}{\hbar}\cos(\omega_1 t+\phi_1) + C_{\sigma_+}^{c_k,a}\frac{\langle J'||er||J\rangle E_2}{\hbar}\cos(\omega_2 t+\phi_2)\\
\tilde{V}_{bc_k} &= C_{\sigma_+}^{b,c_k}\frac{\langle J||er||J'\rangle E_1}{\hbar}\cos(\omega_1 t+\phi_1) + C_{\sigma_+}^{b,c_k}\frac{\langle J||er||J'\rangle E_2}{\hbar}\cos(\omega_2 t+\phi_2)\\
\tilde{V}_{c_k b} &= C_{\sigma_+}^{c_k,b}\frac{\langle J'||er||J\rangle E_1}{\hbar}\cos(\omega_1 t+\phi_1) + C_{\sigma_+}^{c_k,b}\frac{\langle J'||er||J\rangle E_2}{\hbar}\cos(\omega_2 t+\phi_2)
\end{aligned} \tag{A.1}$$

where $C_{\sigma_+}^{i,j}$ are values taken from Figure A.2 (a) for the corresponding states. These result in:

$$\begin{aligned}
\tilde{V}_{ac_1} &= \sqrt{\frac{5}{24}}[\Omega_1\cos(\omega_1 t+\phi_1)+\Omega_2\cos(\omega_2 t+\phi_2)]\\
\tilde{V}_{c_1a} &= \sqrt{\frac{5}{24}}[\Omega_1^*\cos(\omega_1 t+\phi_1)+\Omega_2^*\cos(\omega_2 t+\phi_2)]\\
\tilde{V}_{ac_2} &= \sqrt{\frac{1}{8}}[\Omega_1\cos(\omega_1 t+\phi_1)+\Omega_2\cos(\omega_2 t+\phi_2)]\\
\tilde{V}_{c_2a} &= \sqrt{\frac{1}{8}}[\Omega_1^*\cos(\omega_1 t+\phi_1)+\Omega_2^*\cos(\omega_2 t+\phi_2)]\\
\tilde{V}_{ac_3} &= \tilde{V}_{c_3a} = 0\\
\tilde{V}_{ac_4} &= \tilde{V}_{c_4a} = 0\\
\tilde{V}_{ac_5} &= \tilde{V}_{c_5a} = 0\\
\tilde{V}_{ac_6} &= \tilde{V}_{c_6a} = 0\\
\tilde{V}_{bc_1} &= \sqrt{\frac{1}{120}}[\Omega_1\cos(\omega_1 t+\phi_1)+\Omega_2\cos(\omega_2 t+\phi_2)]\\
\tilde{V}_{c_1b} &= \sqrt{\frac{1}{120}}[\Omega_1^*\cos(\omega_1 t+\phi_1)+\Omega_2^*\cos(\omega_2 t+\phi_2)]\\
\tilde{V}_{bc_2} &= \sqrt{\frac{1}{8}}[\Omega_1\cos(\omega_1 t+\phi_1)+\Omega_2\cos(\omega_2 t+\phi_2)]\\
\tilde{V}_{c_2b} &= \sqrt{\frac{1}{8}}[\Omega_1^*\cos(\omega_1 t+\phi_1)+\Omega_2^*\cos(\omega_2 t+\phi_2)]\\
\tilde{V}_{bc_3} &= \sqrt{\frac{1}{5}}[\Omega_1\cos(\omega_1 t+\phi_1)+\Omega_2\cos(\omega_2 t+\phi_2)]\\
\tilde{V}_{c_3b} &= \sqrt{\frac{1}{5}}[\Omega_1^*\cos(\omega_1 t+\phi_1)+\Omega_2^*\cos(\omega_2 t+\phi_2)]\\
\tilde{V}_{bc_4} &= \tilde{V}_{c_4b} = 0\\
\tilde{V}_{bc_5} &= \tilde{V}_{c_5b} = 0\\
\tilde{V}_{bc_6} &= \tilde{V}_{c_6b} = 0
\end{aligned} \tag{A.2}$$

where $\Omega_1 = \frac{\langle J'=\frac{3}{2}||er||J=\frac{1}{2}\rangle E_1}{\hbar}$ and $\Omega_2 = \frac{\langle J'=\frac{3}{2}||er||J=\frac{1}{2}\rangle E_2}{\hbar}$. Assuming the energy differences between hyperfine excited states are small compared to the single photon detuning Δ, this yields Rabi frequency of $\frac{1}{6}\frac{\Omega_1\Omega_2}{2\Delta}$.

A.1.2 Cross linear polarization

Linear polarization is a superposition of right and left circular light. For cross linear polarizations, i.e. $\vec{\epsilon_1} \perp \vec{\epsilon_2}$, we write $\vec{\epsilon_1} = \frac{1}{\sqrt{2}}(\frac{\hat{e_x}-i\hat{e_y}}{\sqrt{2}} - \frac{\hat{e_x}+i\hat{e_y}}{\sqrt{2}})$ and $\vec{\epsilon_2} = \frac{1}{\sqrt{2}}(\frac{\hat{e_x}-i\hat{e_y}}{\sqrt{2}} + \frac{\hat{e_x}+i\hat{e_y}}{\sqrt{2}})$. Thus the matrix elements become:

$$\begin{aligned}
\tilde{V}_{ac_k} &= (C^{a,c_k}_{\sigma_-} + C^{a,c_k}_{\sigma_+})\frac{\langle J||er||J'\rangle E_1}{\sqrt{2}\hbar}\cos(\omega_1 t + \phi_1) + (C^{a,c_k}_{\sigma_-} - C^{a,c_k}_{\sigma_+})\frac{\langle J||er||J'\rangle E_2}{\sqrt{2}\hbar}\cos(\omega_2 t + \phi_2) \\
\tilde{V}_{c_k a} &= (C^{c_k,a}_{\sigma_-} + C^{c_k,a}_{\sigma_+})\frac{\langle J'||er||J\rangle E_1}{\sqrt{2}\hbar}\cos(\omega_1 t + \phi_1) + (C^{c_k,a}_{\sigma_-} - C^{c_k,a}_{\sigma_+})\frac{\langle J'||er||J\rangle E_2}{\sqrt{2}\hbar}\cos(\omega_2 t + \phi_2) \\
\tilde{V}_{bc_k} &= (C^{b,c_k}_{\sigma_-} + C^{b,c_k}_{\sigma_+})\frac{\langle J||er||J'\rangle E_1}{\sqrt{2}\hbar}\cos(\omega_1 t + \phi_1) + (C^{b,c_k}_{\sigma_-} - C^{b,c_k}_{\sigma_+})\frac{\langle J||er||J'\rangle E_2}{\sqrt{2}\hbar}\cos(\omega_2 t + \phi_2) \\
\tilde{V}_{c_k b} &= (C^{c_k,b}_{\sigma_-} + C^{c_k,b}_{\sigma_+})\frac{\langle J'||er||J\rangle E_1}{\sqrt{2}\hbar}\cos(\omega_1 t + \phi_1) + (C^{c_k,b}_{\sigma_-} - C^{c_k,b}_{\sigma_+})\frac{\langle J'||er||J\rangle E_2}{\sqrt{2}\hbar}\cos(\omega_2 t + \phi_2).
\end{aligned} \tag{A.3}$$

These result in:

$$
\begin{aligned}
\tilde{V_{ac_1}} &= \frac{1}{\sqrt{2}}\sqrt{\frac{5}{24}}\Omega_1\cos(\omega_1 t+\phi_1) - \frac{1}{\sqrt{2}}\sqrt{\frac{5}{24}}\Omega_2\cos(\omega_2 t+\phi_2)\\
\tilde{V_{c_1a}} &= \frac{1}{\sqrt{2}}\sqrt{\frac{5}{24}}\Omega_1^*\cos(\omega_1 t+\phi_1) - \frac{1}{\sqrt{2}}\sqrt{\frac{5}{24}}\Omega_2^*\cos(\omega_2 t+\phi_2)\\
\tilde{V_{ac_2}} &= \frac{1}{\sqrt{2}}\sqrt{\frac{1}{8}}\Omega_1\cos(\omega_1 t+\phi_1) - \frac{1}{\sqrt{2}}\sqrt{\frac{1}{8}}\Omega_2\cos(\omega_2 t+\phi_2)\\
\tilde{V_{c_2a}} &= \frac{1}{\sqrt{2}}\sqrt{\frac{1}{8}}\Omega_1^*\cos(\omega_1 t+\phi_1) - \frac{1}{\sqrt{2}}\sqrt{\frac{1}{8}}\Omega_2^*\cos(\omega_2 t+\phi_2)\\
\tilde{V_{ac_3}} &= \tilde{V_{c_3a}} = 0\\
\tilde{V_{ac_4}} &= -\frac{1}{\sqrt{2}}\sqrt{\frac{5}{24}}\Omega_1\cos(\omega_1 t+\phi_1) - \frac{1}{\sqrt{2}}\sqrt{\frac{5}{24}}\Omega_2\cos(\omega_2 t+\phi_2)\\
\tilde{V_{c_4a}} &= -\frac{1}{\sqrt{2}}\sqrt{\frac{5}{24}}\Omega_1^*\cos(\omega_1 t+\phi_1) - \frac{1}{\sqrt{2}}\sqrt{\frac{5}{24}}\Omega_2^*\cos(\omega_2 t+\phi_2)\\
\tilde{V_{ac_5}} &= \frac{1}{\sqrt{2}}\sqrt{\frac{1}{8}}\Omega_1\cos(\omega_1 t+\phi_1) + \frac{1}{\sqrt{2}}\sqrt{\frac{1}{8}}\Omega_2\cos(\omega_2 t+\phi_2)\\
\tilde{V_{c_5a}} &= \frac{1}{\sqrt{2}}\sqrt{\frac{1}{8}}\Omega_1^*\cos(\omega_1 t+\phi_1) + \frac{1}{\sqrt{2}}\sqrt{\frac{1}{8}}\Omega_2^*\cos(\omega_2 t+\phi_2)\\
\tilde{V_{ac_6}} &= \tilde{V_{c_6a}} = 0\\
\tilde{V_{bc_1}} &= \frac{1}{\sqrt{2}}\sqrt{\frac{1}{120}}\Omega_1\cos(\omega_1 t+\phi_1) - \frac{1}{\sqrt{2}}\sqrt{\frac{1}{120}}\Omega_2\cos(\omega_2 t+\phi_2)\\
\tilde{V_{c_1b}} &= \frac{1}{\sqrt{2}}\sqrt{\frac{1}{120}}\Omega_1^*\cos(\omega_1 t+\phi_1) - \frac{1}{\sqrt{2}}\sqrt{\frac{1}{120}}\Omega_2^*\cos(\omega_2 t+\phi_2)\\
\tilde{V_{bc_2}} &= \frac{1}{\sqrt{2}}\sqrt{\frac{1}{8}}\Omega_1\cos(\omega_1 t+\phi_1) - \frac{1}{\sqrt{2}}\sqrt{\frac{1}{8}}\Omega_2\cos(\omega_2 t+\phi_2)\\
\tilde{V_{c_2b}} &= \frac{1}{\sqrt{2}}\sqrt{\frac{1}{8}}\Omega_1^*\cos(\omega_1 t+\phi_1) - \frac{1}{\sqrt{2}}\sqrt{\frac{1}{8}}\Omega_2^*\cos(\omega_2 t+\phi_2)\\
\tilde{V_{bc_3}} &= \frac{1}{\sqrt{2}}\sqrt{\frac{1}{5}}\Omega_1\cos(\omega_1 t+\phi_1) - \frac{1}{\sqrt{2}}\sqrt{\frac{1}{5}}\Omega_2\cos(\omega_2 t+\phi_2)\\
\tilde{V_{c_3b}} &= \frac{1}{\sqrt{2}}\sqrt{\frac{1}{5}}\Omega_1^*\cos(\omega_1 t+\phi_1) - \frac{1}{\sqrt{2}}\sqrt{\frac{1}{5}}\Omega_2^*\cos(\omega_2 t+\phi_2)\\
\tilde{V_{bc_4}} &= \frac{1}{\sqrt{2}}\sqrt{\frac{1}{120}}\Omega_1\cos(\omega_1 t+\phi_1) + \frac{1}{\sqrt{2}}\sqrt{\frac{1}{120}}\Omega_2\cos(\omega_2 t+\phi_2)\\
\tilde{V_{c_4b}} &= \frac{1}{\sqrt{2}}\sqrt{\frac{1}{120}}\Omega_1^*\cos(\omega_1 t+\phi_1) + \frac{1}{\sqrt{2}}\sqrt{\frac{1}{120}}\Omega_2^*\cos(\omega_2 t+\phi_2)\\
\tilde{V_{bc_5}} &= -\frac{1}{\sqrt{2}}\sqrt{\frac{1}{8}}\Omega_1\cos(\omega_1 t+\phi_1) - \frac{1}{\sqrt{2}}\sqrt{\frac{1}{8}}\Omega_2\cos(\omega_2 t+\phi_2)\\
\tilde{V_{c_5b}} &= -\frac{1}{\sqrt{2}}\sqrt{\frac{1}{8}}\Omega_1^*\cos(\omega_1 t+\phi_1) - \frac{1}{\sqrt{2}}\sqrt{\frac{1}{8}}\Omega_2^*\cos(\omega_2 t+\phi_2)\\
\tilde{V_{bc_6}} &= \frac{1}{\sqrt{2}}\sqrt{\frac{1}{5}}\Omega_1\cos(\omega_1 t+\phi_1) + \frac{1}{\sqrt{2}}\sqrt{\frac{1}{5}}\Omega_2\cos(\omega_2 t+\phi_2)\\
\tilde{V_{c_6b}} &= \frac{1}{\sqrt{2}}\sqrt{\frac{1}{5}}\Omega_1^*\cos(\omega_1 t+\phi_1) + \frac{1}{\sqrt{2}}\sqrt{\frac{1}{5}}\Omega_2^*\cos(\omega_2 t+\phi_2).
\end{aligned}
\tag{A.4}
$$

These matrix elements give $\frac{1}{6}\frac{\Omega_1\Omega_2}{2\Delta}$ Rabi frequency, assuming the energy differences between excited state hyperfine splittings are negligible compared to the single photon detuning Δ.

A.1.3 Linear-linear polarization

For linear-linear polarization, i.e. $\vec{\epsilon_1} \parallel \vec{\epsilon_2}$, we write $\vec{\epsilon_1} = \frac{1}{\sqrt{2}}(\frac{\hat{e_x}-i\hat{e_y}}{\sqrt{2}} - \frac{\hat{e_x}+i\hat{e_y}}{\sqrt{2}})$ and $\vec{\epsilon_2} = \frac{1}{\sqrt{2}}(\frac{\hat{e_x}-i\hat{e_y}}{\sqrt{2}} - \frac{\hat{e_x}+i\hat{e_y}}{\sqrt{2}})$. Thus the matrix elements become:

$$
\begin{aligned}
\tilde{V_{ac_k}} &= (C^{a,c_k}_{\sigma_-} + C^{a,c_k}_{\sigma_+})\frac{\langle J||er||J'\rangle E_1}{\sqrt{2}\hbar}\cos(\omega_1 t + \phi_1) + (C^{a,c_k}_{\sigma_-} + C^{a,c_k}_{\sigma_+})\frac{\langle J||er||J'\rangle E_2}{\sqrt{2}\hbar}\cos(\omega_2 t + \phi_2)\\
\tilde{V_{c_k a}} &= (C^{c_k,a}_{\sigma_-} + C^{c_k,a}_{\sigma_+})\frac{\langle J'||er||J\rangle E_1}{\sqrt{2}\hbar}\cos(\omega_1 t + \phi_1) + (C^{c_k,a}_{\sigma_-} + C^{c_k,a}_{\sigma_+})\frac{\langle J'||er||J\rangle E_2}{\sqrt{2}\hbar}\cos(\omega_2 t + \phi_2)\\
\tilde{V_{bc_k}} &= (C^{b,c_k}_{\sigma_-} + C^{b,c_k}_{\sigma_+})\frac{\langle J||er||J'\rangle E_1}{\sqrt{2}\hbar}\cos(\omega_1 t + \phi_1) + (C^{b,c_k}_{\sigma_-} + C^{b,c_k}_{\sigma_+})\frac{\langle J||er||J'\rangle E_2}{\sqrt{2}\hbar}\cos(\omega_2 t + \phi_2)\\
\tilde{V_{c_k b}} &= (C^{c_k,b}_{\sigma_-} + C^{c_k,b}_{\sigma_+})\frac{\langle J'||er||J\rangle E_1}{\sqrt{2}\hbar}\cos(\omega_1 t + \phi_1) + (C^{c_k,b}_{\sigma_-} + C^{c_k,b}_{\sigma_+})\frac{\langle J'||er||J\rangle E_2}{\sqrt{2}\hbar}\cos(\omega_2 t + \phi_2).
\end{aligned}
\tag{A.5}
$$

These result in:

$$\begin{aligned}
\tilde{V}_{ac_1} &= \frac{1}{\sqrt{2}}\sqrt{\frac{5}{24}}[\Omega_1 \cos(\omega_1 t + \phi_1) + \Omega_2 \cos(\omega_2 t + \phi_2)] \\
\tilde{V}_{c_1 a} &= \frac{1}{\sqrt{2}}\sqrt{\frac{5}{24}}[\Omega_1^* \cos(\omega_1 t + \phi_1) + \Omega_2^* \cos(\omega_2 t + \phi_2)] \\
\tilde{V}_{ac_2} &= \frac{1}{\sqrt{2}}\sqrt{\frac{1}{8}}[\Omega_1 \cos(\omega_1 t + \phi_1) + \Omega_2 \cos(\omega_2 t + \phi_2)] \\
\tilde{V}_{c_2 a} &= \frac{1}{\sqrt{2}}\sqrt{\frac{1}{8}}[\Omega_1^* \cos(\omega_1 t + \phi_1) + \Omega_2^* \cos(\omega_2 t + \phi_2)] \\
\tilde{V}_{ac_3} &= \tilde{V}_{c_3 a} = 0 \\
\tilde{V}_{ac_4} &= -\frac{1}{\sqrt{2}}\sqrt{\frac{5}{24}}[\Omega_1 \cos(\omega_1 t + \phi_1) + \Omega_2 \cos(\omega_2 t + \phi_2)] \\
\tilde{V}_{c_4 a} &= -\frac{1}{\sqrt{2}}\sqrt{\frac{5}{24}}[\Omega_1^* \cos(\omega_1 t + \phi_1) + \Omega_2^* \cos(\omega_2 t + \phi_2)] \\
\tilde{V}_{ac_5} &= \frac{1}{\sqrt{2}}\sqrt{\frac{1}{8}}[\Omega_1 \cos(\omega_1 t + \phi_1) + \Omega_2 \cos(\omega_2 t + \phi_2)] \\
\tilde{V}_{c_5 a} &= \frac{1}{\sqrt{2}}\sqrt{\frac{1}{8}}[\Omega_1^* \cos(\omega_1 t + \phi_1) + \Omega_2^* \cos(\omega_2 t + \phi_2)] \\
\tilde{V}_{ac_6} &= \tilde{V}_{c_6 a} = 0 \\
\tilde{V}_{bc_1} &= \frac{1}{\sqrt{2}}\sqrt{\frac{1}{120}}[\Omega_1 \cos(\omega_1 t + \phi_1) + \Omega_2 \cos(\omega_2 t + \phi_2)] \\
\tilde{V}_{c_1 b} &= \frac{1}{\sqrt{2}}\sqrt{\frac{1}{120}}[\Omega_1^* \cos(\omega_1 t + \phi_1) + \Omega_2^* \cos(\omega_2 t + \phi_2)] \\
\tilde{V}_{bc_2} &= \frac{1}{\sqrt{2}}\sqrt{\frac{1}{8}}[\Omega_1 \cos(\omega_1 t + \phi_1) + \Omega_2 \cos(\omega_2 t + \phi_2)] \\
\tilde{V}_{c_2 b} &= \frac{1}{\sqrt{2}}\sqrt{\frac{1}{8}}[\Omega_1^* \cos(\omega_1 t + \phi_1) + \Omega_2^* \cos(\omega_2 t + \phi_2)] \\
\tilde{V}_{bc_3} &= \frac{1}{\sqrt{2}}\sqrt{\frac{1}{5}}[\Omega_1 \cos(\omega_1 t + \phi_1) + \Omega_2 \cos(\omega_2 t + \phi_2)] \\
\tilde{V}_{c_3 b} &= \frac{1}{\sqrt{2}}\sqrt{\frac{1}{5}}[\Omega_1^* \cos(\omega_1 t + \phi_1) + \Omega_2^* cos(\omega_2 t + \phi_2)] \\
\tilde{V}_{bc_4} &= \frac{1}{\sqrt{2}}\sqrt{\frac{1}{120}}[\Omega_1 \cos(\omega_1 t + \phi_1) + \Omega_2 \cos(\omega_2 t + \phi_2)] \\
\tilde{V}_{c_4 b} &= \frac{1}{\sqrt{2}}\sqrt{\frac{1}{120}}[\Omega_1^* \cos(\omega_1 t + \phi_1) + \Omega_2^* \cos(\omega_2 t + \phi_2)] \\
\tilde{V}_{bc_5} &= -\frac{1}{\sqrt{2}}\sqrt{\frac{1}{8}}[\Omega_1 \cos(\omega_1 t + \phi_1) + \Omega_2 \cos(\omega_2 t + \phi_2)] \\
\tilde{V}_{c_5 b} &= -\frac{1}{\sqrt{2}}\sqrt{\frac{1}{8}}[\Omega_1^* \cos(\omega_1 t + \phi_1) + \Omega_2^* \cos(\omega_2 t + \phi_2)] \\
\tilde{V}_{bc_6} &= \frac{1}{\sqrt{2}}\sqrt{\frac{1}{5}}[\Omega_1 \cos(\omega_1 t + \phi_1) + \Omega_2 \cos(\omega_2 t + \phi_2)] \\
\tilde{V}_{c_6 b} &= \frac{1}{\sqrt{2}}\sqrt{\frac{1}{5}}[\Omega_1^* \cos(\omega_1 t + \phi_1) + \Omega_2^* \cos(\omega_2 t + \phi_2)].
\end{aligned} \tag{A.6}$$

These matrix elements give 0 Rabi frequency.

A.2 Raman transition with multiple frequency components

A.2.1 Double beam modulation scheme

If both beams are phase modulated in the same way, the frequency components become:

$$\begin{aligned} E_{1,n} &= E_{10} J_n(\beta) e^{i(\omega_{10}+n\omega_{EOM})t+i(n\phi+\phi_{10,n})} + c.c \\ E_{2,n} &= E_{20} J_n(\beta) e^{i(\omega_{20}+n\omega_{EOM})t+i(n\phi+\phi_{20,n})} + c.c \end{aligned} \tag{A.7}$$

where $\phi_{10,n} = k_{10,n}x = \omega_{n,1}x/c$ and $\phi_{20,n} = k_{20,n}x = \omega_{n,2}x/c$. Using results from section 2.5, we get the Rabi frequency of the system to be:

$$\Omega = \frac{1}{2}|\sum_k \sum_n \frac{e^{-i(\phi_{n,1}-\phi_{n+1,2})}\Omega^{c_k a}_{n+1,2}\Omega^{c_k b}_{n,1}}{\omega_{c_k b} - \omega_{n,1}}| \tag{A.8}$$

where $\phi_{n,1} - \phi_{n+1,2} = \phi_{10,n} - \phi_{20,n+1} - \phi$ and ϕ is the modulation phase. If the two beams are counter-propagating, then $\phi_{10,n} - \phi_{20,n+1} = (\frac{\omega_{10}+\omega_{20}}{c} + (2n+1)\frac{\omega_{EOM}}{c})x$. Thus, the Rabi frequency is position dependent:

$$\Omega = \Omega(x) = \frac{1}{2}|\sum_k \sum_n \frac{\Omega^{c_k a}_{n+1,2}\Omega^{c_k b}_{n,1}}{\omega_{c_k b} - \omega_{n,1}} e^{-i(2n+1)\frac{\omega_{EOM}}{c}x}|. \tag{A.9}$$

Since $\Omega(x) = \Omega(x + \lambda/2)$, $\lambda = 2\pi c/\omega_{EOM}$. The magnitude of the Rabi frequency has a period of $\lambda/2$.

Appendix B

Cancel the Polarization effects from the Vacuum Chamber Wall

The vacuum chamber wall is modeled as an arbitrary wave plate. This means that the wall has a fast and a slow axis that is perpendicular to each other. When a linearly polarized light travels through the wall, the electric field that is parallel to the slow axis will acquire an arbitrary phase ϕ with respect to the electric field that is parallel to the fast axis. I will demonstrate that to cancel this effect, we need a half waveplate and a quarter waveplate.

First, I will show that the combination of a half and a quarter waveplate can generate any elliptically polarized light from a linearly polarized light. For example, to generate the elliptically polarized light shown in Figure B.1 (this is an arbitrary one), we first use a half waveplate to rotate a linearly polarized light such that it is parallel to the light blue arrow. Then we align the fast and slow axis of the quarter waveplate to axis 1 and 2 in Figure B.1. This generates the elliptical polarization shown by the red ellipse in Figure B.1.

We next see that to get a linearly or circularly polarized light after the effect of the chamber wall, we need elliptically polarized light as an input. In Figure B.2, the x and y axis are the fast and slow axis of the vacuum chamber wall. The electric field we expect after the wall is linearly polarized with angle θ from the x axis. This writes as

$$\begin{cases} E_x = E\cos\theta \cdot \cos(\omega t) \\ E_y = E\sin\theta \cdot \cos(\omega t). \end{cases} \tag{B.1}$$

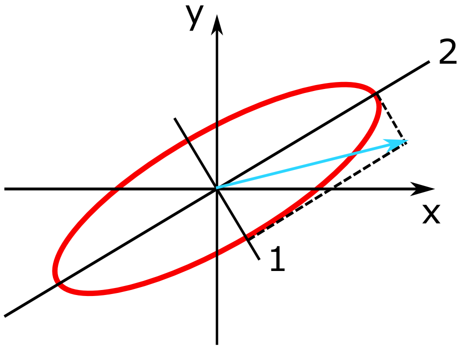

Figure B.1: The red ellipse shows an arbitrary elliptical polarization. 1 and 2 are the minor and major axis of the ellipse. Light blue arrow shows a linear polarization.

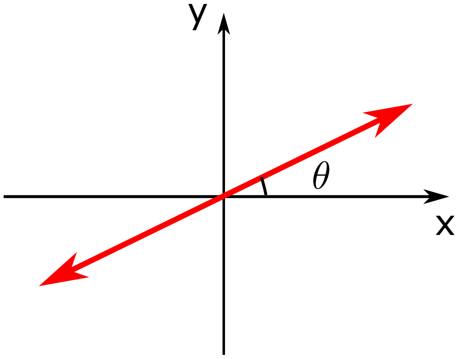

Figure B.2: Optical axis of the vacuum chamber wall. The x and y axis correspond to the fast and slow axis of the vacuum chamber wall. The red arrow is the linear polarized light after passing through the chamber wall. The angle between the electric field of the light and the x axis is θ.

Thus, before passing through the vacuum chamber wall, the electric field writes

$$\begin{cases} E_x = E\cos\theta\cdot\cos(\omega t+\phi) \\ E_y = E\sin\theta\cdot\cos(\omega t). \end{cases} \tag{B.2}$$

This stands for elliptically polarized light where the ellipse equation is

$$x^2 - 2\frac{\cos\phi\cdot\cos\theta}{\sin\theta}xy + \frac{\cos^2\theta}{\sin^2\theta}y^2 = E^2\cos^2\theta\sin^2\phi.$$

Using the same method, the electric field of circularly polarized light after the wall writes

$$\begin{cases} E_x = \frac{1}{\sqrt{2}}E\cdot\cos(\omega t+\frac{\pi}{2}) \\ E_y = \frac{1}{\sqrt{2}}E\cdot\cos(\omega t). \end{cases} \tag{B.3}$$

Thus, before the vacuum chamber, the electric field writes

$$\begin{cases} E_x = \frac{1}{\sqrt{2}} E \cdot \cos(\omega t + \frac{\pi}{2} + \phi) \\ E_y = \frac{1}{\sqrt{2}} E \cdot \cos(\omega t). \end{cases} \tag{B.4}$$

This stands for elliptically polarized light where the ellipse equation is

$$x^2 + 2\sin\phi \cdot xy + y^2 = \frac{E^2}{2}\cos^2\phi.$$

Appendix C

Two-level system driven by multiple frequency components

The quantum state of a 2-level system is $|\psi(t)\rangle = \psi_a(t)e^{-i\omega_a t}|a\rangle + \psi_b(t)e^{-i\omega_b t}|b\rangle$. The Schrodinger equation is

$$i\hbar \begin{pmatrix} \dot{\psi}_a \\ \dot{\psi}_b \end{pmatrix} = \begin{pmatrix} 0 & V_{ab}e^{-i\omega_0 t} \\ V_{ba}e^{i\omega_0 t} & 0 \end{pmatrix} \begin{pmatrix} \psi_a \\ \psi_b \end{pmatrix} \tag{C.1}$$

where $\omega_0 = \omega_b - \omega_a$. We apply a transformation as the following:

$$\begin{aligned} |\psi_a|^2 &= \frac{1+w}{2} \\ \psi_a \psi_b^* e^{i\omega_0 t} &= \frac{u - iv}{2} \\ |\psi_b|^2 &= \frac{1-w}{2} \end{aligned} \tag{C.2}$$

where $u, v, w \in \mathcal{R}$. Thus, Equation C.1 becomes:

$$\begin{aligned} \dot{u} &= \omega_0 v - \frac{2V_{abi}}{\hbar} w \\ \dot{v} &= -\omega_0 u - \frac{2V_{abr}}{\hbar} w \\ \dot{w} &= \frac{2V_{abi}}{\hbar} u + \frac{2V_{abr}}{\hbar} v \end{aligned} \tag{C.3}$$

i.e.

$$\frac{d\vec{a}}{dt} = \vec{\Omega} \times \vec{a} \tag{C.4}$$

where $\vec{a} = (u, v, w)$ and $\vec{\Omega} = (2V_{abr}/\hbar, -2V_{abi}/\hbar, -\omega_0)$. $V_{abr} = \Re[V_{ab}]$, $V_{abi} = \Im[V_{ab}]$, $V_{ab} = \langle a|V|b\rangle$, $V_{ba} = \langle b|V|a\rangle$, and $V_{ba} = V_{ab}^*$. Based on this result, the evolution of a 2-level system is equivalent to a vector rotation about an axis.

For a multi-mode electric field, $\vec{E} = \sum_k E_k \vec{\epsilon_k} cos(\omega_k t + \phi_k)$. Thus,

$$V_{ab} = \sum_k \langle a|\vec{p} \cdot \vec{\epsilon_k}|b\rangle E_k cos(\omega_k t + \phi_k) = \sum_k \hbar \Omega_k cos(\omega_k t + \phi_k)$$

where ϕ_k is the phase of the electric field at the interaction location, and $\Omega_k = \frac{\langle a|\vec{p} \cdot \vec{\epsilon_k}|b\rangle E_k}{\hbar}$. To simplify the notation and without loss of generality, we assume $V_{ab} \in \mathcal{R}$. In this case

$$\vec{\Omega} = (\sum_k 2\Omega_k cos(\omega_k t + \phi_k), 0, -\omega_0) = \sum_k \vec{\Omega_k} + \vec{\Omega_0}$$

where $\vec{\Omega_k} = (2\Omega_k cos(\omega_k t + \phi_k), 0, 0)$ and $\vec{\Omega_0} = (0, 0, -\omega_0)$. Each $\vec{\Omega_k}$ can be decomposed as the sum of $\vec{\Omega_k}^+$ and $\vec{\Omega_k}^-$. Here $\vec{\Omega_k}^+ = (\Omega_k cos(\omega_k t + \phi_k), \Omega_k sin(\omega_k t + \phi_k), 0)$ is a vector rotating counter clockwise in the xy plane with angular velocity ω_k; and $\vec{\Omega_k}^- = (\Omega_k cos(\omega_k t + \phi_k), -\Omega_k sin(\omega_k t + \phi_k), 0)$ is a vector rotating clockwise in the xy plane with the same angular velocity ω_k. The state evolution is equivalent to the rotation of the vector $\vec{a}$ around $\vec{\Omega}$. Here, $\vec{\Omega}$ itself varies and is decomposed into $2n + 1$ components.

Now we apply the rotating-wave approximation. If we go to the rotation frame of one of the $\vec{\Omega_k}^-$, say $\vec{\Omega_i}^-$, then all the $\vec{\Omega_k}^+$ terms rotating at angular velocity $\omega_k + \omega_i$ are much faster than the time scale we are interested in. Thus, we ignore these terms and only the $\vec{\Omega_k}^-$ and $\vec{\Omega_0}$ terms contribute to the equation of motion under rotating-wave approximation. The equation of motion becomes

$$\frac{d\vec{a}}{dt} = (\sum_k \vec{\Omega_k}^- + \vec{\Omega_0}) \times \vec{a}. \tag{C.5}$$

Now we determine what an observer in the rotating frame will see. A vector standing still in the original frame will now rotate counter clockwise at ω_i, i.e.

$$\vec{a}_{\text{new}} = \begin{pmatrix} cos(\omega_i t) & -sin(\omega_i t) & 0 \\ sin(\omega_i t) & cos(\omega_i t) & 0 \\ 0 & 0 & 1 \end{pmatrix} \vec{a}. \tag{C.6}$$

Thus, the new equation of motion in the rotating frame of $\vec{\Omega_i}^-$ becomes:

$$\begin{aligned}
\dot{u}_{\text{new}} &= (\omega_0 - \omega_i) \cdot v_{\text{new}} - \Omega_i sin\phi_i \cdot w_{\text{new}} + \sum_{i \neq k} \Omega_k sin[(\omega_i - \omega_k)t - \phi_k] \cdot w_{\text{new}} \\
\dot{v}_{\text{new}} &= -(\omega_0 - \omega_i) \cdot u_{\text{new}} - \Omega_i cos\phi_i \cdot w_{\text{new}} - \sum_{i \neq k} \Omega_k cos[(\omega_k - \omega_i)t + \phi_k] \cdot w_{\text{new}} \\
\dot{w}_{\text{new}} &= \Omega_i sin\phi_i \cdot u_{\text{new}} + \Omega_i cos\phi_i \cdot v_{\text{new}} + \sum_{i \neq k} \Omega_k cos[(\omega_k - \omega_i)t + \phi_k] \cdot v_{\text{new}} \\
&\quad - \sum_{i \neq k} \Omega_k sin[(\omega_i - \omega_k)t - \phi_k] \cdot u_{\text{new}}
\end{aligned} \tag{C.7}$$

i.e.

$$\frac{d\vec{a}_{\text{new}}}{dt} = \vec{\Omega}_{\text{new}} \times \vec{a}_{\text{new}} + \vec{\Omega}_{\text{extra}} \times \vec{a}_{\text{new}} \tag{C.8}$$

where

$$\vec{\Omega}_{\text{new}} = (\Omega_i cos\phi_i, -\Omega_i sin\phi_i, -(\omega_0 - \omega_i))$$

and

$$\vec{\Omega}_{\text{extra}} = (\sum_{i \neq k} \Omega_k cos[(\omega_k - \omega_i)t + \phi_k], -\sum_{i \neq k} \Omega_k sin[(\omega_k - \omega_i)t + \phi_k], 0).$$

In cases where $\omega_k - \omega_i \gg \Omega_i$, $\omega_0 - \omega_i$, the rotations around $\vec{\Omega}_{\text{new}}$ and $\vec{\Omega}_{\text{extra}}$ can be viewed as independent. For a vector $\vec{b}$ experience a torque of $\vec{\Omega}_{\text{extra}}$, we have:

$$\frac{d\vec{b}}{dt} = \vec{\Omega}_{\text{extra}} \times \vec{b} \tag{C.9}$$

where $\vec{\Omega}_{\text{extra}}$ is fast rotating on the xy plane. We move to another rotating frame that rotates clockwise at angular velocity $\omega_j - \omega_i$. We determine what an observer in this frame will see

$$\vec{b}_{\text{new}} = \begin{pmatrix} cos(\omega_j - \omega_i)t & -sin(\omega_j - \omega_i)t & 0 \\ sin(\omega_j - \omega_i)t & cos(\omega_j - \omega_i)t & 0 \\ 0 & 0 & 1 \end{pmatrix} \vec{b}. \tag{C.10}$$

Follow similar steps as previously, we find

$$\frac{d\vec{b}_{\text{new}}}{dt} = \vec{\Omega}_{\text{new}} \times \vec{b}_{\text{new}} + \vec{\Omega}_{\text{extra}} \times \vec{b}_{\text{new}} \tag{C.11}$$

where

$$\vec{\Omega}_{\text{new}} = (\Omega_j cos\phi_j, -\Omega_j sin\phi_j, \omega_j - \omega_i)$$

and

$$\vec{\Omega}_{\text{extra}} = (\sum_{i\neq k, j\neq k} \Omega_k cos[(\omega_k - \omega_j)t + \phi_k], -\sum_{i\neq k, j\neq k} \Omega_k sin[(\omega_k - \omega_j)t + \phi_k], 0).$$

In cases where $\omega_k - \omega_j \gg \Omega_j, \omega_j - \omega_i$, we can keep separating the $\vec{\Omega}_{\text{new}}$ and $\vec{\Omega}_{\text{extra}}$ motions.

Thus, the evolution of $\vec{a}$ under multiple frequency components can be viewed as a rotation of $\vec{a}$ around $(\Omega_i cos\phi_i, -\Omega_i sin\phi_i, -(\omega_0 - \omega_i))$ plus some corrections due to frequency components other than ω_i (Equation C.8). Here ω_i is chosen to minimize $\omega_0 - \omega_i$. The corrections can be again viewed as a rotation of $\vec{a}$ around $(\Omega_j cos\phi_j, -\Omega_j sin\phi_j, \omega_j - \omega_i)$ plus some corrections due to frequency components other than ω_i and ω_j where ω_j is chosen to minimize $\omega_j - \omega_i$ (Equation C.11). We can keep separating the correction into a constant term and a fast changing term as the next level of correction when considering more and more frequency components, as long as the time scale of the two terms differ by a lot.

Bibliography

[1] M. S. Safronova, D. Budker, D. DeMille, Derek F. Jackson Kimball, A. Derevianko, and Charles W. Clark. Search for new physics with atoms and molecules. *Rev. Mod. Phys.*, 90:025008, Jun 2018.

[2] A. Derevianko and M. Pospelov. Hunting for topological dark matter with atomic clocks. *Nature Physics*, 10(12):933–936, December 2014.

[3] N. Hinkley, J. A. Sherman, N. B. Phillips, M. Schioppo, N. D. Lemke, K. Beloy, M. Pizzocaro, C. W. Oates, and A. D. Ludlow. An atomic clock with 10^{-18} instability. *Science*, 341(6151):1215–1218, 2013.

[4] W. F. McGrew, X. Zhang, R. J. Fasano, S. A. Schäffer, K. Beloy, D. Nicolodi, R. C. Brown, N. Hinkley, G. Milani, M. Schioppo, T. H. Yoon, and A. D. Ludlow. Atomic clock performance enabling geodesy below the centimetre level. *Nature*, 564(7734):87, 2018.

[5] B. J. Bloom, T. L. Nicholson, J. R. Williams, S. L. Campbell, M. Bishof, X. Zhang, W. Zhang, S. L. Bromley, and J. Ye. An optical lattice clock with accuracy and stability at the $10^{\text{-}18}$ level. *Nature*, 506(7486):71–75, February 2014.

[6] S. L. Campbell, R. B. Hutson, G. E. Marti, A. Goban, N. Darkwah Oppong, R. L. McNally, L. Sonderhouse, J. M. Robinson, W. Zhang, B. J. Bloom, and J. Ye. A Fermi-degenerate three-dimensional optical lattice clock. *Science*, 358(6359):90–94, October 2017.

[7] Peter Asenbaum, Chris Overstreet, Minjeong Kim, Joseph Curti, and Mark A. Kasevich. Atom-interferometric test of the equivalence principle at the 10^{-12} level. *Phys. Rev. Lett.*, 125:191101, Nov 2020.

[8] Andrea Bertoldi, Kai Bongs, Philippe Bouyer, et al. AEDGE: Atomic experiment for dark matter and gravity exploration in space. *Experimental Astronomy*, 2021.

[9] Mahiro Abe, Philip Adamson, Marcel Borcean, et al. Matter-wave atomic gradiometer interferometric sensor (magis-100). *Quantum Science and Technology*, 2021.

[10] Yousef Abou El-Neaj, Cristiano Alpigiani, Sana Amairi-Pyka, et al. AEDGE: Atomic experiment for dark matter and gravity exploration in space. *EPJ Quantum Technology*, 7(1):6, 2020.

[11] Xuejian Wu, Zachary Pagel, Bola S. Malek, Timothy H. Nguyen, Fei Zi, Daniel S. Scheirer, and Holger Müller. Gravity surveys using a mobile atom interferometer. *Science Advances*, 5(9), 2019.

[12] Kai Bongs, Michael Holynski, Jamie Vovrosh, Philippe Bouyer, Gabriel Condon, Ernst Rasel, Christian Schubert, Wolfgang P. Schleich, and Albert Roura. Taking atom interferometric quantum sensors from the laboratory to real-world applications. *Nature Reviews Physics*, 1(12):731–739, December 2019.

[13] T. L. Gustavson, P. Bouyer, and M. A. Kasevich. Precision rotation measurements with an atom interferometer gyroscope. *Phys. Rev. Lett.*, 78:2046–2049, Mar 1997.

[14] Hayden J. McGuinness, Akash V. Rakholia, and Grant W. Biedermann. High data-rate atom interferometer for measuring acceleration. *Applied Physics Letters*, 100(1):011106, 2012.

[15] B. Canuel, F. Leduc, D. Holleville, A. Gauguet, J. Fils, A. Virdis, A. Clairon, N. Dimarcq, Ch. J. Bordé, A. Landragin, and P. Bouyer. Six-axis inertial sensor using cold-atom interferometry. *Phys. Rev. Lett.*, 97:010402, Jul 2006.

[16] Florence Yver-Leduc, Patrick Cheinet, Jérôme Fils, André Clairon, Noël Dimarcq, David Holleville, Philippe Bouyer, and Arnaud Landragin. Reaching the quantum noise limit in a high-sensitivity cold-atom inertial sensor. *Journal of Optics B: Quantum and Semiclassical Optics*, 5(2):S136–S142, April 2003.

[17] G. Santarelli, Ph. Laurent, P. Lemonde, A. Clairon, A. G. Mann, S. Chang, A. N. Luiten, and C. Salomon. Quantum projection noise in an atomic fountain: A high stability cesium frequency standard. *Phys. Rev. Lett.*, 82:4619–4622, Jun 1999.

[18] W. Wasilewski, K. Jensen, H. Krauter, J. J. Renema, M. V. Balabas, and E. S. Polzik. Quantum noise limited and entanglement-assisted magnetometry. *Phys. Rev. Lett.*, 104:133601, Mar 2010.

[19] O. Arcizet, P.-F. Cohadon, T. Briant, M. Pinard, A. Heidmann, J.-M. Mackowski, C. Michel, L. Pinard, O. Français, and L. Rousseau. High-sensitivity optical monitoring of a micromechanical resonator with a quantum-limited optomechanical sensor. *Phys. Rev. Lett.*, 97:133601, Sep 2006.

[20] G. Rosi, F. Sorrentino, L. Cacciapuoti, M. Prevedelli, and G. M. Tino. Precision measurement of the Newtonian gravitational constant using cold atoms. *Nature*, 510(7506):518–521, June 2014.

[21] F. Sorrentino, Q. Bodart, L. Cacciapuoti, Y.-H. Lien, M. Prevedelli, G. Rosi, L. Salvi, and G. M. Tino. Sensitivity limits of a raman atom interferometer as a gravity gradiometer. *Phys. Rev. A*, 89:023607, Feb 2014.

[22] Vittorio Giovannetti, Seth Lloyd, and Lorenzo Maccone. Quantum metrology. *Phys. Rev. Lett.*, 96:010401, Jan 2006.

[23] Zilong Chen, Justin G. Bohnet, Joshua M. Weiner, Kevin C. Cox, and James K. Thompson. Cavity-aided nondemolition measurements for atom counting and spin squeezing. *Phys. Rev. A*, 89:043837, Apr 2014.

[24] Onur Hosten, Nils J. Engelsen, Rajiv Krishnakumar, and Mark A. Kasevich. Measurement noise 100 times lower than the quantum-projection limit using entangled atoms. *Nature*, 529(7587):505–508, 2016.

[25] J. Estève, C. Gross, A. Weller, S. Giovanazzi, and M. K. Oberthaler. Squeezing and entanglement in a Bose-Einstein condensate. *Nature*, 455(7217):1216–1219, October 2008.

[26] Max F. Riedel, Pascal Böhi, Yun Li, Theodor W. Hänsch, Alice Sinatra, and Philipp Treutlein. Atom-chip-based generation of entanglement for quantum metrology. *Nature*, 464(7292):1170–1173, April 2010.

[27] Monika H. Schleier-Smith, Ian D. Leroux, and Vladan Vuletić. States of an ensemble of two-level atoms with reduced quantum uncertainty. *Phys. Rev. Lett.*, 104:073604, Feb 2010.

[28] J. Appel, P. J. Windpassinger, D. Oblak, U. B. Hoff, N. Kjærgaard, and E. S. Polzik. Mesoscopic atomic entanglement for precision measurements beyond the standard quantum limit. *Proceedings of the National Academy of Sciences*, 106(27):10960–10965, 2009.

[29] Zilong Chen, Justin G. Bohnet, Shannon R. Sankar, Jiayan Dai, and James K. Thompson. Conditional spin squeezing of a large ensemble via the vacuum rabi splitting. *Phys. Rev. Lett.*, 106:133601, Mar 2011.

[30] Ian D. Leroux, Monika H. Schleier-Smith, and Vladan Vuletić. Implementation of cavity squeezing of a collective atomic spin. *Phys. Rev. Lett.*, 104:073602, Feb 2010.

[31] Kevin C. Cox, Graham P. Greve, Joshua M. Weiner, and James K. Thompson. Deterministic squeezed states with collective measurements and feedback. *Phys. Rev. Lett.*, 116:093602, Mar 2016.

[32] Ian D. Leroux, Monika H. Schleier-Smith, and Vladan Vuletić. Orientation-dependent entanglement lifetime in a squeezed atomic clock. *Phys. Rev. Lett.*, 104:250801, Jun 2010.

[33] Edwin Pedrozo-Peñafiel, Simone Colombo, Chi Shu, Albert F. Adiyatullin, Zeyang Li, Enrique Mendez, Boris Braverman, Akio Kawasaki, Daisuke Akamatsu, Yanhong Xiao, and Vladan Vuletić. Entanglement on an optical atomic-clock transition. *Nature*, 588(7838):414–418, December 2020.

[34] Masahiro Kitagawa and Masahito Ueda. Squeezed spin states. *Phys. Rev. A*, 47:5138–5143, Jun 1993.

[35] D. J. Wineland, J. J. Bollinger, W. M. Itano, F. L. Moore, and D. J. Heinzen. Spin squeezing and reduced quantum noise in spectroscopy. *Phys. Rev. A*, 46:R6797–R6800, Dec 1992.

[36] D. J. Wineland, J. J. Bollinger, W. M. Itano, and D. J. Heinzen. Squeezed atomic states and projection noise in spectroscopy. *Phys. Rev. A*, 50:67–88, Jul 1994.

[37] L Allen and J H Eberly. Optical resonance and two-level atoms. 1975.

[38] Marlan O. Scully and M. Suhail Zubairy. *Quantum Optics.* Cambridge University Press, 1997.

[39] Michel Devoret, Benjamin Huard, Robert Schoelkopf, and Leticia F. Cugliandolo. *Quantum Machines: Measurement and Control of Engineered Quantum Systems: Lecture Notes of the Les Houches Summer School: Volume 96.* Oxford University Press, July 2011.

[40] A. B. Klimov, L. L. Sánchez-Soto, A. Navarro, and E. C. Yustas. Effective hamiltonians in quantum optics: a systematic approach. *Journal of Modern Optics*, 49(13):2211–2226, 2002.

[41] I. Dotsenko. Raman spectroscopy of single atoms. 2002.

[42] A Kuzmich, N. P Bigelow, and L Mandel. Atomic quantum non-demolition measurements and squeezing. *Europhysics Letters (EPL)*, 42(5):481–486, Jun 1998.

[43] Monika Helene Schleier-Smith. Cavity-Enabled Spin Squeezing for a Quantum-Enhanced Atomic Clock. *Ph.D. thesis, MIT*, Jun 2011.

[44] Nils Johan Engelsen. Quantum Metrology Using Large Ensembles of Entangled Atoms. *Ph.D. thesis, Stanford University*, Dec 2016.

[45] Monika H. Schleier-Smith, Ian D. Leroux, and Vladan Vuletić. Squeezing the collective spin of a dilute atomic ensemble by cavity feedback. *Phys. Rev. A*, 81:021804, Feb 2010.

[46] R Wynands and S Weyers. Atomic fountain clocks. *Metrologia*, 42(3):S64–S79, jun 2005.

[47] Christopher J Foot. *Atomic physics.* Oxford University Press, 2005.

[48] Pippa Storey and Claude Cohen-Tannoudji. The Feynman path integral approach to atomic interferometry. a tutorial. *Journal de Physique II*, 4(11):1999–2027, Sep 1994.

[49] R. P. Feynman and A. R. Hibbs. *Quantum mechanics and path integrals.* New York : McGraw-Hill, 1965.

[50] P. R. Berman. *Atom interferometry.* San Diego: Academic Press, 2014.

[51] Jason Michael Hogan. Towards precision tests of general relativity using an atom interferometer. *Ph.D. thesis, Stanford University*, June 2010.

[52] Rajiv Krishnakumar. Entagling Atoms For Quantum Metrology. *Ph.D. thesis, Stanford University*, Sep 2017.

[53] Geert Vrijsen. Collective Quantum Behavior of Atomic Ensembles in High-finesse Optical Cavities. *Ph.D. thesis, Stanford University*, Dec 2011.

[54] Jongmin Lee. Collective Atom-cavity Interactions in a High-finesse Dual-wavelength Cavity. *Ph.D. thesis, Stanford University*, Aug 2011.

[55] Geert Vrijsen, Onur Hosten, Jongmin Lee, Simon Bernon, and Mark A. Kasevich. Raman lasing with a cold atom gain medium in a high-finesse optical cavity. *Phys. Rev. Lett.*, 107:063904, Aug 2011.

[56] Jongmin Lee, Geert Vrijsen, Igor Teper, Onur Hosten, and Mark A. Kasevich. Many-atom-cavity QED system with homogeneous atom-cavity coupling. *Opt. Lett.*, 39(13):4005–4008, Jul 2014.

[57] Eric D. Black. An introduction to Pound-Drever-Hall laser frequency stabilization. *American Journal of Physics*, 69(1):79–87, 2001.

[58] Kevin C. Cox, Graham P. Greve, Baochen Wu, and James K. Thompson. Spatially homogeneous entanglement for matter-wave interferometry created with time-averaged measurements. *Phys. Rev. A*, 94:061601, Dec 2016.

[59] Yunfan Wu, Rajiv Krishnakumar, Julián Martínez-Rincón, Benjamin K. Malia, Onur Hosten, and Mark A. Kasevich. Retrieval of cavity-generated atomic spin squeezing after free-space release. *Phys. Rev. A*, 102:012224, Jul 2020.

[60] Jiazhong Hu, Wenlan Chen, Zachary Vendeiro, Hao Zhang, and Vladan Vuletić. Entangled collective-spin states of atomic ensembles under nonuniform atom-light interaction. *Phys. Rev. A*, 92:063816, Dec 2015.

[61] J. J. Sakurai and Jim Napolitano. *Modern Quantum Mechanics.* Cambridge University Press, 2 edition, 2017.

[62] O. Hosten, R. Krishnakumar, N. J. Engelsen, and M. A. Kasevich. Quantum phase magnification. *Science*, 352(6293):1552–1555, 2016.

[63] Benjamin K. Malia, Yunfan Wu, Julián Martínez-Rincón, and Mark A. Kasevich. Utilizing machine learning to improve the precision of fluorescence imaging ofcavity-generated spin squeezed states. *Phys. Rev. A*, 102:012224, Jul 2021.

[64] Justin G. Bohnet, Brian C. Sawyer, Joseph W. Britton, Michael L. Wall, Ana Maria Rey, Michael Foss-Feig, and John J. Bollinger. Quantum spin dynamics and entanglement generation with hundreds of trapped ions. *Science*, 352(6291):1297–1301, 2016.

[65] D. B. Hume, I. Stroescu, M. Joos, W. Muessel, H. Strobel, and M. K. Oberthaler. Accurate atom counting in mesoscopic ensembles. *Phys. Rev. Lett.*, 111:253001, Dec 2013.

[66] C. D. Hamley, C. S. Gerving, T. M. Hoang, E. M. Bookjans, and M. S. Chapman. Spin-nematic squeezed vacuum in a quantum gas. *Nature Physics*, 8(4), April 2012.

[67] Benjamin K. Malia, Julián Martínez-Rincón, Yunfan Wu, Onur Hosten, and Mark A. Kasevich. Free space ramsey spectroscopy in rubidium with noise below the quantum projection limit. *Phys. Rev. Lett.*, 125:043202, Jul 2020.

[68] Benjamin Karl Malia. Integration of Spin Squeezed States into Free Space Atomic Sensors. *Ph.D. thesis, Stanford University*, Aug 2021.

[69] E Rocco, R N Palmer, T Valenzuela, V Boyer, A Freise, and K Bongs. Fluorescence detection at the atom shot noise limit for atom interferometry. *New Journal of Physics*, 16(9):093046, sep 2014.

[70] Boris Braverman, Akio Kawasaki, and Vladan Vuletić. Impact of non-unitary spin squeezing on atomic clock performance. *New Journal of Physics*, 20(10):103019, oct 2018.

[71] Ross T. Schermer, Frank Bucholtz, Carl A. Villarruel, Jesus Gil Gil, Tim D. Andreadis, and Keith J. Williams. Investigation of electro-optic modulator disruption by microwave-induced transients. *Opt. Express*, 17(25):22586–22602, Dec 2009.

[72] James P. Cahill, Weimin Zhou, and Curtis R. Menyuk. Additive phase noise of fiber-optic links used in photonic microwave-generation systems. *Appl. Opt.*, 56(3):B18–B25, Jan 2017.

[73] W. Shieh and L. Maleki. Phase noise of optical interference in photonic RF systems. *IEEE Photonics Technology Letters*, 10(11):1617–1619, 1998.

[74] D. Steck. Rubidium 87 D Line Data. 2003.